

SIZE DEPENDENT TUNING OF THE STRUCTURE AND MAGNETIC PROPERTIES OF RARE-EARTH TRANSITION METAL OXIDES AT NANOSCALE

A Thesis Submitted in partial fulfilment of the requirements of the degree of
Doctor of Philosophy in Physics

By

OIMANG BORANG

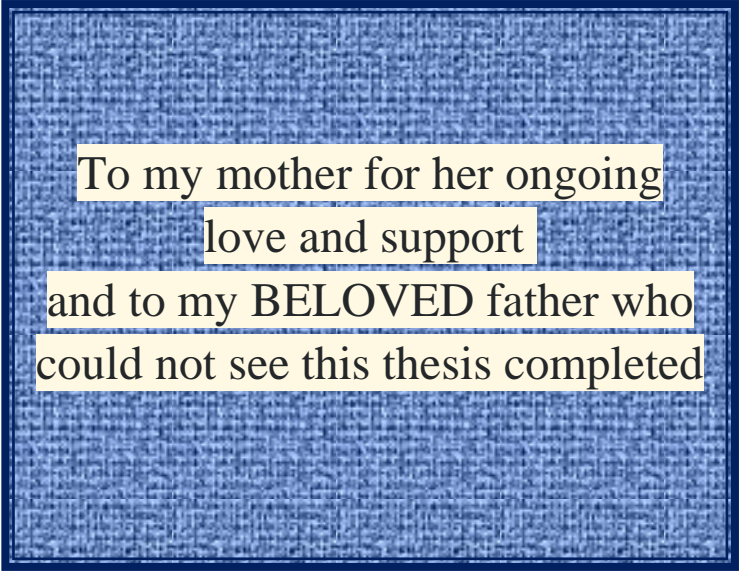
Ph.D. Registration no. 709/2016

Registration date 03.11.2015



**Department of Physics,
School of Sciences, Nagaland University,
Lumami – 798627, Nagaland, India.**

AUGUST, 2018



To my mother for her ongoing
love and support
and to my BELOVED father who
could not see this thesis completed



DEPARTMENT OF PHYSICS
NAGALAND UNIVERSITY
*(A Central University Estd. By the Act of Parliament
No. 35 of 1989)*
Headquarters: Lumami– 798627

DECLARATION

I, Ms. **Oimang Borang**, bearing registration No. 709/2016, hereby declare that the subject matter of the thesis entitled “*Size dependent tuning of the structure and magnetic properties of rare-earth transition metal oxides at nanoscale*” is the record of work done by me, that the contents of this thesis did not form basis of the award of any previous degree to me or to the best of my knowledge to anybody else, and that the thesis has not been submitted by me for any research degree in any other university/institute.

This is being submitted to the Nagaland University for the degree of Doctor of Philosophy in Physics.

Place:

(Oimang Borang)

Date:

Candidate

(Prof. M. Indira Devi)
*Head, Dept. of Physics and
Dean, School of Sciences*

(Dr. Y. Sundarayya)
Supervisor



DEPARTMENT OF PHYSICS
NAGALAND UNIVERSITY
(A Central University Estd. By the Act of Parliament
No. 35 of 1989)
Headquarters: Lumami - 798627

CERTIFICATE

This is to certify that the thesis entitled “*Size dependent tuning of the structure and magnetic properties of rare-earth transition metal oxides at nanoscale*” is a record of original research work carried out by Ms. Oimang Borang under my supervision. She is a registered research scholar, bearing the registration no. 709/ 2016 of the department of physics.

The candidate has fulfilled all the requirements of Ph.D. regulations of Nagaland University for submission of thesis. The work is original and neither the thesis nor any part of it has been submitted elsewhere for the award of any degree or distinctions. The thesis, therefore, forwarded for adjudication and consideration for the award of degree of Doctor of Philosophy in Physics under Nagaland University.

Date:
Place:

(Dr. Y. Sundarayya)
Supervisor

(Prof. M. Indira Devi)
Head, Dept. of Physics and
Dean, School of Sciences



DEPARTMENT OF PHYSICS
NAGALAND UNIVERSITY
*(A Central University Estd. By the Act of Parliament
No. 35 of 1989)*
Headquarters: Lumami - 798627

COURSE COMPLETION CERTIFICATE

This is to certify that Ms. **Oimang Borang** has satisfactorily completed the course offered in the Ph.D. Course Work Programme in Physics.

The Courses include:

PHY-801 Research Methodology

PHY-802 (B) Experimental Techniques (Theory) (Elective/ optional)

PHY-803 Review of literature Reports/ Seminar

(Prof. M. Indira Devi)
Head
Department of Physics
Nagaland University

ACKNOWLEDGEMENT

It's been a long journey for me, but at the end there are so many people to whom I want to extend my gratitude.

First of all, I am over whelming to share my heartiest gratitude to my respected supervisor, Dr. Y. Sundarayya for being my mentor. His incomparable lecture, vast knowledge, experience, wisdom and undying enthusiasm to explore new ideas have made my research interesting and successful. I thank him for guiding me with his constant encouragement and support. The times I have spent working with him are all worthwhile.

I am grateful to Dr. Shanta Singh Naorem, for willingly giving his precious time and his constructive suggestion and advices. He has been and always will be a great inspiration to me.

I am also deeply indebted to former Dean School of Sciences/ Head of Department, Lt. Prof. Sharif U. Ahmed for his encouragement and support during my research work.

I express my sincere gratitude to Present Dean School of Sciences/ Head of Department Prof. Indira Devi, for always pointing me in the right direction and for motivating me in my research work.

A special thanks to central Library of Nagaland University and all the staffs for making it possible to use UGC-provided software URKUND to check for plagiarism for the present thesis.

I also take this opportunity to thank Prof. S. N. Kaul, Prof. S. Srinath, Dr. Ravi and Dr. Pavan from magnetism group, University of Hyderabad (UoH).

I am grateful to my best friend Yaba and Sandip for helping me in everything, thank you for listening, offering me advice, and supporting me through this entire journey. Shivaraj and Ranjoy you were a living dictionary for me. Kenie, Marsosang, Lobe, Asang thank you so much for helping me out during thesis printing.

I extend my acknowledgement to School of Engineering and Technology (SEST), NIT chumukhedima, NERIST Nirjuli, for the X-ray diffractograms, School of Physics for FESEM images and EDAX spectra, Centre for Nanotechnology, for magnetic measurements, Central instruments laboratory (CIL) for low temperature EPR measurements, University of Hyderabad (UoH).

Also I want to thank UGC-NON NET fellowship and National Fellowship for Higher Education (NFHE) of ST students for the financial assistance.

I am grateful to my siblings and my dearest mother Unngan, who has supported me morally and emotionally throughout my life. They are the true source of all my joy, love and strength. I sincerely acknowledge their great sacrifices, support and love. I thank them humbly for making me the person I am today.

Above all I thank almighty God for his abundance love, grace and blessings.

Date:

Place:

(Oimang Borang)

CONTENTS

CHAPTER-1	INTRODUCTION	PAGE NO.
1.1	A Brief History of Multiferroics	1
1.2	Present Discussion on Multiferroics	2-6
1.3	Types of Multiferroics	7-9
1.4	Advantages, Disadvantages and Applications Of Multiferroic Materials	9-11
1.5	Rare earth and transition metals	11-18
1.6	Magnetic Structure of Rare Earth Orthochromites, RCrO_3	18-31
1.7	Rare earth chromates, RCrO_4	31-34
1.8	Aim and Scope of the Thesis	34-36
	References	37-43
 CHAPTER-2	 EXPERIMENTAL TECHNIQUES	
2.1	Introduction	44
2.2	Sol gel method	44-45
2.3	Hydrothermal synthesis	45-46
2.4	X-Ray Diffraction	46-51
2.4.1	Principle of X-Ray Powder Diffraction (XRD)	47-48
2.4.2	Working of X-Ray Diffractometer	48-51
2.5	FESEM and EDAX	51-54
2.6	Physical property measurement system (PPMS)	54-56

2.6.1	Theory of Operation	55-56
2.7	ESR Spectrometer	57-65
2.7.1	Principle of ESR	58-61
2.7.2	Working techniques and components of EPR spectrometer	61-64
2.7.3	Low Temperature EPR Measurements	64-65
	References	66-67
CHAPTER-3	SYNTHESIS AND CHARACTERIZATION	
3.1	Introduction	68
3.2	Synthesis procedure	69-70
3.3	Characterization	70-83
3.3.1	Crystal Structure	70-77
3.3.2	Morphological analysis of RCrO_4 and RCrO_3 nanoparticles	78-81
3.3.3	Elemental Analysis of RCrO_4 and RCrO_3 nanoparticles	81-83
3.4	Conclusion	83-84
	References	85-88
CHAPTER-4	MAGNETIC PROPERTIES OF RARE-EARTH CHROMATES NANOPARTICLES	
4.1	Introduction	89-90

4.2	Magnetic Properties of RCrO_4 nanoparticles	90-101
4.2.1	Magnetization (M) vs. Temperature (T) Measurements	90-95
4.2.2	Curie-Weiss Analysis	95-98
4.2.3	Magnetization (M) vs. Magnetic Field (H) Measurements	98-101
4.3	Conclusions	101-102
	References	103-104
CHAPTER-5	MAGNETIC PROPERTIES OF RARE-EARTH ORTHOCHROMITES NANOPARTICLES	
5.1	Introduction	105-106
5.2	Magnetic Properties of RCrO_3	106-118
5.2.1	Magnetization (M) vs. Temperature (T) Measurements	106-111
5.2.2	Curie -Weiss Analysis	111-114
5.2.3	Magnetization (M) vs. Magnetic Field (H) Measurements	115-118
5. 3	Conclusions	118-119
	References	120-122
CHAPTER-6	ELECTRON PARAMAGNETIC RESONANCE OF RCrO_3 (R = Eu, Gd and Er)	
6.1	Introduction	123-124

6.2	Critical View on Magnetic Properties of RCrO ₃ (R = Eu, Gd and Er)	124-128
6.3	Room-temperature EPR Spectra of RCrO ₃ (R = Eu, Gd and Er)	128-130
6.4	Temperature-dependent EPR Spectra of RCrO ₃ (R = Eu, Gd and Er)	130-141
6.5	Conclusions	141
	References	142-143
CHAPTER -7	CONCLUSIONS	144-146
	Papers Published	147
	Papers to be communicated	147
	Publications not related to this thesis	147
	Paper presentations	148
	Workshop/ winter school attended	149

LIST OF FIGURES

FIG.NO.	DESCRIPTION	PAGES
CHAPTER 1		
<i>Fig.1:</i>	Structure of ferromagnetic and ferroelectric	3
<i>Fig.2:</i>	Multiferroics combines the properties of ferroelectrics and ferromagnetic	5
<i>Fig.3:</i>	Different oxidation states of chromium	17
<i>Fig.4:</i>	Possible Spin structures of RCrO_3	20
<i>Fig.5:</i>	Orthorhombic structure of RCrO_3	22
<i>Fig.6:</i>	Polyhedral crystal structure, RCrO_3	24
<i>Fig.7:</i>	Rotation of magnetic vector during Spin-reorientation	27
<i>Fig.8:</i>	Polyhedral view of crystal structure of zircon type RCrO_4	32
CHAPTER 2		
<i>Fig.1:</i>	Schematic diagram of the mini-stainless steel auto clave and the Teflon liner	46
<i>Fig.2:</i>	Schematic Diagram of X-Ray Diffractometer	49
<i>Fig.3:</i>	Bruker D8 Advance diffractometer	50
<i>Fig.4:</i>	Physical property measurement system	55
<i>Fig.5:</i>	Bar magnet	59
<i>Fig.6:</i>	Bar magnet in a magnetic field	60
<i>Fig.7:</i>	Zeeman splitting	60
<i>Fig.8:</i>	Block diagram of ESR spectrometer	62
<i>Fig.9:</i>	Klystron tube	63

CHAPTER 3

<i>Fig.1:</i> Block diagram of the synthesis procedure for RCrO_4 and RCrO_3 nanoparticles	69
<i>Fig.2:</i> Rietveld profile matching of the X-ray diffractogram of SmCrO_4	72
<i>Fig.3:</i> Rietveld profile matching of the X-ray diffractogram of EuCrO_4	72
<i>Fig.4:</i> Rietveld profile matching of the X-ray diffractogram of GdCrO_4	73
<i>Fig.5:</i> Rietveld profile matching of the X-ray diffractogram of DyCrO_4	73
<i>Fig.6:</i> Rietveld profile matching of the X-ray diffractogram of ErCrO_4	74
<i>Fig.7:</i> Rietveld profile matching of the X-ray diffractogram of SmCrO_3	75
<i>Fig.8:</i> Rietveld profile matching of the X-ray diffractogram of EuCrO_3	75
<i>Fig.9:</i> Rietveld profile matching of the X-ray diffractogram of GdCrO_3	76
<i>Fig.10:</i> Rietveld profile matching of the X-ray diffractogram of DyCrO_3	76
<i>Fig.11:</i> Rietveld profile matching of the X-ray diffractogram of ErCrO_3	77
<i>Fig.12 (a):</i> Morphology of SmCrO_4 nanoparticles by FESEM	78
<i>Fig.12 (b):</i> Morphology of SmCrO_3 nanoparticles	78
<i>Fig.13 (a):</i> Morphology of EuCrO_4 nanoparticles	78
<i>Fig.13 (b):</i> Morphology of EuCrO_3 nanoparticles	78
<i>Fig.14 (a):</i> Morphology of GdCrO_4 nanoparticles	79
<i>Fig.14 (b):</i> Morphology of GdCrO_3 nanoparticles	79
<i>Fig.15 (a):</i> Morphology of DyCrO_4 nanoparticles	79
<i>Fig.15 (b):</i> Morphology of DyCrO_3 nanoparticles	79

<i>Fig.16 (a): Morphology of ErCrO₄nanoparticles</i>	80
<i>Fig.16 (b): Morphology of ErCrO₃nanoparticles</i>	80
<i>Fig.17 (a): The EDAX Spectrum of GdCrO₄ nanoparticles</i>	82
<i>Fig.17(b): The location of EDAX recorded on GdCrO₄ nanoparticles</i>	82
<i>Fig.18 (a): The EDAX Spectrum of ErCrO₃ nanoparticles</i>	82
<i>Fig.18(b): The location of EDAX recorded on ErCrO₃ nanoparticles</i>	82

CHAPTER 4

<i>Fig.1: Zero-Field Cooled (ZFC) and Field-Cooled (FC)</i>	91
Magnetization of SmCrO ₄	
<i>Fig.2: Zero-Field Cooled (ZFC) and Field-Cooled (FC)</i>	91
Magnetization of GdCrO ₄	
<i>Fig.3: Zero-Field Cooled (ZFC) and Field-Cooled (FC)</i>	93
Magnetization of DyCrO ₄	
<i>Fig.4: Zero-Field Cooled (ZFC) and Field-Cooled (FC)</i>	93
Magnetization of ErCrO ₄	
<i>Fig.5: Derivative of Zero-Field Cooled (ZFC) Magnetization of</i>	94
RCrO ₄ nanoparticles	
<i>Fig.6: Curie-Weiss fits of RCrO₄ nanoparticles</i>	97
<i>Fig.7: M-H curve of RCrO₄ recorded at 300 K (in PM regime) in the range</i>	99
H = -9 T to +9 T	
<i>Fig.8: M-H curve of SmCrO₄nanoparticles recorded at 5 K. The inset shows</i>	99

the curves in the Range $H = -9 \text{ T}$ to $+9 \text{ T}$	
<i>Fig.9:</i> M-H curve of GdCrO_4 nanoparticles recorded at 5 K . The inset shows	100
the curves in the Range $H = -9 \text{ T}$ to $+9 \text{ T}$	
<i>Fig.10:</i> M-H curve of DyCrO_4 nanoparticles recorded at 5 K . The inset shows	100
the curves in the Range $H = -9 \text{ T}$ to $+9 \text{ T}$	
<i>Fig.11:</i> M-H curve of ErCrO_4 nanoparticles recorded at 5 K . The inset shows	101
the curves in the Range $H = -9 \text{ T}$ to $+9 \text{ T}$	
 CHAPTER 5	
<i>Fig.1:</i> Zero-Field Cooled (ZFC) Field-Cooled (FC) Magnetization of	107
SmCrO_3 nanoparticles	
<i>Fig.2:</i> Zero-Field Cooled (ZFC) Field-Cooled (FC) Magnetization of	108
GdCrO_3 nanoparticles	
<i>Fig.3:</i> Zero-Field Cooled (ZFC) Field-Cooled (FC) Magnetization of	109
DyCrO_3 nanoparticles	
<i>Fig.4:</i> Zero-Field Cooled (ZFC) Field-Cooled (FC) Magnetization of	110
ErCrO_3 nanoparticles	
<i>Fig.5:</i> Derivative of Zero-Field Cooled (ZFC) Magnetization of RCrO_3	111
nanoparticles	
<i>Fig.6:</i> Modified Curie-Weiss fits of RCrO_3 nanoparticles	112
<i>Fig.7:</i> M-H curve of RCrO_3 recorded at 320 K (in PM regime) in the range	115
$H = -9 \text{ T}$ to $+9 \text{ T}$	

- Fig.8:* M-H curve of SmCrO₃ nanoparticles recorded at 5 K. The inset shows the 116
curves in the range H = -9 T to +9 T
- Fig.9:* M-H curve of GdCrO₃ nanoparticles recorded at 2.5 K. The inset shows 116
the curves in the range H = -9 T to +9 T
- Fig.10:* M-H curve of DyCrO₃ nanoparticles recorded at 2.5 K. The inset shows 117
the curves in the range H = -9 T to +9 T
- Fig.11:* M-H curve of ErCrO₃ nanoparticles recorded at 2.5 K. The inset shows 117
the curves in the range H = -9 T to +9 T

CHAPTER 6

- Fig.1:* Magnetization of ErCrO₃ with temperature. The inset shows the 125
bifurcation of ZFC and FC magnetization in the range 280 – 350 K
- Fig.2:* Reciprocal Susceptibility (χ^{-1}) of ErCrO₃ with temperature 126
- Fig.3:* Magnetization of EuCrO₃ with temperature 126
- Fig.4:* Reciprocal Susceptibility (χ^{-1}) of EuCrO₃ with temperature 127
- Fig.5:* Magnetization of GdCrO₃ with temperature 127
- Fig.6:* Reciprocal Susceptibility (χ^{-1}) of GdCrO₃ with temperature 128
- Fig.7:* EPR spectra of EuCrO₃, GdCrO₃, and ErCrO₃ nanoparticles at 373 K 129
- Fig.8:* As-recorded EPR spectra of EuCrO₃ nanoparticles as a function of 131
temperature
- Fig.9:* As-recorded EPR spectra of ErCrO₃ nanoparticles as a function 131
Of temperature

<i>Fig.10:</i> As-recorded EPR spectra of GdCrO ₃ nanoparticles as a function of temperature	132
<i>Fig.11:</i> The EPR spectral parameters peak-to-peak width (ΔH_{pp}) and Differential intensity (ΔI_{pp}) of EuCrO ₃ with temperature	134
<i>Fig. 12:</i> The magnetic parameters spontaneous magnetization ($4\pi M_s$) and Magnetic anisotropy field (H_k) of EuCrO ₃ as a function of temperature	135
<i>Fig. 13:</i> The EPR spectral parameters peak-to-peak width (ΔH_{pp}) and Differential intensity (ΔI_{pp}) of GdCrO ₃ with temperature	136
<i>Fig. 14:</i> The magnetic parameters spontaneous magnetization ($4\pi M_s$) and magnetic anisotropy field (H_k) of GdCrO ₃ as a function of temperature	137
<i>Fig. 15:</i> The EPR spectral parameters peak-to-peak width (ΔH_{pp}) and differential intensity (ΔI_{pp}) of ErCrO ₃ with temperature	138
<i>Fig. 16:</i> The magnetic parameters spontaneous magnetization ($4\pi M_s$) and magnetic anisotropy field (H_k) of ErCrO ₃ as a function of temperature	139

LIST OF TABLES

TABLE NO.	DESCRIPTION	PAGES
CHAPTER 1		
<i>Table 1:</i>	Difference between Type-I and Type-II Multiferroics	8
<i>Table 2:</i>	Some common multiferroic with their T_C , T_N and polarization	9
<i>Table 3:</i>	List of rare earths elements with their properties	12
<i>Table 4:</i>	Properties of Chromium	17
<i>Table 5:</i>	$RCrO_3$ (Rare-earth, Y and La) compounds with the respective Néel temperatures	18
<i>Table 6:</i>	Magnetic moment configurations of $RCrO_3$	25
<i>Table 7:</i>	Compatible spin configurations in $RCrO_3$ for $T \geq T_N^{RE}$	26
<i>Table 8:</i>	$RCrO_4$ (Rare-earth, Y and La) compounds with the respective Curie/ Néel temperatures	32
CHAPTER 3		
<i>Table 1:</i>	Obtained lattice parameters a, b, c and volume of the unit cell of $RCrO_4$ (R = Sm, Eu, Gd, Dy, Er)	74
<i>Table 2:</i>	Obtained lattice parameters a, b, c and volume of the unit cell of $RCrO_3$ (R = Sm, Eu, Gd, Dy, Er)	77
<i>Table 3:</i>	The approximate particle sizes of $RCrO_4$ and $RCrO_3$ nanoparticles	80
<i>Table 4:</i>	The weight percentage and atomic percentage of R, Cr and O in $GdCrO_4$ and $ErCrO_3$ nanoparticles	83

CHAPTER 4

<i>Table 1:</i> Curie-Weiss constant, C_{cw} , Curie-Weiss temperature, θ_{cw} , and calculated effective magnetic moment (μ_{eff}) for $R\text{CrO}_4$ nanoparticles	98
---	----

CHAPTER 5

<i>Table 1:</i> Curie-Weiss constant, C_{cw} , Curie-Weiss temperature, θ_{cw} , and calculated effective magnetic moment (μ_{eff}) for $R\text{CrO}_3$	114
---	-----

CHAPTER 6

<i>Table 1:</i> The observed values of the resonance field, H_{res} , the line-width, ΔH_{pp} and differential intensity, ΔI_{pp} at 373 K	130
---	-----

Chapter 1

Introduction

1.1 A Brief History of Multiferroics

In recent times, scientists and engineers are engaged in extensive research to discover materials with new properties that have a direct bearing on the advancement of technology. Magnetoelectric multiferroics constitute a class of novel materials in which interaction between coupled electric and magnetic dipoles (with two order parameters) leads to magnetoelectric effect [1–5]. As we all know that electricity and magnetism plays a very important role in our day to day life. In fact, thinking about the absence of these would make a vast difference on our lives. As per the opinion of Daniel Khomskii, electricity and magnetism were combined into one collective order way back in the early 19th century which was described in the form of Maxwell’s equation. However, researchers thought it would be difficult to find a material that can combine the properties of ferroics which are ferroelectricity, ferromagnetism and ferroelasticity [1]. The popularity of multiferroics became more since when Hans Christian Oersted accidentally discovered it in 1820 when he was switching on/off the battery kept nearby the compass needle. He found that the needle of the compass deflected by the switching of the battery. Only after studying for 40 years by many scientists including Andre Marie Ampere, Michael Faraday and James Maxwell on multiferroics approved the result as a Maxwell’s unified theory [2].

1.2 Present Discussion on Multiferroics

For the fulfillment of the needs of human race and the environment, innumerable amount of research has been made and is still on go. One of the most talked topic where the compound consist a substantial range of properties including, superconductivity, ferroelectricity, magneto resistance, strongly correlated electron behavior, magnetism etc. is multiferroic material. So basically, multiferroic material is a material which consists of more than one ferroic nature and that may be ferroelectricity, ferromagnetic or ferroelastic. Ferroic is a material that acquires a spontaneous, switchable internal alignment that may be spin or charge by some external field. However in our current discussion/work we are excluding the ferroelasticity. Instead, the thesis work has been focused mainly on ferromagnetic and ferroelectricity. The accepted definition for ferroelectricity is the one which undergoes a phase transition from a high-temperature phase that behaves as an ordinary dielectric (so that an applied electric field induces an electric polarization, which goes to zero when the field is removed) to a low-temperature phase that has a spontaneous polarization whose direction can be switched by an applied field [3]. In ferroelectricity, the internal charge can be adjusted by the external electric field. And also, ferroelectricity occurs when the metal ions have empty d shell-orbital [4]. On the other hand, a ferromagnetic material is one that undergoes a phase transition from a high temperature phase that does not have a macroscopic magnetic moment to a low temperature phase that has a spontaneous magnetization even in the absence of an applied magnetic field [3]. And also, the ferromagnetic nature occurs when the metal cations have partially filled d-orbital. In ferromagnetic, the internal spin can be aligned by the external magnetic field. In recent years, with a high demanding technology, one of the interesting tasks is to create a storage

media (like hard drive) with higher density. Currently, besides ferromagnetic, ferroelectric is the material that are highly used for the data storage media in gadgets.

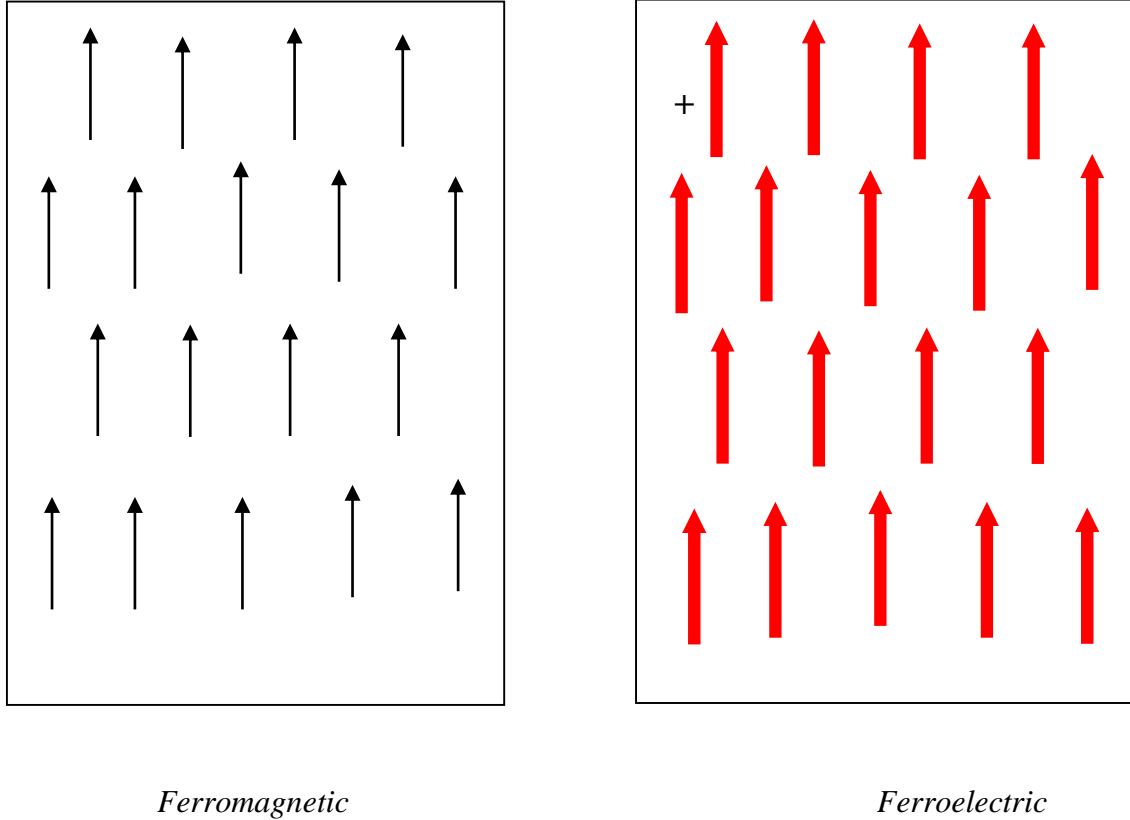


Fig.1. Structure of ferromagnetic and ferroelectric

So it began as the matter of concern to think about the combination of the properties of ferromagnetic and ferroelectric to get unique material that can provide both nature of ferromagnetic as well as ferroelectric. Figure 1 is the simplest structure of ferromagnetic material and ferroelectric material. In addition the management of replacing the magnetic field by electric field pulse to control the magnetic state would lead to reduced power consumption which indirectly helps in economic growth. On the other hand, combination of magnetism and electricity can also be found in some other material such as magnetoelectric material and electromagnetic material. These materials almost have the

same properties as of multiferroic material. In magnetoelectric material the electric dipoles are controlled by external magnetic field where as in electromagnetic material the magnetic dipoles are controlled only by an external electric field. But in multiferroic material magnetization is controlled by both electric field and magnetic field and polarization is controlled by both magnetic field and electric field. In other words we can say that, when these two phenomena i.e. magnetoelectric and electromagnetic are present in the same material, it is called as multiferroic material [5, 6]. Magnetoelectric and electromagnetic materials form a compact subclass of multiferroics. In these materials, there is a fusion between the electric and magnetic order parameters, and the application of a magnetic field induces electric polarization. In magneto dielectrics, the capacitance of a material is affected by an external magnetic field. A multiferroic may or may not be magnetoelectric but may exhibit magneto capacitance. We must note that the magneto dielectric effect can also have a resistive origin arising from the Maxwell-Wagner effect and magnetoresistance [7]. Figure 2 shows the absolute representation of multiferroic orderings where yellow loop is the ferroelectric material and blue loop is the ferromagnetic material and green one is the multiferroic ordering. As we can see clearly that in ferroelectric, the polarization is control by electric field and in ferromagnetism; the magnetization is control by magnetic field. But in case of multiferroic material, the polarization is control by electric field as well as magnetic field. And also there magnetization is control by magnetic field as well as electric field. [1]. Basically, in a proper and clear way if we want to understand the phenomena of multiferroic materials we have to go through a term electromagnetic and magnetoelectricity. If there is a material with an electric dipole with a different direction

that state is called as paraelectric and when it orients in a same direction, it is known as ferroelectric state.

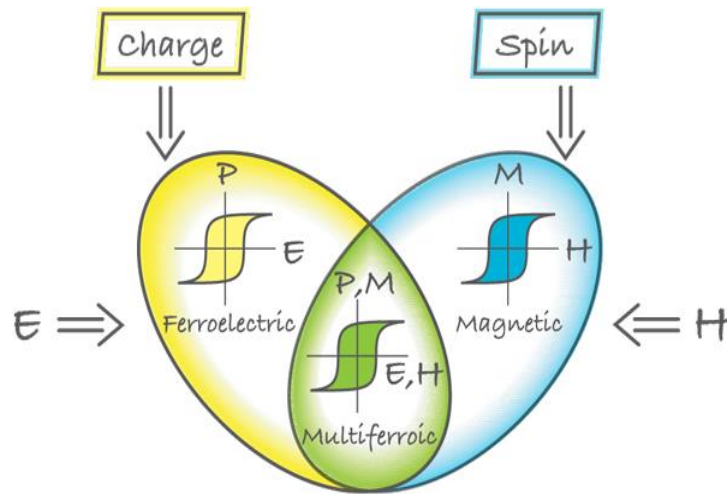


Fig.2. Multiferroics combines the properties of ferroelectrics and ferromagnetics

Now, if we can be able to orient the direction of this dipole according to our own way by applying external magnetic field then this will be called as magnetoelectric effect. In the same way, when we can control the magnetic dipole by applying an external electric field then it can be called as electromagnetic effect. So when these two phenomena exist in the same material we can consider that to be a multiferroic material. The first multiferroic material was confirmed in the year of 1959 – 1960. The theoretical parts were pledged by Dzyaloshinskii and the experimental part by Astrov. In general, the multiferroic material describes the coupling between the magnetic field and an electric field. Below is the equation which relates the work of electric field and magnetic field, these equations from

1–3 were found by Landau which is also known as Landau theory of equation for magnetoelectric effect [8]

$$P(\vec{E}, \vec{H}) = F_0 - P_i^s E_i - M_i^s H_i - \frac{1}{2} \epsilon_0 \epsilon_{ij} E_i E_j - \frac{1}{2} \mu_0 \mu_{ij} H_i H_j - \alpha_{ij} E_i H_j - \frac{1}{2} \beta_{ijk} E_i H_j H_k - \frac{1}{2} \gamma_{ijk} H_i E_j E_k \dots (1)$$

Where, F_0 is the ground state free energy

Subscripts (i, j, k) refer to the three components of a variable in spatial coordinates.

E_i and H_i are the components of the electric field \vec{E} and magnetic field \vec{H} , respectively;

P_i^s And M_i^s are the components of the spontaneous polarization P^s and magnetization M^s

μ_0 are the dielectric and magnetic susceptibilities,

β_{ijk} and γ_{ijk} are the third-order tensor coefficients and,

Most importantly, α_{ij} is the component of tensor $\hat{\alpha}$. The tensor $\hat{\alpha}$ corresponds to induction of Polarization by a magnetic field or magnetization by an electric field which is designated as the linear magnetoelectric effect. The rest of the terms in the preceding equations correspond to the high-order magnetoelectric effects parameterized by tensors β and γ .

The differentiation of equation (1) leads to the polarization

$$P_i(E, H) = \frac{\partial F}{\partial E_i} = P_i^s + \epsilon_0 \epsilon_{ij} E_j + \alpha_{ij} H_j + \frac{1}{2} \beta_{ijk} H_j H_k + \gamma_{ijk} H_i E_j + \dots, \dots (2)$$

And to the magnetization,

$$M_i(E, H) = -\frac{\partial F}{\partial H_i} = M_i^s + \mu_0 \mu_{ij} H_j + \alpha_{ij} E_j + \beta_{ijk} H_j E_i + \frac{1}{2} \gamma_{ijk} E_j E_k + \dots, \dots (3)$$

1.3 Types of Multiferroics

Researchers already found out that the multiferroics are divided into two groups which are Type-I Multiferroics and Type-II multiferroics.

Type-I Multiferroics: As per the research till now, the ferromagnetism and ferroelectricity have different origin in type-I multiferroics and often occurs due to a different active sub system of a material. The ferroelectricity can have much microscopic origin in this type of multiferroics. Also in such type of multiferroics, magnetic order parameters, breaking spatial inversion symmetry, breaking time reversal symmetry and the ferroelectric parameter coexists and have certain coupling between them. The ferroelectricity is generated due to (i) the compound like BaTiO_3 where the transition metal (TM) with d^0 configuration is present (ii) the presence of lone pairs of Bi^{3+} and Pb^{2+} where the ferroelectric (FE) is predominant (iii) the presence of geometric ferroelectricity such as in YMnO_3 compound, where FE is caused by a rotation of rigid M -O polyhedra (in this case MnO_5 trigonal bi-pyramids). To make it clear, in this type-I multiferroic material the ordering of ferroelectricity is very much higher than that of the ferromagnetic ordering.

Type-II multiferroics: For Type-II multiferroic material there is a condition where the ferroelectricity can occur only in the magnetically ordered state that is at the same temperature FE sets in as a certain type of magnetic ordering and is driven by it. Type-II multiferroicity can give rise up by, for example, Spiral magnetic ordering, there may have two microscopic origins for magnetically driven FE in type-II multiferroics. Probably the most common among them works in systems like $\text{Ni}_3\text{V}_2\text{O}_8$, MnWO_4 and TbMnO_3 in multiferroic pyroxenes and in some other systems. Inverse Dzyaloshinskii- Moriya effect

interaction is the mechanism of FE materials. And it usually operates in systems with non-collinear, usually spiral magnetic structures of a certain type. It requires the direct action of the relativistic spin-orbit interaction. A second possible mechanism does not require the presence of spin-orbit coupling; and works for collinear magnetic structures and it is based on magnetostriction. To have a multiferroic behavior for the magnetostriction, the presence of inequivalent magnetic ions is required, with different charges. These, in turn, may be either just different TM ions, or the same element in different valence states [9]. Below we have given few points that could enlighten us the difference between Types-I and Type-II multiferroics [1].

Table 1: Difference between Types-I and Type-II multiferroics.

Type-I	Type-II
<ul style="list-style-type: none"> ➤ weak coupling of ferroelectricity and magnetism ➤ ferroelectricity at higher T than magnetism ➤ large P(polarization) ➤ “old” multiferroics 	<ul style="list-style-type: none"> ➤ strong coupling: polarization changes with H field ➤ ferroelectricity in low-temperature regime ➤ weak P(polarization) ➤ “new” multiferroics

And also, we have listed some already existed multiferroics compound in table 2 [10]. Among all the mentioned multi-ferroics listed below, $BiFeO_3$ is the only material that is both magnetic and strong ferroelectric at room temperature. As a result; it has an impact

on the field of multi-ferroics that is comparable to that of *yttrium barium copper oxide* (YBCO) on superconductors, with hundreds of publications devoted to it in the recent past [11].

Table 2: Some common multiferroic with their T_C , T_N and polarization

Sl. No.	Material	$T_{FE}(K)$	$T_M(K)$	$P(\mu Ccm^{-2})$
1	BiFeO ₃	1100	643	6.1
2	YMnO ₃	914	76	5.5
3	HoMnO ₃	875	72	5.6
4	TbMnO ₃	28	41	0.06
5	TbMn ₂ O ₅	38	43	0.04
6	Ni ₃ V ₂ O ₈	6.3	9.1	0.01

1.4 Advantages, Disadvantages and Applications of Multiferroic Materials

Since the past decade, the dramatic progresses in the fundamental physics of magneto electrics and multiferroics have become very high and sensible. The first initial starter from a technology perspective for multiferroic materials was the potential to control and manipulate ferromagnetism with electric fields. This became one of the most important topics to focus because of its tremendous impact in areas as diverse as sensing, information storage, actuation, and spintronics due to the significance of less power consumption where the magnetic spins are controlled more by the electric field than the magnetic-field, which

requires electric currents to generate the magnetic fields [12, 13]. The most challenging and the demanding task for the researchers is to find the mechanism that gives a large coupled magnetization and polarization, merged with large susceptibilities at low magnetic field or electric field which should be at room temperature. Though, in literature there may have some results of single phase room temperature multiferroics but still the production is quite hard as for the reports of room temperature superconductors. Yet, multiferroics continue to disclose the degree of realism, unlike in physics and the capable applications of multiferroics are stretched far beyond the electrical control of ferromagnetism. The current or recent discoveries such as electrical conduction, magneto transport, and the vortex formation forward the possibility of electrically controllable nanoscale storage or logic elements. In multiferroic structures the electrical control of resonances has already led to prototypes of electrically controlled microwave devices. The antiferromagnetic resonance frequencies ranges between the hundreds of giga-hertz in the orthoferrites (the parent compounds of BiFeO_3) suggesting the possibility of controlled electric-field frequencies up to tera-hertz, an area that is essentially unexplored. The palette of parameters for tuning, coupling, and controlling functionalities can be extended by the range of addressable order parameters including orbital ordering, chirality and toroidal or higher-order multipolar orderings, and identifying their associated conjugate fields. The recent progress on the basic materials on aspects of physics may lead to the stimulation of the physics community to exploit entirely new device paradigms for the cause of novel and unique functionalities of multiferroics [14]. Usually a multiferroic material that we have studied falls into a class of materials known as complex oxides. These are the compounds with the fusion of two or more metal cations (mostly 3d-4f) and oxygen. It is a matter of

fact that, complex oxides are attractive because of their chemically inert and non-toxic nature and abundance of their constituent elements. Scientifically, the intermediate ionic-covalent nature of transition metal-oxygen bonds leads to strong polarizability which could cause a super exchange interaction between the transition metal ions which is an advisable property in ferroelectrics. The highly localized transition-metal $3d$ electrons leads to the so-called strong correlation physics commonly associated with exotic magnetic behavior. But also worthy of exploration are other material classes, including fluorides, which featured prominently in the early history of multiferroics, and organics and selenides, which are currently showing promising early results [15, 16].

1.5 Rare earth and transition metals

Rare earths are a chain of chemical elements found in the earth's crust that are essential to many modern technologies, including computers and networks, consumer electronics, environmental mitigation, communications, clean energy, advanced transportation, national defense, health care and many others. Not only that, because of their unique electrochemical properties, magnetic and luminescent, these elements help many technologies to perform with reduced weight, reduced emissions, and energy consumption; or give them greater efficiency, performance, miniaturization, speed, durability, and thermal stability. And also, rare earth enabled products and technologies to enhance fuel global economic growth, maintain high standards of living, and even save lives. There are 16 elements that are considered to be rare earth elements, 14 elements in the lanthanide series and two additional elements which are yttrium and lanthanum, that share similar chemical properties.

Table 3: List of rare earth elements with their properties [17].

Sl. No.	RE elements	symbol	Atom. No.	Heavy/light	Atom. weight	Melting point (°C)	Elec. conf. (R ³⁺)
1	Yttrium	Y	39	Heavy	88.90	522	4d ¹ 5s ²
2	Lanthanum	La	57	Light	138.90	918	5d ¹ 6s ²
3	Cerium	Ce	58	Light	140.11	798	4f ¹ 6s ²
4	Praseodymium	Pr	59	Light	140.90	931	4f ² 6s ²
5	Neodymium	Nd	60	Light	144.24	1021	4f ³ 6s ²
6	Promethium	Pm	61	Light	145.00	1042	4f ⁴ 6s ²
7	Samarium	Sm	62	Light	150.36	1074	4f ⁵ 6s ²
8	Europium	Eu	63	Light	151.96	822	4f ⁶ 6s ²
9	Gadolinium	Gd	64	Heavy	157.25	1313	4f ⁷ 6s ²
10	Terbium	Tb	65	Heavy	158.92	1356	4f ⁸ 6s ²
11	Dysprosium	Dy	66	Heavy	162.50	1412	4f ⁹ 6s ²
12	Holmium	Ho	67	Heavy	164.93	1474	4f ¹⁰ 6s ²
13	Erbium	Er	68	Heavy	167.26	1529	4f ¹¹ 6s ²
14	Thulium	Tm	69	Heavy	168.93	1545	4f ¹² 6s ²
15	Ytterbium	Yb	70	Heavy	173.04	819	4f ¹³ 6s ²
16	Lutetium	Lu	71	Heavy	174.97	1663	4f ¹⁴ 5d ¹ 6s ²

The total number of rare earth elements is listed in the table. The rare earths form a remarkable interesting group of elements in the so far listed periodic table. Almost all the rare earths have three electrons in the conduction band or valence shell, starting from cerium to lutetium, as the atomic number increases the inner 4f shell is gradually filled up. The interesting features in the field of electric and magnetic properties of rare earths are mostly arising from the unfilled 4f shell. To make it clear, we can say that the properties have a smooth dependence on the number of electrons in the shell. Usually at room temperature, most of the rare earth metals are paramagnetic in nature [17]. When the temperature is lowered than the room temperature the particular rare earths such as dysprosium, holmium, erbium and thulium exhibit a transition to an ordered magnetic state and have a very complicated structure known as antiferromagnetic. But on decreasing the temperature gradually it faces another transition and become ferromagnetic in nature. On the other hand, gadolinium and terbium become ferromagnetic below 289 K and 230 K respectively. Around 10 K cerium, neodymium, and samarium transform into antiferromagnetic in nature. According to the literature, no other ordered state has been found in other elements of the group. The magnetic properties that we have observed in these elements are primarily due to the incomplete shell. The basic concept to find the magnetic moment per atom is the number of electrons in the 4f shell according to the Russell-Saunders coupling scheme. But, in order to understand the antiferromagnetic or ferromagnetic coupling in magnetic rare earth elements we have to consider the other effects also. As we already know that in this kind of metals the 5s and 5p shells are completely surrounding the 4f shell of each ion. Due to a very little chance of magnetic shells to overlap with each other, direct exchange effect between neighboring ions must be

very small. That is why we are considering the other mechanism behind the strong coupling in magnetic rare earth elements. Indirect exchange coupling via conduction electrons is considering being one such mechanism which is predicted to be the most crucial key role for the interaction [18]. Below we have described this interaction briefly, first with the help of electrostatic Coulomb exchange effect, a 4f shell electrons of an ion first interacts with a conduction electron. And this compels the spin of the conduction electron to align parallel or anti parallel to the spin of ion. In the crystal when the electrons are moving it may also interact with the other ion inside the crystal, when it happens it give rise to a force which inclines to align all the ions in the crystal and due to these phenomena long range type of coupling occurs. Also, many other properties of rare earth are believed to exist due to the interaction between the 4f shell electrons (s-f interaction) and the conduction electrons [19].

The next element which is very important for this present doctoral thesis is the transition metal ions. Due to their strong inter-atomic metallic bonding, the transition metals has a high melting point, boiling point and high tensile strength and that is why it became one of the most important industrial metals. There are 38 transition metal elements so far in the periodic table. Even in these metals with change in atomic number the chemical properties of the transition element do not visibly change. The main attractive and notable nature of the compounds of transition metal ions is their color. Almost all the compounds that are made of transition metal ions including vanadium, chromium, manganese, iron, cobalt, nickel and copper are vigorously colored, including the atomic number of the metallic element. The color also depends on the oxidation state and to some degree of extent it may also depend on the non-metallic element or acidic radical along with which the transition

metal ions combined to form a compound. Another interesting property of transition metal ions is the incomplete inner shells. Virtually all the compounds that are made by transition metal elements corresponding to the presence of incomplete inner shells are strongly paramagnetic. If we study thoroughly, though the compounds of transition metal ions are functional to the human race but we also cannot deny the truth that the transition metals themselves and their alloys are very significant in the development of industrial growth. Since decades and still, our modern civilization is deployed on steel and iron. And the important part is that, the steel is made up of other transition metals which include vanadium, chromium, manganese, cobalt, nickel, molybdenum, wolfram etc. The strength and the hardness of these alloys made it very important to the development. These properties are the result of a very strong bonding between the atoms inside the metals. Compared to the other 3d block elements, zinc has a low melting point and a lower tensile strength. Even though scandium is physically typical transition metal for example high tensile strength, high melting point but chemically it only forms a single and colorless triple charged ion (Sc^{3+}). Likewise zinc also does not show any typical characteristics of transition metal chemistry e.g. variable oxidation state, colored complex ions, and catalytic properties of the metal or ion. So, from the above discussion the most appropriate definition of a transition metal is an element which forms at least one ion with an incomplete d sub-shell containing at least one electron. Therefore the properties which transition metals possess are due to the partially filled d sub-shells of electrons which other group element does not have namely, group 1–7. But if we see properly then it has a similar nature with group 2, 3 and 4. As we have already discussed that transition metal has a high value in the field of industry due to their strength arising from the strong inter-atomic

forces. The main cause of their high tensile strength, ductility (can be drawn into wire) and malleability (can be readily beaten into shape) is the delocalized 3d or 4s electrons contributing to the bonding. And due to small ionic radii the transition metal ions have a strong bonding. If we talk about the color all the transition metals have a silver grey color in nature excluding copper with a dark orange in color. Due to their high melting point, boiling point and densities, they form enormous variety of alloys with an extensive range of uses based on their hardness, strength, malleability and anti-corrosion properties. These are the reasons which lead to be an interesting topic for the researchers to discern the nature of the forces that hold the metal atoms together in these metal and alloys [20]. But in the present thesis work, we have chosen chromium among all the other transition elements. In the further research we may include some other transition elements. Chromium is one of the representative transition element in the first long period of the periodic table. They are neither so well-known nor as important as some other transition elements (eg. Iron and nickel) but the chemistry within this element is very interesting. The principal oxidation state of chromium is represented as figure 3 in the following diagram. One of the most important ore of chromium is chromite, FeCr_2O_4 . The element was not known to the ancients, but was discovered in 1798 in lead chromate PbCrO_4 , which occurs in nature as the mineral crocoites. In table 4 the basic information including symbol, atomic no., atomic mass no., melting point, boiling point and electronic configuration has been given.

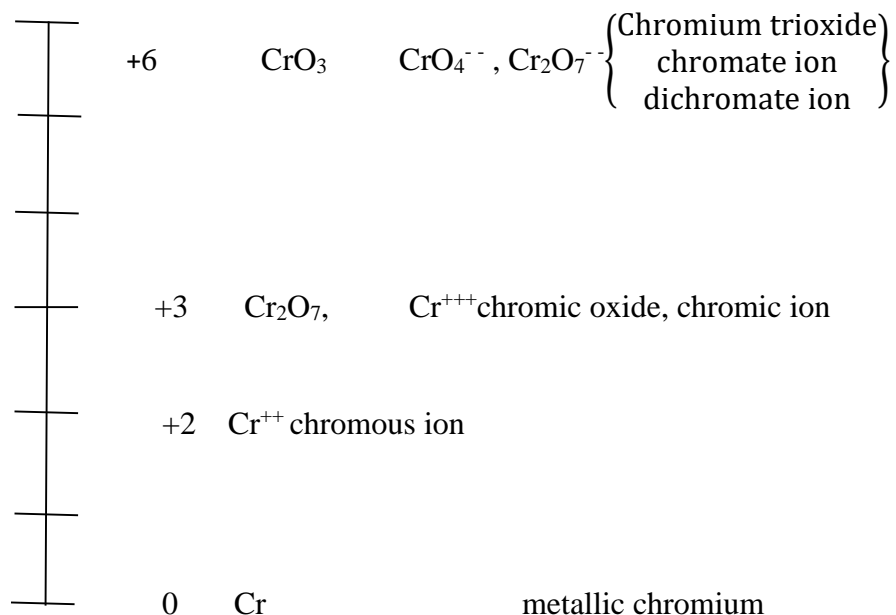


Fig. 3. Different oxidation states of chromium

Table 4: Properties of Chromium [20]

symbol	Atom. no.	Atom. mass no.	Melting point	color	Electronic conf. (Cr^{3+})
Cr	24	51.996 g.mol ⁻¹	1907 °C	Silver-gray	4s ⁰ 3d ³

So the properties of rare earth and transition metal ions are one of the most attractive and an interesting research field in terms of their own particular properties in electronic correlation and magnetic properties.

The compound which we have proposed for this thesis work is the fusion of rare earth (Er, Dy, Gd, Eu, Sm) and the transition metal ions which is chromium in our case. In table 5 we

have listed some compounds of RCrO_3 with their Néel temperature where the properties of the compounds changes its nature [21–29].

Table 5: RCrO_3 (R =Rare earth, Y and La) compounds with the respective Néel temperatures

RCrO_3	Ce	Pr	Nd	Pm	Sm	Eu	Gd	Tb
T_N^{Cr} (K)	260	237	214	—	198	181	168	167
RCrO_3	Dy	Ho	Er	Tm	Yb	Lu	Y	La
T_N^{Cr} (K)	145	142	135	127	115	111	141	295

1.6 Magnetic Structure of Rare earth Orthochromites, RCrO_3

Rare earth transition metal oxides have been manifested to be one of the most relevant groups of materials due to their mechanical, dielectric, optical and magnetic properties. Rare earth orthochromites, RCrO_3 (R = rare earth/ Yttrium), isostructural orthoferrites, RFeO_3 are such class of oxides that got the attention of researchers due to their electronic correlations with unusual magnetoelectric properties [6–9]. They are of great interest notably due to the observed high coercive fields when deposited in the form of thin films [12]. The rare earth orthochromites RCrO_3 (where R stands for a rare earth metal) are isostructural with the rare earth orthoferrites, RFeO_3 , and crystallize in an orthorhombic distorted perovskite structure. Here when we talk about RCrO_3 there can be two possibilities. When R is nonmagnetic (Y, La) there will be only one interaction which is $\text{Cr}^{3+}-\text{Cr}^{3+}$ interaction. This magnetic interaction is arises only because of B-site Cr^{3+} ions.

So the magnetic interaction of RCrO_3 when the rare earth is nonmagnetic is given in the equation below [30, 31]

$$E = \lambda \mathbf{M}_1 \cdot \mathbf{M}_2 - \mathbf{H} \cdot (\mathbf{M}_1 + \mathbf{M}_2) - \mathbf{D} \cdot (\mathbf{M}_1 \times \mathbf{M}_2) - \left(\frac{K_b}{M_0^2} \right) (M_{1x}^2 + M_{2x}^2) \quad \dots (4)$$

Where

$M_0 = |\mathbf{M}_1| = |\mathbf{M}_2|$, \mathbf{M}_1 and \mathbf{M}_2 being each Cr-sub-lattice magnetization.

1st term – the isotropic Heisenberg exchange which is responsible for anti-ferromagnetic ordering

2nd term – the interaction of magnetic moments with the applied field

3rd term – the anti-symmetric DM interaction, which is a minimum when each sub-lattice magnetization \mathbf{M}_1 and \mathbf{M}_2 and the \mathbf{D} vectors are mutually perpendicular, and the

Last term – magneto crystalline anisotropy.

The analysis made by R.M Honreich et al also finds out the relative spin structure of RCrO_3 when R is non-magnetic (La, Y). According to them the Hamiltonian of the Cr spins can be written as [32]

$$\begin{aligned} H = 2J \sum_{\langle ij \rangle} \vec{S}_i \vec{S}_j - \vec{D} \sum_{\langle ij \rangle} \vec{S}_i \vec{S}_j \sum_{\langle ij \rangle} \vec{S}_i \vec{S}_j - A_{xz} \left(\sum_i S_{ix} S_{iz} - \sum_j S_{jx} S_{jz} \right) \\ - K_2 \sum_i S_{iz}^2 - g \mu_B \vec{H} \cdot \sum_l \vec{S}_l \quad \dots (5) \end{aligned}$$

Where \vec{S}_i is a spin in one sublattice

\vec{S}_j Belongs to the other sub-lattices

\vec{S}_l Belongs to either of the sublattices, the l summation extends over all spins and the (ij) summation extends over pairs of nearest neighbour spins. Here, \vec{D} is the Dzyaloshinskii vector, the subscripts x, y, z refer to the orthorhombic a, b and c axes. The constants J , D , A_{xz} , K_2 will be regarded as adjustable parameters. The first and second term is isotropic nearest-neighbour and the Dzyaloshinskii-Moriya exchange interactions, the third and fourth terms are due to quadratic anisotropy. As a result of the third term, the two sublattices will have different easy directions in the a-c plane. The fourth fixes c as the anti-ferromagnetic axis of the system. The final term is the direct interaction of the spins with the external magnetic field. When R is magnetic, there exist three magnetic interactions between rare earth and chromium ions which are given by a) $R^{3+}-R^{3+}$ interaction, b) $R^{3+}-Cr^{3+}$ interaction and c) $Cr^{3+}-Cr^{3+}$ interaction.

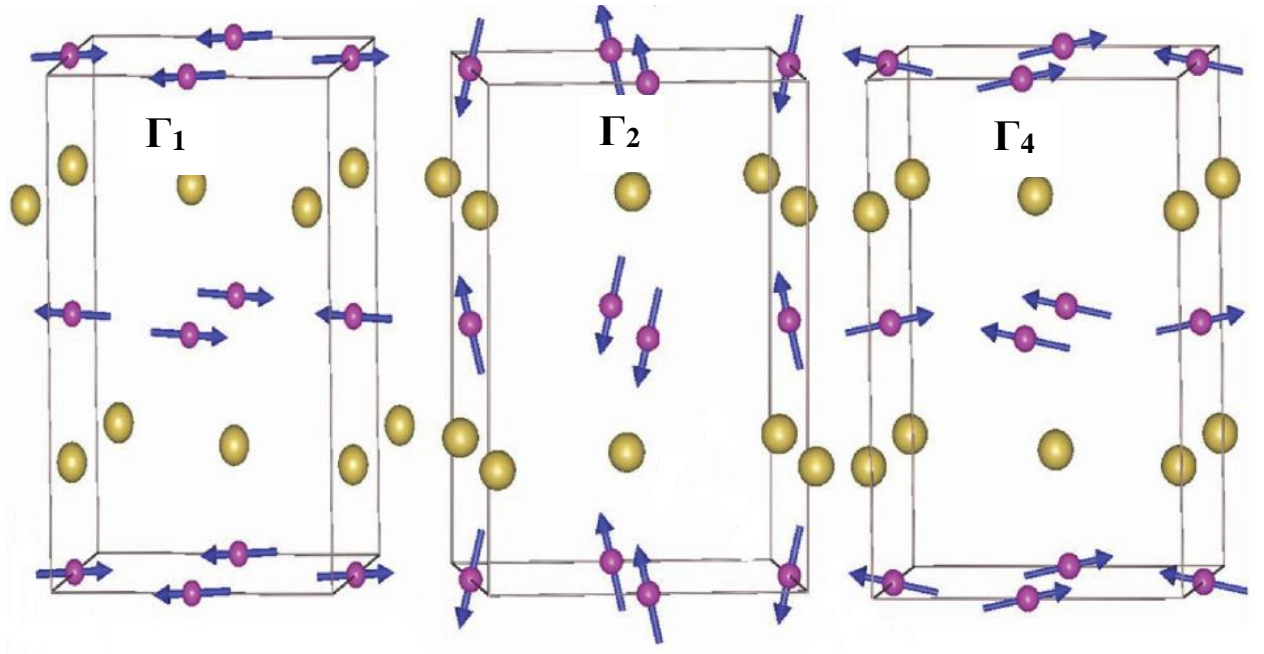


Fig.4. Possible Spin structures of $RCrO_3$ [23]

Among these three interaction, $\text{Cr}^{3+} - \text{Cr}^{3+}$ interaction are considered as the strongest one which is the cause of antiferromagnetic nature with some canting in it or we can say a weak ferromagnetism. The second dominating interaction is $\text{R}^{3+} - \text{Cr}^{3+}$ interaction and third one is between $\text{R}^{3+} - \text{R}^{3+}$ interaction [30]. We know that the crystal structure of a solid is very vast and it has been divided into some categories. Bertaut has classified a crystal structure according to their spin structure [23]. The types of spin structure classified are said to be $\Gamma_1, \Gamma_2, \dots, \Gamma_8$. Among these Bertaut notation RCrO_3 fall under Γ_1, Γ_2 and Γ_4 depending upon the rare earth ions. Figure 4 shows the spin structure of RCrO_3 as per Bertaut notation. Here if we see the first part of this diagram which is Γ_1 , the spins are just opposite to each other or we can say that the angle between the spins is 180 degree. These kinds of spins are found when we have an anti-ferromagnetic (AFM) structure. And when we see the other two parts of the same figure i.e. Γ_2 and Γ_4 the spins are not exactly opposite to each other or say the angle between the spins is not 180 degree. These types of spin structure are evolved in the canted antiferromagnetic material (CAFM). According to the literature, When the rare earth is non-magnetic (LaCrO_3 and YCrO_3) the spin structure is Γ_4 and it is due to the $\text{Cr}^{3+} - \text{Cr}^{3+}$ interaction. When the rare- earth is magnetic the spin structure could be either Γ_2 or Γ_1 . But among the entire RCrO_3 compound, ErCrO_3 only falls on the collinear antiferromagnetic order which is Γ_1 . So the rest of the RCrO_3 compounds are considering being in Γ_2 and Γ_4 spin structure [23]. Many researchers have already studied about the multiferroic nature of RCrO_3 including B. Rajeswaran et al which is given elsewhere [23]. They have shown that the temperature dependence of magnetization of RCrO_3 under field-cooled conditions with an applied magnetic field of 100 Oe. The distinguished behavior is characteristic of antiferromagnetic ordering of Cr

moments T_N^{Cr} with weak ferromagnetism. They had observed the magnetic ground state is $\Gamma_2 (F_x, C_y, G_z)$ for $RCrO_3$ with magnetic rare earth except erbium. For $R = Er$, the magnetic ground state is found to be collinear antiferromagnetic with $\Gamma_1 (A_x, G_y, C_z)$ spin structure. It is noteworthy that in the case of $LaCrO_3$ and $YCrO_3$ with nonmagnetic R ions no intrinsic electric polarization is observed. In addition to the magnetic R ion, they show that the weak ferromagnetism of the Cr sublattice is also essential for inducing polarization in these orthochromites. They have observed dielectric anomalies both at T_N and at T_{SR} confirming the magnetoelectric coupling. Interestingly, the electric polarization measured disappears along with the weak ferromagnetism below T_{SR} , which demonstrates that the weak ferromagnetism of the Cr sublattice is essential for inducing electric polarization. However, the polarization below T_{SR} is revived by cooling the sample under an applied magnetic field (± 2 T). The applied magnetic field suppresses the spin reorientation and thus the weak ferromagnetic state and the polarization remain down to the lowest temperature.

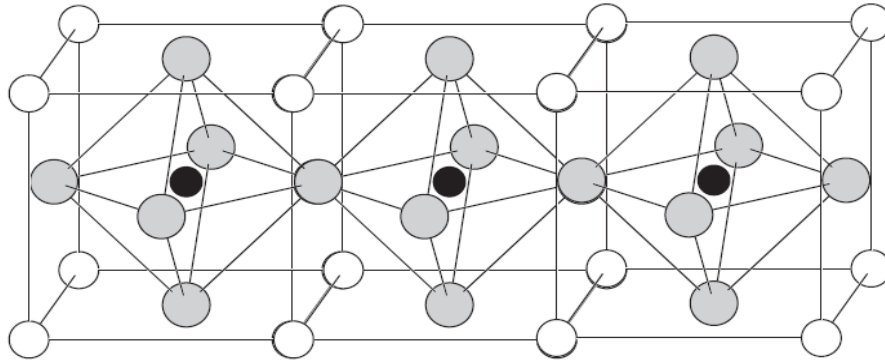


Fig.5. Orthorhombic structure of $RCrO_3$

Figure 5 shows the crystal structure of $RCrO_3$ which is distorted into an orthorhombic structure with space $pbnm$ group. The figure given above shows the transition metal ions

as black circles, rare earth as white circles and Oxygen atoms as grey circles. In the figure we can clearly see that in order to interact with one transition metal ion with another transition metal ion it passes through the oxygen atom, this type of interaction is known as super exchange interaction.

Figure 6 shows the polyhedral structure of RCrO_3 compound that shows the way of R, Cr and O atoms are connected magnetically. Due to the mechanical, dielectrical and magnetic properties of rare earth orthochromites (RCrO_3) it has become an attractive compound for researchers worldwide. The rare earth orthochromites have unusual magnetic properties due to its dependency on the rare earth such as gadolinium (Gd), Erbium (Er), Europium (Eu) etc which leads to a complete change of the magnetic properties. As the above discussion, when the rare earth is non-magnetic there exist only one interaction where as when the rare earth is magnetic there exists three interactions. The magnetic nature of rare earth controls the magnetic nature of chromium. So by controlling the use of different rare earths we can have a different Néel temperature or critical temperature. In a very low temperature say up to around 10 K, rare earth shows a paramagnetic nature, they do not align themselves into antiferromagnetic/ferromagnetic nature. Rare earth can show different magnetic nature only at a very low temperature. In all the higher state it is fully paramagnetic. In addition to this, the compound of RCrO_3 is captivating due to a distinguished coercive field that arouse in the presence of low magnetic field [33]. The rare earth (R^{3+}) occupies the A-site of a crystal with an electronic configuration $\text{R}^{3+} (4f^{4-14})$ (electronic configurations are given in table no.3). While with an electronic configuration of $(4s^0 3d^3)$ the chromium (Cr^{3+}) ion occupies octahedral B site of the crystal.

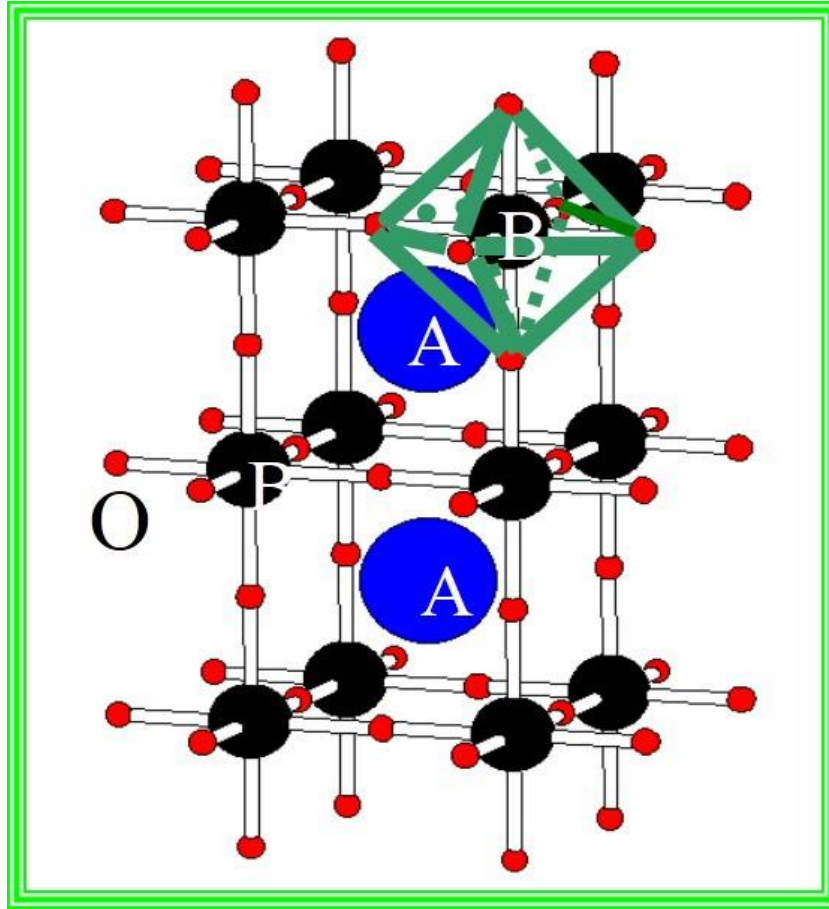


Fig.6. Polyhedral crystal structure, RCrO_3 .

The possible magnetic Configurations with crystal symmetry for RCrO_3 are found as D_{2h}^{16} and these were studied by Wollan, Koehler and by Bertaut. In the table 6 and 7 the possible magnetic configurations and their magnetic symmetry has been given [34]. The magnetic moment configurations sites are numbered in the following table, the positive (+) symbol indicates the parallelism of a magnetic moment to a particular direction and the negative (-) symbol represents the anti-parallelism of a magnetic moment to the same directions. Scientists has been working on magnetic structure of orthochromites (RCrO_3) by using neutron elastic scattering (NES) measurements on powder samples and also on spontaneous magnetization and susceptibility(SMS) measurements on a single crystal. The

result we got through the literature surveys are given in Table 7. It has listed the possible magnetic structures in the (4b) and (4c) positions in D_{2h}^{16} with symmetry isomorphic with D_{2h}^{16} with x,y,z designates a G configuration with the spin axis along a,b,c conventional cell of $pbnm$ structure respectively. The A, C and G indicate the A-, C- and G- type antiferromagnetic arrangements and the ferromagnetic is denoted by F symbol.

Table 6: Magnetic moment configurations of $RCrO_3$

Configuration designation	Site			
	1	2	3	4
F	+	+	+	+
G	+	−	+	−
A	+	−	−	+
C	+	+	−	−

At a certain temperature the spins of Cr^{3+} at the chromium sub-lattice undergoes a sudden transition. That transition temperature changes the properties of $RCrO_3$ from paramagnetic (PM) to antiferromagnetic (AFM) transition with the presence of canting between the spins at chromium sub-lattice [23, 35]. The cause of this transition is due to the interaction between neighboring Cr^{3+} spins that conducted to $\Gamma_4(G_x, A_y, F_z)$ which is a weak ferromagnetism and this kind of interaction is known as antisymmetric Dzyaloshinskii-

Moriya(DM) exchange interaction [36–39]. Above the Néel temperature of RCrO_3 the nature of the material is paramagnetic that means the magnetization is zero. In fact in all the paramagnetic material the magnetization value is zero. The magnetization of each sample increases from the Néel temperature due to the $\text{Cr}^{3+} - \text{Cr}^{3+}$ interaction. But at around 9 K the magnetization graphs decreases suddenly due to the magnetic anisotropy of rare earth which oppose the magnetization of Chromium and try to pull down the magnetization.

Table 7: Compatible spin configurations in RCrO_3 for $T \geq T_N^{\text{RE}}$.

Space group	Site							
	(4b) Cr					(4c) R		
Pbnm	Γ_1	A_x	G_y	C_z	-	-	C_z	
Pbn'm'	Γ_2	F_x	C_y	G_z	F_x	C_y	-	
pb'nm'	Γ_3	C_x	F_y	A_z	C_z	F_y	-	
pb'n'm	Γ_4	G_x	A_y	F_z	-	-	F_z	
pb'n'm'	Γ_5	-	-	-	G_x	A_y	-	
pb'nm	Γ_6	-	-	-	-	-	A_z	
pbn'm	Γ_7	-	-	-	-	-	G_z	
pbnm'	Γ_8	-	-	-	A_x	G_y	-	

The above statement suggests that at low temperature the magnetic anisotropy of rare-earth become very high which dominates the interaction of chromium (Cr^{3+}). In figure 7 the Rotation of magnetic vector during Spin-reorientation has been shown.

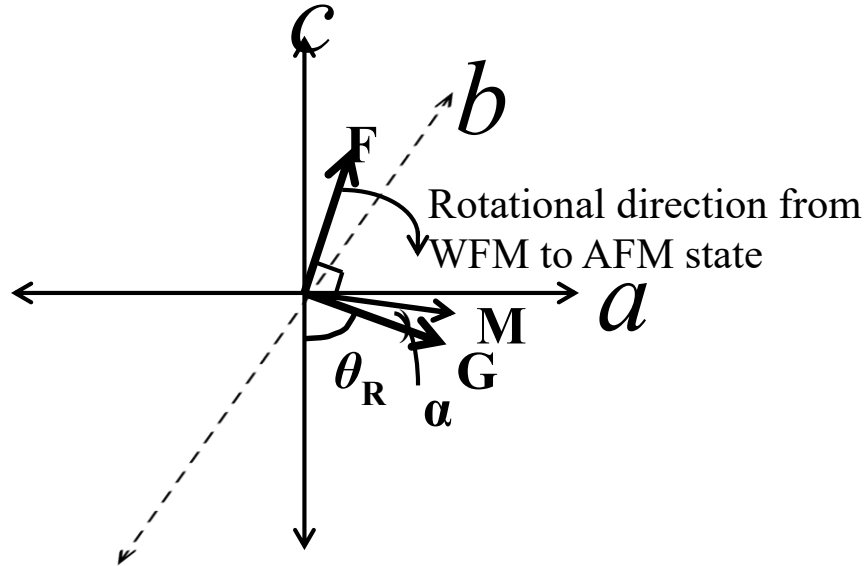


Fig.7. Rotation of magnetic vector during Spin-reorientation

Where, F- Ferromagnetic vector

G- Antiferromagnetic vector

M- Magnetization

α - Canting Angle

θ_R - Angle of rotation of G in 'ac' plane

Until and unless the presence of magneto crystalline-anisotropy gets affected the ground state Γ_4 remains the same. This is due to the presence of high magnetic anisotropy of rare earth which stimulates the phenomena like negative magnetization, spin re-orientation;

magnetic compensation or we can say in a broad way that anomalous behavior of the RCrO_3 compound [39, 40]. At the temperature to its lowest, the magnetic moment of Cr^{3+} dominant R^{3+} , so it is quite hard to know about the magnetic anisotropy of rare earth [41, 42]. The anisotropy of paramagnetic Eu^{3+} is expected to be minimal in EuCrO_3 due to the population of non-magnetic ground term ${}^7\text{F}_0$ of Eu^{3+} . So Γ_2 (F_x , C_y , G_z) configuration may arise because due to the above statement which may lead to the dominant magnetic behavior of Cr^{3+} at low temperatures [43–45]. SmCrO_3 compound also follows the same trend so they are termed to show similar properties. If we talk about the ErCrO_3 the presence of strong magnetic anisotropy of rare earth may lead to collinear Γ_1 (A_x , G_y , C_z) spin structure.

The spin Hamiltonian of RCrO_3 where R is magnetic, the following equations would lead to an appropriate understanding to the spin structure. The spin Hamiltonian varies with different phase such as Γ_1 , Γ_2 and Γ_4 . We are going to denote the Γ_1 phase as α , Γ_2 as β and Γ_4 as γ . In Γ_4 phase the spin Hamiltonian is given below [46].

$$H_\alpha = H_\alpha^{\text{Cr}-\text{Cr}} + H_\alpha^{\text{R}-\text{R}} + H_\alpha^{\text{Cr}-\text{R}} \quad \dots (6)$$

The above equation is the Hamiltonian of RCrO_3 for Γ_4 phase between the $\text{Cr}^{3+}-\text{Cr}^{3+}$ interactions, $\text{R}^{3+}-\text{R}^{3+}$ interactions and $\text{Cr}^{3+}-\text{R}^{3+}$ interactions. Considering the first term for orthorhombic crystallographic we are introducing x , y and z coordinates system. In Γ_4 phase usually spins lies in the coordinate of x axis. The appropriate Hamiltonian for the first term which is between $\text{Cr}^{3+}-\text{Cr}^{3+}$ which is given in equation 7.

Where S_1 and S_2 are representing Cr^{3+} spins in the plus and minus sublattices respectively

—

$$H_a^{Cr-Cr} = \left(\frac{1}{2} N g_c \mu_B \right)^2 - \lambda (S_{1x} S_{2x} + S_{1z} S_{2z}) + D (S_{1x} S_{2z} - S_{1z} S_{2x}) + \frac{1}{2} K (S_{1x}^2 + S_{2x}^2) - \frac{1}{2} g_c \mu_B N H_c (S_{1z} + S_{2z}) \quad \dots (7)$$

g_c is the Z-axis g factor ,

μ_B is the Bohr magnetron

N is Avogadro's number.

The first term of the equation represents the symmetric which is caused by Heisenberg exchange interaction, the second term denotes the antisymmetric which caused due to Dzyaloshinskii-Moriya exchange interaction, the third term denotes the uniaxial anisotropy which fixes the crystallographic axis as the easy direction for each sublattice and the last one represents the coupling of the spins to external fields H_c applied along the z axis. The coefficients λ , D and K are interaction constants.

Going to the second term of equation 6

$$H_a^{R-R} = \left(\frac{1}{2} N g_z \mu_B \right)^2 \left(\frac{1}{2} G_1 \sum_i J_{iz}^2 + G_2 (J_{1z} J_{2z} + J_{3z} J_{4z}) + G_3 (J_{2z} J_{4z} + J_{1z} J_{3z}) + G_4 (J_{2z} J_{3z} + J_{1z} J_{4z}) \right) - \frac{1}{4} g_z \mu_B N H_c - \quad \dots (8)$$

Where J_{iz} is the z component of the effective spin operator at site i and the summation is over the rare earth sites per unit cell.

G_i is the coupling of coefficients

g_z is the z axis effective splitting factor of the rare earth ground doublet

And finally the third term which is between the chromium and rare earth

$$H_a^{Cr-R} = -\left(\frac{1}{4}N\mu_B\right)^2 g_c g_z \sum_i J_{iz} [D_1(S_{1z}+S_{2z}) + D_2(S_{1z}-S_{2z})] \quad \dots (9)$$

Where D_1 and D_2 are coupling coefficients denoting the magnitudes of the symmetric and antisymmetric parts of the Cr-R interaction respectively

The spin Hamiltonian for Γ_1 phase are given below

$$H_\beta = H_\beta^{Cr-Cr} + H_\beta^{R-R} + H_\beta^{Cr-R} \quad \dots (10)$$

The Γ_1 phase is somewhat similar as Γ_4 and the interaction between Cr-Cr in the absence of an external magnetic field is given by-

$$H_\beta^{Cr-Cr} = \left(\frac{1}{2}N g_b \mu_B\right)^2 \lambda S_{1y} S_{2y} \quad \dots (11)$$

$$H_\beta^{R-R} = \left(\frac{1}{2}N g_z \mu_B\right)^2 \left(\frac{1}{2} G_1 \sum_i J_{iz}^2 + G_2 (J_{1z} J_{2z} + J_{3z} J_{4z}) + G_3 (J_{2z} J_{4z} + J_{1z} J_{3z}) + G_4 (J_{2z} J_{3z} + J_{1z} J_{4z}) \right) - \frac{1}{4} g_z \mu_B N H_c \sum_i J_{iz} \quad \dots (12)$$

The last interaction of Γ_1 phase is between the Chromium and Rare earth (Cr – R) and it is given by

$$H_\beta^{Cr-R} = \left(\frac{1}{4}N\mu_B\right)^2 g_b g_z D_3 (J_{1z} + J_{2z} - J_{3z} - J_{4z}) (S_{1y} - S_{2y}) \quad \dots (13)$$

This property of RCrO_3 attracts many researchers to study the complex magnetic behavior of the compound with the fusion of rare earth and transition metal ions. As in our discussion we have evince the interactions and properties of RCrO_3 in terms of their

magnetic behavior. And from this we have known that an extensive range of the temperature has been dominated by the transition metal ion which is chromium in our work. So, we have not collected enough information for the rare earth ions due to the +3 state of the chromium and it is magnetically favorable than R^{3+} ions in $RCrO_3$ compound. Here we report on the study based on different oxidation state of Chromium by varying the annealing temperature from 973 K ($RCrO_3$) to 773 K resulting to form chromates ($RCrO_4$), because in chromates the chromium oxidation state is +5. So, in $RCrO_4$ the observed behavior is mostly from the R^{3+} ion which is more magnetic in nature than Cr^{5+} . It is due to the fact that the Cr^{5+} ion does not have a d-orbital shell. The functionality of the rare earths should be given emphasized because in $RCrO_3$ the anisotropy of the magnetic rare earth plays a major role in deciding the Cr spin structure which is responsible for the intriguing phenomena of spin-reorientation, magnetic compensation and magnetization reversal. So this situation compels us to roll our eyes to study about $RCrO_4$ compound to know the properties of Rare earth also including the chromium. $RCrO_4$ is also one of the family of the research field given by the result of the fusion of rare earth and the transition metal ions, where rare earths (Er, Dy, Gd, Eu and Sm) and transition metal ions (chromium) in this work.

1.7 Rare earth Chromates, $RCrO_4$

Given below in table 8, we have listed some compounds of rare earth chromates ($RCrO_4$) with their Néel temperature where the properties changes. Further-more, the literature reveals the distortion of rare earth chromates into perovskite with a tetragonal structure with space groups $I41/amd$ with crystal symmetry (D_{4h}^{19}) for zircon type material [47, 48]. The final structure which has been assemble up by the edges sharing chains of distorted

(RO₈) bisdisphenoids managing parallel to the a-axis and which is connected one another by the tetrahedral (CrO₄) is given in figure no. 8.

Table 8: RCrO₄ (R=Rare earth, Y and La) compounds with the respective Curie/ Néel temperatures [49–57].

RCrO₄	Ce	Pr	Nd	Pm	Sm	Eu	Gd	Tb
T_C/ T_N (K)	—	9	25	—	15	16	21	22
RCrO₄	Dy	Ho	Er	Tm	Yb	Lu	Y	La
T_C/ T_N (K)	23	18	15	18	25	10	9	20

In rare earth chromates the oxidation state of rare earth is +3 which is same as in rare- earth orthochromites.

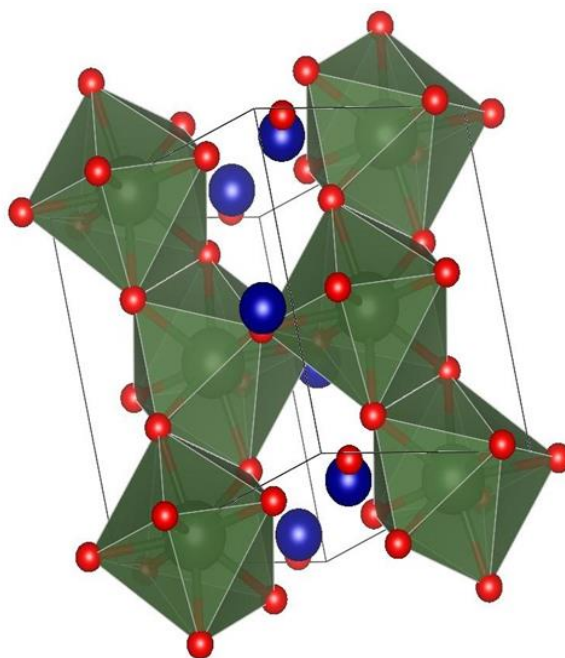
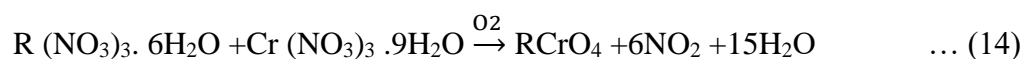


Fig. 8. Polyhedral view of crystal structure of zircon type RCrO₄

But the oxidation state of chromium changes from +3 state to +5 pentavalent state which have a weaker magnetic properties than that in +3 state. The common reaction that takes place in this compound between rare earth and transition metal ions is given in equation (14) below



The phases of rare earth and chromium are inter-convertible into one another at suitable pressure or temperature conditions. The position that occupied by rare earth with an electronic configuration of $(4f^{1-14})$ is in eighth coordinated RO_8 dodecahedra while the chromium ion with an electronic configuration of $(4s^1 3d^0)$ is occupied in distorted CrO_4 tetrahedral. In addition, at high temperatures the chromate undergoes a structural rearrangement and reduces to orthochromites [48]. It is shown in literature that the chromium exists in Cr^{+5} state in the $RCrO_4$ compound which is sequenced by itself ferromagnetically with curie temperature, $T_C \sim 10$ K when the rare earth is non-magnetic [58]. But the rare earth samples discussed in this doctoral thesis work are all magnetic ($R = Er, Dy, Gd, Eu$ and Sm), so at a Néel temperature which is at around $T_N < 20$ K, it changes the spin order of the material or we can say that the magnetic properties changes from paramagnetic to antiferromagnetic state. The two possibilities of the nature of the material are either ferromagnetic or antiferromagnetic and are dependent on the anisotropy of the rare earth (R). The best example from the literature about the magnetic structure of $RCrO_4$ with ($R = Sm, Eu$ and Lu) are shown to be an antiferromagnetic and with $R (Nd-Yb)$ is reported as ferromagnetic in nature [49, 50]. For both $RCrO_3$ and $RCrO_4$ the involvement of rare earth can be seen at very low temperature, so very easily it can be say that the transition occurs at $RCrO_3$ sample is due to the $Cr^{3+} - Cr^{3+}$ interaction. But in case of $RCrO_4$

the transition temperature is very low comparing to the RCrO_3 . So it is quite difficult to point out the interaction responsible for the transition occurred. One more interesting phenomena based on this study is a field induced metamagnetism which we get when we compare the antiferromagnetic and ferromagnetic exchange interaction. And this metamagnetism, where both the Néel temperature and Curie temperature coexists is due to the tough competition between the antiferromagnetic 4f spins of rare earth (R^{3+}) ions and the super-exchange interactions of ferromagnetic 3d spins of chromium (Cr^{3+}) ions [51]. Indeed, RCrO_4 material is one of the interesting and attractive compounds which require an attention to study thoroughly.

1.8 Aim and Scope of the Thesis

From the assessment of the literature described in the previous sections, it is understood that rare earth orthochromites, RCrO_3 (R = rare earth, Y and La) is a class of materials that exhibit unusual magnetic properties [52–56]. They crystallize into orthorhombic perovskite structure with space group $Pbnm$ and D_{4h}^{19} crystal symmetry. The rare earth ion, R^{3+} ($4f^{1-14}$) is located in a nine-coordinated A-site while the chromium ion, Cr^{3+} ($4s^0 3d^3$) in octahedral B-site, similar to the iso-structural orthoferrites, RFeO_3 . They undergo a paramagnetic (PM) to canted antiferromagnetic (CAFM) transition below room temperature with G-type ordered configurations. When R is non-magnetic, the magnetic property is solely an outcome of the super exchange interaction between Cr^{3+} – Cr^{3+} mediated by oxygen with canting of spins at Cr sites below Néel temperature, T_N^1 as reported in YCrO_3 [36,37]. This is attributed to antisymmetric Dzyaloshinskii-Moriya (DM) exchange interaction between neighboring spins that results in $\Gamma_4(\text{G}_x, \text{A}_y, \text{F}_z)$ configuration of Cr spins. However, the ground state configuration, Γ_4 remains the same

unless affected by the presence of magneto-crystalline anisotropy. When R is magnetic, magnetic interactions does exist between $R^{3+}-R^{3+}$ and $R^{3+}-Cr^{3+}$ in addition to $Cr^{3+}-Cr^{3+}$ interaction with possible antiferromagnetic ordering of R^{3+} ions at very low temperature, referred as $T_N^2 < 20K$ [39,40]. In addition, the presence of a magnetic R^{3+} ion (in place of non-magnetic Y^{3+}) brings in magnetic anisotropy that promotes intriguing phenomena like negative magnetization, magnetic compensation and spin-reorientation (SR) in $RCrO_3$ [44,45]. This $3d-4f$ interaction gives rise to the Γ_4 (G_x, A_y, F_z), Γ_2 (F_x, C_y, G_z) and Γ_1 (A_x, G_y, C_z) arrangements in $RCrO_3$ with the Γ_1 being the collinear antiferromagnetic ground state configuration [41,42]. Since the magnetic behavior of $RCrO_3$ is dominated by the $3d$ electrons of Cr, very limited is known about the rare earth ordering in oxides. This necessitates to study rare earth chromates, $RCrO_4$ which crystallizes into tetragonal structure with space groups $I41/amd$ (No. 141, $Z=4$ with crystal symmetry D_{4h}^{19}) and/or $I41/a$ (No. 88, $Z=4$ with crystal symmetry C_{4h}^6) referred as zircon and scheelite phases respectively [47,48]. The two phases are inter-convertible into one another at appropriate temperature and/or pressure conditions. The rare earth ion, R^{3+} ($4f^{1-14}$) is located in an eight-coordinated RO_8 triangular dodecahedra while the chromium ion, Cr^{5+} ($4s^1 3d^0$) in distorted CrO_4 tetrahedra. In $RCrO_4$, Cr exists in paramagnetic Cr^{5+} state that orders ferromagnetically with Curie temperature, $T_C \sim 10$ K in the presence of non-magnetic rare earth, as shown in $YCrO_4$ [57]. When R is magnetic, rare earth orders antiferromagnetically with $T_N < 20$ K. Depending on the anisotropy of the R, the ground state of $RCrO_4$ is either ferromagnetic or antiferromagnetic. It has been reported that the magnetic structure of $RCrO_4$ with $R = Nd-Yb$ is described as ferromagnetic and $R = Sm, Eu$ and Lu are shown to be antiferromagnetic [58, 59]. When the ferromagnetic and antiferromagnetic exchange

interactions are comparable, a field-induced metamagnetism is observed in RCrO_4 with $\text{R} = \text{Ho, Gd and Lu}$. This is due to the strong competition between the super-exchange interactions of ferromagnetic $3d$ spins of Cr^{5+} ions and antiferromagnetic $4f$ spins R^{3+} ions [51]. Thus, the complicated magnetic structure of RCrO_4 and RCrO_3 requires an attention to study. In addition, rare earth chromates and orthochromites have been synthesized by various techniques. However, synthesis of RCrO_4 and RCrO_3 in nanoparticles has been given less attention to the best of our knowledge. In addition, the chromates undergo a structural rearrangement and reduce to orthochromites at high temperatures, reported elsewhere [48].

In view of the above discussion, the present doctoral thesis has been aimed at the following objectives in the forth coming chapters.

1. To synthesis of homogeneous single phase RCrO_4 and RCrO_3 ($\text{R} = \text{Sm, Eu, Gd, Dy and Er}$) through a modified sol-gel route followed by hydrothermal method and temperature driven tuning of the crystal structure of RCrO_4 and RCrO_3 nanoparticles.
2. To study the magnetic properties of temperature induced magnetic phases RCrO_4 and RCrO_3 ($\text{R} = \text{Sm, Gd, Dy and Er}$) and size effects on the magnetic properties through DC magnetization measurements.
3. To study the role played by the magnetic anisotropy of rare earth that brings in a temperature-dependent $3d-4f$ interaction and is responsible for the intriguing magnetic phenomena in RCrO_3 ($\text{R} = \text{Eu, Gd and Er}$) through temperature-dependent electron paramagnetic resonance (EPR) spectroscopy.

References

1. D. Khomskii, *classifying multiferroics: mechanisms and effects*, Physics 2, **20** (2009).
2. N.A. Spaldin, S.-W. Cheong, and R. Ramesh, *multiferroics: past, present, and future*, Phys Today, **63**, p38 (2010).
3. N.A. Hill, *Why Are There so Few Magnetic Ferroelectrics?*, J. Phys. Chem. B, **104**, p6694 (2000).
4. C.N.R. Rao and C.R. Serrao, *New routes to multiferroics*, J. Mater. Chem., **17**, p4931 (2007).
5. N.A. Spaldin and M. Fiebig, *The renaissance of magnetoelectric multiferroics*, Science, **309**, p391 (2005).
6. R. Ramesh, *Materials science: Emerging routes to multiferroics*, NATURE, **461**, p1218 (2009).
7. C.N.R. Rao, A. Sundaresan, and R.Saha, *Multiferroic and Magnetoelectric Oxides: The Emerging Scenario*, J. Phys. Chem. Lett., **3**, p2237 (2012).
8. C.M.N. Kumar, *Crystal and spin structure and their relation to physical properties in some geometrical and spin spiral multiferroics*, Forschungszentrum Jülich GmbH, **44**, p4 (2012).
9. J.V.D. Brink and D.I Khomskii, *Multiferroicity due to charge ordering*, J. Phys. Condens. Matter, **20**, p434217 (2008).
10. D.I.Khomskii, *Multiferroics: Different ways to combine magnetism and ferroelectricity*, JMMM, **306**, p1 (2006).
11. G.Catalan and J.F. Scott, *Physics and Applications of Bismuth Ferrite*, Adv. Mater., **21**, p2463 (2009).

12. J. Moodera, G.X. Miao, and T. Santos, *Frontiers in spin-polarized tunneling*, Phys Today, **63**, p46 (2010).
13. Y. Tokura, *Multiferroics-toward strong coupling between magnetization and polarization in a solid*, J.Magn. Magn. Mate., **310**, p1145 (2007).
14. J. Hu, *Microscopic Origin of Magnetoelectric Coupling in Noncollinear Multiferroics*, Phys. Rev. Lett. , **100**, p077202 (2008).
15. A.L., H.V, Loehneysen, G.M. Kalvius, *PREFACE: Multiferroics Multiferroics*, J. Phys.: Condens. Matter, **20**, p430301 (2008).
16. P. Jain,V. Ramachandran, Ro. J. Clark, H. D. Zhou, B. H. Toby, N. S. Dalal, H. W. Kroto, and A. K. Cheetham, *Multiferroic Behavior Associated with an Order-Disorder Hydrogen Bonding Transition in Metal-Organic Frameworks (MOFs) with the Perovskite ABX₃ Architecture*, J. Am. Chem. Soc., **131**, p13625 (2009).
17. V. Zepf, *Rare earth elements*, Springer-Theses, p65 (2013).
18. A. Walters, and P. Lusty, *Rare earth elements*, British geological survey, p45 (2011).
19. S.H.P. Liu, *Magnetic properties of rare earth metals*, Retrospective Theses and Dissertations, p2796 (1960).
20. L. Pauling, *College Chemistry: An Introductory Textbook of General Chemistry*, W. H. Freeman and Company, p518 (1950).
21. K. Sardar, Martin R. Lees, R. J. Kashtiban, J. S. and R. I. Walton, *Direct Hydrothermal Synthesis and Physical Properties of Rare earth and Yttrium Orthochromite Perovskites*, Chem. Mater., **23**, p48 (2011).

22. J.P. Gonjal, R. Schmidt, D. Avila, U. Amador, E. Moran, *Structural and physical properties of microwave synthesized orthorhombic perovskite erbium chromite ErCrO_3* , J. Eur. Ceram. Soc, **32**, p611 (2012).
23. B. Rajeswaran, D. I. Khomskii, A. K. Zvezdin, C.N.R. Rao and A. Sundaresan, *Field-induced polar order at the Néel temperature of chromium in rare earth orthochromites: Interplay of rare earth and Cr magnetism*, Phys.Rev.B, **86**, p214409 (2012).
24. O. Borang, S. Srinath, S. N. Kaul, Y. Sundarayya, *Temperature driven tuning of the structure and magnetic properties of oxides of erbium and chromium at nanoscale*, IJRET, **06**, p14 (2017).
25. S. Kumar, I. Coondoo, M. Vasundhara, S. Kumar, A. L. Kholkin, and N. Panwar, *Structural, Magnetic, Magnetocaloric and Specific heat Investigations on Mn doped PrCrO_3 Orthochromites*, J. Phys.: Condens. Matter, **29**, p195802 (2017).
26. J.-S. Zhou, J. A. Alonso, V. Pomjakushin, J. B. Goodenough, Y. Ren, J.-Q. Yan and J.-G. Cheng, *Intrinsic structural distortion and superexchange interaction in the orthorhombic rare earth perovskites RCrO_3* , Phys.Rev.B, **81**, p214115 (2010).
27. L.H. Yin, J. Yang, P. Tong, X. Luo, C.B. Park, K.W. Shin, W.H. Song, J.M. Dai, K.H. Kim, X.B. Zhu, and Y.P. Sun, *Role of rare earth in the magnetic, magnetocaloric and magnetoelectric properties of RCrO_3 ($R=\text{Dy, Nd, Tb, Er}$) crystals*, J. Mater. Chem. C, **4**, p47 (2016).
28. V.S. Bhadram, D. Swain, R Dhanya, M. Polentarutti, A Sundaresan and C. Narayana, *Effect of pressure on octahedral distortions in RCrO_3 ($R= \text{Lu, Tb, Gd, Eu, Sm}$): the role of R-ion size and its implications*, Mater Res Express, **1** , p026111 (2014).

29. A. McDannald, L. Kuna, M.S. Seehra, and M. Jain, *Magnetic exchange interactions of rare earth-substituted $DyCrO_3$ bulk powders*, Phys.Rev.B, **91**, p224415 (2015).
30. Y. Sundarayya, P. Mandal, A. Sundaresan and C. N. R. Rao, *Mössbauer spectroscopic study of spin reorientation in Mn-substituted yttrium orthoferrite*, J. Phys. Condens. Matt., **23**, p436001 (2011).
31. S. Mathur, M. Veith, R. Rapalaviciute, H. Shen, G. F. Goya, W. L. M. Filho and T. S. Berquo, *Molecule Derived Synthesis of Nanocrystalline $YFeO_3$ and Investigations on Its Weak Ferromagnetic Behaviour*, Chem. Mater., **16**, p1906 (2004).
32. R.M Hornreich and S.Shtrikman, *Magnetization studies in rare earth orthochromites. VII. $LuCrO_3$* , Phys.Rev.B, **13**, p9 (1976).
33. K.P. Belov, V.N. Derkachenko, A.M. Kadomtseva, T.L. Ovchinnikova, V.A. Timofeeva and V.A. Khokhlov, *Fiz. Tverd. Tela*, **17**, p3328 (1975).
34. N.Shamir, H.Shaked, Shtrikman, *Magnetic structure of some rare earth orthochromites*, Phys.Rev.B, **24**, p11 (1981).
35. H.J. Zhao, J. Iniguez, X.M. Chen, and L. Bellaiche, *Origin of the magnetization and compensation temperature in rare earth ortho ferrites and orthochromites*, Phys. Rev. B, **93**, p014417 (2016).
36. I. Singh, A. K. Nigam, K. Landfester, R.M. Espi and A. Chandra, *Anamolous magnetic behavior below 10 K in $YCrO_3$ nanoparicles obtained under under droplet confinement*, Appl. Phys. Lett., **103**, p182902 (2013).
37. C.R. Serrao, A.K. Kundu, S.B. Krupanidhi, U.V. Waghmare, and C.N.R. Rao, *Biferroic $YCrO_3$* , Phys. Rev. B (Rapid Comm.), **72**, p220101 (2005).

38. G. Alvarez, H. Montiel, M.P. Cruz, A.C. Duran and R. Zamorano, *Resonant and non-resonant microwave absorption in the magnetoelectric $YCrO_3$ through ferro-paraelectric transition*, J. Alloy Compd., **509**, pL331 (2011).
39. T. Sakata, and A. Enomura, *Studies of the rare earth-iron interactions in the orthoferrites $GdFeO_3$ and $HoFeO_3$* , Phys. Status Solidi A, **52**, p311 (1979).
40. K.B. Aring, and A. J. Sievers, *Role of the Ytterbium Spins in the Spin Reorientation in $YbFeO_3$* , J. Appl. Phys., **41**, p1197 (1970).
41. E. F. Bertaut, in *Magnetism III*, edited by G. T. Rado and H. Suhl, Academic, New York, **3**, p149 (1968).
42. E.F. Bertaut, G. Bassi, G. Buisson, P. Burlet, J. Chappert, A. Delapalme, J. Mareschal, G. Roullet, R. Aleonard, R. Pouthenet, and J. P. Rebouillat, *Some Neutron-Diffraction Investigations at the Nuclear Center of Grenoble*, J. Appl. Phys. **37**, p1038 (1966).
43. A.M. Sánchez, F. Fernández and R.S. Puche, *Magnetic properties of rare earth chromates $RCrO_4$ ($R = Nd, Sm$ and Eu)*, J. Alloy. Comp., **201**, p161 (1993).
44. J.H. Van Vleck, *Theory of Electric and Magnetic Susceptibilities*, Oxford University Press, p86, (1965).
45. A.H. Morrish, *The Physical Principles of Magnetism*, Wiley-IEEE Press, p46, New York (2001).
46. A. Hasson, R.M Hornreich and Y.Komet, *Magneto-optical and magnetization studies in the rare earth orthochromites. IV. $ErCrO_3$* , Phys. Rev. B, **12**, p5051 (1975).
47. E.J. Melero, P.C.M. Gubbens, M.P. Steenvoorden, S. Sakarya, A. Goosens, P. Dalmas de Reotier, A. Yaouanc, J.R. Carvajal, B. Beuneu, J. Isasi, R.S.Puche, U. Zimmerman and J.L.

- Martinez, *A combined studies of the magnetic properties of $GdCrO_4$* , J. Phys.: Condens, Matt., **18**, p7893 (2006).
48. Y. Long, Q. Liu, YuxiLv, R. Yu, C. Jin, *Various 3d-4f spin interactions and field-induced metamagnetism in the Cr^{5+} system $DyCrO_4$* , Phys. Rev. B, **83**, p024416 (2011).
49. H.Walter, H.G. Kahle, K. Mulder, H.C. Schopper, H. Schwarz, *Magnetic phase transitions in rare earth chromates*, Int. J. Magn., **5**, p129 (1973).
50. E. Jiménez, J. Isasi, R. S. Puche, *Synthesis, structural characterization and magnetic properties of $RCrO_4$ oxides*, R= Nd,Sm,Eu and Lu, J. Alloys Comp., **312**, p53 (2000).
51. A. Midya, N. Khan, D. Bhoi and P. Mandal, *3d-4f spin interaction and field-induced metamagnetism in $RCrO_4$ ($R = Ho, Gd, Lu$) compounds*, J. Appl. Phys., **115**, p17E114 (2014)
52. C.Veyret, J. B. Ayasse, J. Chaussy, J. Mareschal, and J. Sivadriere, *Magnetic properties of single crystal $ErCrO_3$* , J. Phys. (France), **31**, p607 (1970).
53. M. Eibschutz, L. Holmes, J. P. Maita, and L. G. Van Uitert, *Low temperature magnetic phase transition in $ErCrO_3$* , Solid State Commun., **8**, p1815 (1970).
54. J.B. Goodenough, *Electronic and ionic transport properties and other physical aspects of perovskites*, Rep. Prog. Phys., **67**, p1915 (2004).
55. T.Yamaguchi, *Theory of spin reorientation in rare earth orthochromites and orthoferrites*, J.Phys.Chem. Solids, **35**, p479 (1974).
56. L.H. Yin, J. Yang, P. Tong, X. Luo, C.B. Park, K.W. Shin, W.H. Song, J.M. Dai, K.H. Kim, X.B. Zhua and Y.P. Sun, *Role of rare earth ions in the magnetic, magnetocaloric and magnetoelectric properties of $RCrO_3$ ($R = Dy, Nd, Tb, Er$) crystals*, J. Mater. Chem. C, **4**, p11198 (2016).

57. Y.W. Long, L.X. Yang, Y. Yu, F.Y. Li, R.C. Yu, and C.Q. Jin, *Synthesis, structure, magnetism and specific heat of $YCrO_4$ and its zircon-to-scheelite phase Transition*, Phys.Rev.B, **75**, p104402 (2007).
58. E. Jiménez, J. Isasi, M.T. Fernández, R.S. Puche, *Magnetic behaviour of $ErCrO_4$ oxide*, J. Alloys Comp., **344**, p369 (2002).
59. R.S. Puche, E. Climent, M.G. Rabie, J. Romero, and J.M. Gallardo, *Neutron diffraction characterization and magnetic properties of the scheelite-type $ErCrO_4$ polymorph*, J. Phys.: Conf. Series, **325**, p012012 (2011).

Chapter 2

Experimental Techniques

2.1 Introduction

In this chapter, the various experimental techniques and working principles of the instruments used in carrying out this research work, has been described in detail. The structural characterization for crystal structure, lattice parameters was performed by X-ray diffractometry (XRD) and the topographical studies (microstructure studies) of the sample were carried out using field emission scanning electron microscopy (FESEM). The elemental compositions of the samples were determined by energy dispersive X-ray analysis (EDAX). The magnetic properties of the as-synthesized RCrO_4 and RCrO_3 have been studied using vibrating sample magnetometer (VSM) setup in physical property measurement system (PPMS). The electron paramagnetic resonance (EPR) spectra were recorded in the X band region of EPR spectrometer to understand the electronic structure and magnetic properties of the sample.

2.2 Sol gel method

The sol gel method is the process in which a molecular precursor in liquid forms an oxide network through poly condensation reaction that cross link with each other to form a gel of solid continuous network as well as liquid continuous network [1]. The precursors for the synthesizing procedure to this kind of colloids are consisting of metal alkoxides and transition metal ions. There are generally two reactions namely hydrolysis and polycondensation that are involved in a sol-gel process. A sol is a colloidal solid particle where

the stable suspension occurs in a liquid of around 2–200 nm. And depending on the solvents it can be obtained in aqueous solution and an alcohol. A gel is a solid network having porous sites which forms in a liquid medium in three dimensions. The growth of gel depends on the container and on a solvent. Sol-gel is basically a process forming a chemical compound in a liquid state at room temperature or at low temperature with a precise control of the purity of the elements. This process also yields the highest specific surface area of a compound relative to any other method. The flexible processing allows combining organic and inorganic compounds.

2.3. Hydrothermal synthesis

A German geologist Karlemil von Schafhautl was the first person to report the growth of crystal by hydrothermal method by using a pressure cooker where he has grew microscopic quartz in 1845 [2]. The hydrothermal technique has become one of the most popular or common way of synthesis due to its ease and flexibility in preparing a wide range of nanomaterial's at low temperatures. Hydrothermal method involves crystallizing/precipitating the compounds at high pressures and low temperatures from aqueous/ non-aqueous solutions relative to conventional high temperature synthesis techniques [3]. The synthesis procedure involves an apparatus, autoclave made up of stainless steel along with a Teflon liner, to which the solution has to be transferred, as shown in figure 1. In between the autoclave chamber the temperature gradient are maintained. Byrappa and Yoshimura proposed to define the hydrothermal reaction as “any heterogeneous chemical reaction in the presence of solvent (whether aqueous or non-aqueous) above room temperature and at pressure greater than one atmosphere in a closed system” [4]. In a typical reaction, a

precursor and a reagent capable of regulating the crystal growth are added into water in a certain ratio.

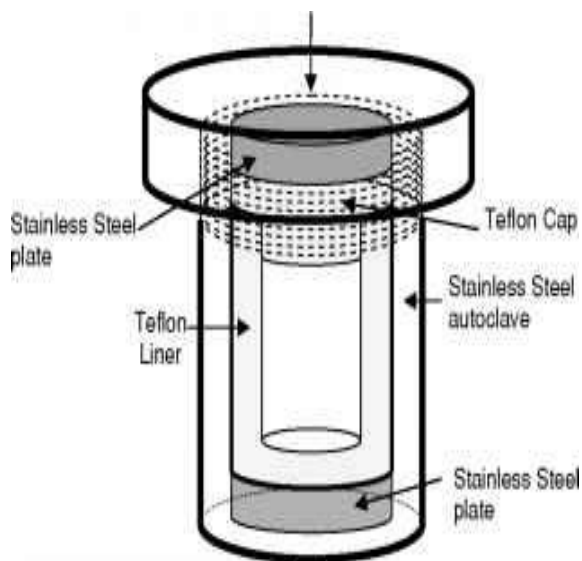


Fig.1. Schematic diagram of the mini-stainless steel auto clave and the Teflon liner.

The mixture is placed in an autoclave to allow the reaction to proceed at elevated temperatures and pressures. The advantage of hydrothermal synthesis is the ability to synthesize crystalline phases that are unstable at melting point. Certain compounds can be synthesis even at temperatures higher than the melting point, at high vapours pressure with a controlled composition. The major advantage of this approach is that most of the inorganic material can be made soluble in water at elevated temperatures and pressures. However, the growth of the crystals and the work performance cannot be observed.

2.4 X-Ray Diffraction

Max Van Laue in 1912 discovered that crystalline substances act as three-dimensional diffraction grating for X-Ray wavelength similar to the spacing of planes in a crystal lattice. Every crystalline substance gives a pattern. The same substance always gives the

same pattern and in a mixture of substances each produces its patterns independently of the others. X-Ray Diffraction is now a common technique for the study of crystal structure details (e.g., average crystallite size and crystallite structure) and Atomic Spacing. X-Ray Diffraction plays a prominent role in Identifying and Characterizing the Nano-crystalline of rare earth and chromium ions Sample.

2.4.1 Principle of X-Ray Powder Diffraction (XRD)

X-Ray Diffraction is based on constructive interference of monochromatic X-rays and a crystalline sample. These X-rays are generated by cathode ray tube, filtered to produce monochromatic radiation, collimated to concentrate, and directed towards the sample. The interaction of the incident rays with the sample produces constructive interference when conditions satisfy “Bragg’s Law”, i.e.

$$2d_{hkl} \sin\theta = n\lambda \quad \dots (1)$$

Where, d_{hkl} – the interplanar spacing between parallel planes.

θ – the Bragg angle

λ – the incident wavelength

and n – the order of diffraction.

This law relates the wavelength of electromagnetic radiation to the diffraction angle and the lattice spacing in a crystalline sample. These diffracted X-rays are then detected, processed and counted. By scanning the sample through a range of 2θ angles, all possible diffraction directions of the lattice should be attained due to the random orientation of the

powdered material. Conversion of the diffraction peaks to d-spacing allows identification of the mineral because each mineral has a set of unique d-spacing. Typically, this is achieved by comparison of d-spacing with standard reference patterns. All diffraction methods are based on generation of X-rays in an X-ray tube. These X-rays are directed at the sample, and the diffracted rays are collected. A key component of all diffraction is the angle between the incident and diffracted rays. Powder and single crystal diffraction vary in instrumentation beyond this.

2.4.2 Working of X-Ray Diffractometer

The basic measurement geometry which is most frequently used X-ray diffraction instrument is depicted in figure 2 [5]. The sample S should preferably exhibit a plane or flattened surface. The angle of both the incoming and the exiting beam is θ with respect to the specimen surface. A vast number of organic and inorganic powder samples have been measured with these instruments from which the naming of powder diffract meter is understood. The diffraction pattern is collected by varying the incidence angle of the incoming X-ray beam by θ and the scattering angle by 2θ while measuring the scattered intensity $I(2\theta)$. Two angles have thus to be varied during a $\theta/2\theta$ scan and various types of powder diffractometers are in use. For one set of instruments the X-ray source remains fixed while the sample is rotated around θ and the detector moves by 2θ . For other systems the sample is fixed while both the X-ray source and the detector rotate by θ simultaneously, but clockwise and anticlockwise, respectively. The rotations are performed by a so-called goniometer, which is the central part of a diffractometer. A goniometer of a powder diffractometer comprises at least two circles or equally two axes of rotation.

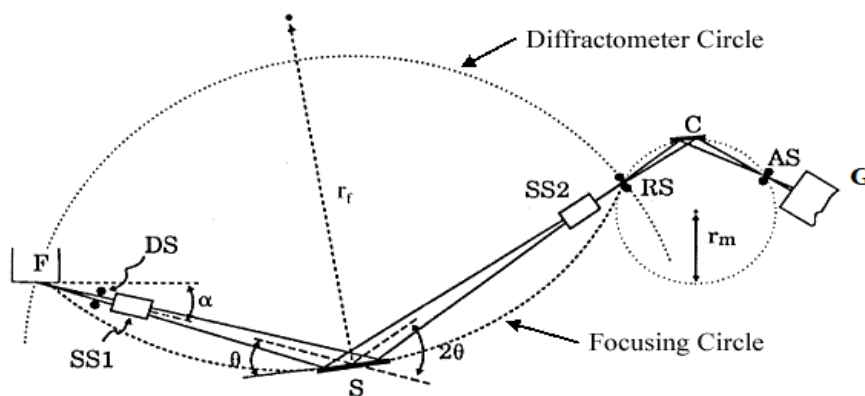


Fig.2. Schematic Diagram of X-Ray Diffractometer

F – The x-ray source

DS – the incident beam divergence limiting slit

SS – The Soller Slit Assembly

S – The Sample

RS – The Diffracted-Beam Receiving Slit

C – The Monochromator Crystal

AS – The Anti-Scattering Slit

R – Axis perpendicular to the plane of drawing

G – Counter.



Fig.3. Bruker D8 Advance diffractometer

However in this work, to study the structural details about the nanocrystalline of rare earth and chromium ions, Bruker D8 Advance diffractometer machine has been used, as shown in figure 3. The Bruker D8 Advance powder X-ray diffractometer is a device for the phase-analytic and structural characterization of powders and thin films. It is equipped with a fast detector and allows measurements in the transmission and reflection mode. The device is additionally equipped with a multi-sample charger. In this diffractometer a scintillation counter may be used as detector instead of film to yield exact intensity data. Using automated goniometers step by step scattered intensity may be measured and stored digitally. The digitized intensity may be discussed by programs. More powerful methods

may be used to determine lots of information about the specimen. The Bruker D8 Advance has a $\theta:\theta$ geometry (often called Bragg-Brentano or focusing geometry) with a copper sealed tube X-ray source producing Cu $k\alpha$ radiation (technically $k\alpha_1$ and $k\alpha_2$ with $k\beta$ being removed by the primary optic) at a wavelength of 1.5406 Å from a generator operating at 40 keV and 40 mA. A parallel beam of monochromatic X-ray radiation is produced by the use of a Göbel mirror optic (primary optic). The diffracted X-rays are recorded on a scintillation counter detector located behind a set of long Soller slits/parallel foils. The sample remains flat throughout the measurement but can be rotated to allow for better sampling and removal of preferred orientation effects.

The average crystallite sizes t can be estimated from FWHM of the respective diffraction peaks by the Scherrer's formula [5],

$$t = \frac{0.94\lambda}{B \cos \theta_B} \quad \dots (2)$$

Where θ_B is the Bragg angle

λ is incident wavelength(nm)

B is Full width at half-maximum (FWHM in radians)

2.5 FESEM and EDAX

The morphology of the samples has been examined by Carl Zeiss ULTRA-55 field emission scanning electron microscope (FESEM). In FESEM, the electrons interlude with the atoms of the sample to produce the result which contain an information about the

composition, topography and also the other components regarding electrical conductivity [6, 7]. While discussing about this, it came across that there are two source of emission, which are Thermionic emitter and Field emitter. And this source of emitter type is the main difference between the scanning electron microscopy and the field emission electron microscopy. The most commonly used filaments in the thermionic emitter is tungsten (W) and lanthanum hexaboride (LaB_6). The electrons can escape after only when the heating is enough above the work function of the heating material. The unwanted problems that we face on thermionic emitter is that it has a relative low brightness with the evaporation on the cathode material side and also has the thermal drifting during the whole operation process. While the good news is that we don't have that kind of problem in the process of field emitter. Because of its unheating process of filament, the field emitter is also known as cold cathode field emitter. So the only way it uses to reaches the emission is to place the filament in a huge electrical potential gradient. The FE source has a sharp point usually with a wire of tungsten (W) with an approximately 100 nm and due to which we can concentrate the electric fields in an extreme level which turns it into so big that the electrons can leave the cathode because of the lowering of the work function. The researcher has find one techniques where the secondary electron can be detected by combining the field emission (FE) and the scanning electron microscopy (SEM). As we already know that the field emission produced an electron beam of about 1000 times smaller than that of a standard microscope which also has a thermal electron gun , hence the quality of an image produced much better for example we can get the resolution of approximately 2 nm at 1 KeV and approx 1 nm at 15 KeV. The feature must be bigger than the beam of diameter in terms to resolve the feature of the specimen surface; therefore the

electrons beam should get condensed. The electromagnetic lenses are engaged to help the demagnetization of the beam. By experiment, it has come to know that in the field emission source the cross over diameter is smaller and for the image processing the probe should be of the lower level of the beam condensation. This nature of field emission scanning electron microscope made it one of the highest resolution instruments comparing other. The important applications of FESEM including the thickness measurement of thin coatings and films, measurement of lateral dimensions and height of nanometer sized objects, elemental analysis of micron sized features, correlation of surface morphology and surface appearance, fracture and failure analysis, characterization of shape and dispersion of additives, size, size distribution, particulates and fibers in composites and blends, characterization of cell size and size distribution in foam materials and defect analysis. Along with this instrument, one more important machine we have used to identify the elemental composition of as little as cubic micron of a material. This instrument is named as energy dispersive X-ray spectroscopy (EDAX or EDX). The sample under the investigation for elemental information is gathered under this equipment which is attached with the scanning electron microscopy. It has sensitivity of around 0.1 percent for some elements and also it is non destructive. In an electron beam a sample has been kept and that is how the EDS work by detecting X-ray. While continuously producing X-rays to discharge the excess energy the electron beam excites the atoms in the sample. The formation of the peaks depends upon the energy of the X-rays which is characteristic of the atoms that produced them. The possibility of having more than one peak is highly in an individual elements and overlapping to a certain degree from the different elements may also occur for the same. While collecting the EDX spectra from a certain particle on the

sample it also gives an analysis of a few cubic microns of material as an electron beam can be controlled precisely. In order to identify the elements in the particular region the beam can easily sweep over a selected area.

2.6 Physical property measurement system (PPMS)

The magnetic properties have been measured by a vibrating sample magnetometer (VSM) in a physical property measurement system (PPMS), designed by Quantum Design, Inc., shown in figure 4. The instrument can be used with fields up to ± 16 tesla and temperature range of 1.9 – 400 K. Its advanced expandable design combines many features in one instrument to make the PPMS the most versatile system of its kind. One can measure DC Resistivity, AC Transport (AC Resistivity, Hall Coefficient, I-V Curve, & Critical Current for superconductors), and Heat Capacity for small samples under user controlled magnetic field, pressure, gas composition, and temperature. The Vibrating sample magnetometer (VSM) is a powerful measurement system to be used for magnetic property of samples. The VSM option transforms your PPMS into a sensitive DC magnetometer for fast data acquisition. The movement of the sample is done by a special sample transport, which has a linear characteristic and thus is very precise and flexible. Further options extend the capability of the VSM.

The Quantum Design Vibrating Sample Magnetometer (VSM) option for the Physical Property Measurement System (PPMS) family of instruments is a fast and sensitive DC magnetometer. The basic measurement is accomplished by oscillating the sample near a detection (pickup) coil and synchronously detecting the voltage induced. By using a

compact gradiometer pickup coil configuration, relatively large oscillation amplitude (1-3 mm peak) and a frequency of 40 Hz, the system is able to resolve magnetization changes of less than 10^{-6} emu at a data rate of 1 Hz. The VSM option consists primarily of a VSM linear motor transport (head) for vibrating the sample, a coil set puck for detection, electronics for driving the linear motor transport and detecting the response from the pickup coils, and a copy of the software application for automation and control.



Fig.4. Physical property measurement system

2.6.1 Theory of Operation

The basic principle of operation for a vibrating sample magnetometer is that a changing magnetic flux will induce a voltage in a pickup coil [8]. The time-dependent induced voltage is given by the following equation:

$$V_{coil} = \frac{d\Phi}{dt} \quad \dots (3)$$

$$= \frac{d\Phi}{dz} \frac{dz}{dt}$$

$$V_{coil} = 2\pi f C_m A \sin(2\pi f t) \quad \dots (4)$$

The basic measurement is accomplished by oscillating the sample near a detection (pickup) coil and synchronously detecting the voltage induced. In equation (3), Φ is the magnetic flux enclosed by the pickup coil; z is the vertical position of the sample with respect to the coil, and t is time. For a sinusoidally oscillating sample position, the voltage is based on the following equation: In equation (4), C is a coupling constant, m is the DC magnetic moment of the sample, A is the amplitude of oscillation, and f is the frequency of oscillation. The acquisition of magnetic moment measurements involves measuring the coefficient of the sinusoidal voltage response from the detection coil. The sample is attached to the end of a sample rod that is driven sinusoidally. The center of oscillation is positioned at the vertical center of a gradiometer pickup coil. The precise position and amplitude of oscillation is controlled from the VSM motor module using an optical linear encoder signal. The voltage induced in the pickup coil is amplified and lock-in detected in the VSM detection module. The VSM detection module uses the position encoder signal as a reference for the synchronous detection. This encoder signal is obtained from the VSM motor module, which interprets the raw encoder signals from the VSM linear motor transport. The VSM detection module detects the in-phase and quadrature-phase signals from the encoder and from the amplified voltage from the pickup coil. These signals are averaged and sent over the CAN bus to the VSM application running on the PC.

2.7 Electron Paramagnetic Resonance (EPR) Spectrometer

All the species which have magnetic moment associated with an electron can be studied by this technique. Some atoms and molecules consists one or more electrons with unpaired spins and these are the substances which are expected to show electron spin resonance spectra because the magnetic field interacts with the spin and the spin of the system has to be non-zero. This type of spectroscopy is also known as electron paramagnetic resonance (EPR). Many can understand all kind of properties (e.g. electronic structure, magnetism, photochemistry and biology) from this spectrometer. Majority of stable molecules are held together by bonds in which electron spins are paired, in this situation there is no net electron spin, no electronic magnetic moment and hence no interaction between the electron spins and an applied magnetic field. When unpaired electrons exist in a substance their spins are aligned at random in the absence of a field. When placed in a magnetic field, however they will each have a preferred direction and since the spin quantum numbers of an electron is $1/2$ each can be thought of a spinning either clockwise or anti-clockwise about the field direction. E.S.R spectroscopy essentially measures the energy required to reverse the spin of an unpaired electron. Numerical simulations of EPR spectra are usually performed with three intentions-

1. Systematic study of the dependencies of spectral feature on the magnetic parameters.
2. Predictions whether a new experiment will give new information and
3. Accurate parameter extraction from experimental spectra.

2.7.1 Principle of ESR

Electrons are known to have magnetic moments and when they are exposed in a magnetic field, we can do a spectroscopic measurement on it. Electrons has an intrinsic angular momentum which is also called as electron spin angular momentum and that explains a lots of experiment observation on species for examples are atoms, molecules, free radicals, radicals ions, transition metal complexes. So we know that an electron can have two type of angular momentum-

1. Orbital angular momentum, $l = 0, 1, 2, \dots m_l = -l, -l+1, \dots l-1, l$.
2. Spin angular momentum, $S = 1/2, m_s = -1/2, +1/2$

So spin angular momentum is a vector quantity i.e. it has a particular direction whether its upside or down side and an orbital angular momentum is also a vector quantity which has a different components with a certain direction. So the two angular momentum can now be putting up together to generate a net angular momentum. Since an electron has two specific components of the angular momentum as we have already discussed it should also have two orientations of the magnetic moment in the magnetic field. So we have also a fact by which we can easily explain the splitting of atomic spectral line in the magnetic field which is a famous Zeeman Effect. So with this basic we will be explaining the experimental result of our sample. We already know that electrons have an intrinsic magnetic moment which acts properly like a tiny bar magnets which has also a magnetic moment.



Fig.5. Bar magnet

μ – Magnetic moment vector

$$\mu_z = g_e \beta_e S_z \quad \dots (5)$$

As given in the bar magnet, it has a magnetic moment μ which has a direction from south to north and also it is a vector quantity. So from here it can be easily related the magnetic moment and the angular momentum by the equation (5) which is given above.

μ_z – magnetic moment vector in the given direction

g_e – constant, g-factor

β_e – Bohr magneton

S_z – component of spin angular momentum

Further we will be discussing about what happens when a bar magnet is placed in a magnetic field and the consequences when these two has encountered with each other. So basically we have a bar magnet which has a magnetic moment μ and has been placed in a magnetic field B . The expression has been given in equation 6. Then the magnetic moment will orient itself according to the value of an angular momentum. It has depicted in figure 6.

$$E = - \mu \mathbf{B} \text{ (both vector)} \quad \dots (6)$$

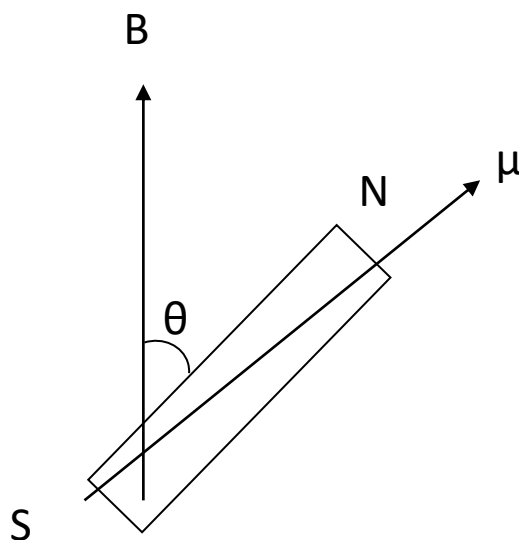


Fig. 6. Bar magnet in a magnetic field

Electron spin has two energy levels when kept in a magnetic field, also known as Zeeman splitting. The diagram has been given below in figure 7 by which the splitting of an energy level will be clear enough to understand.

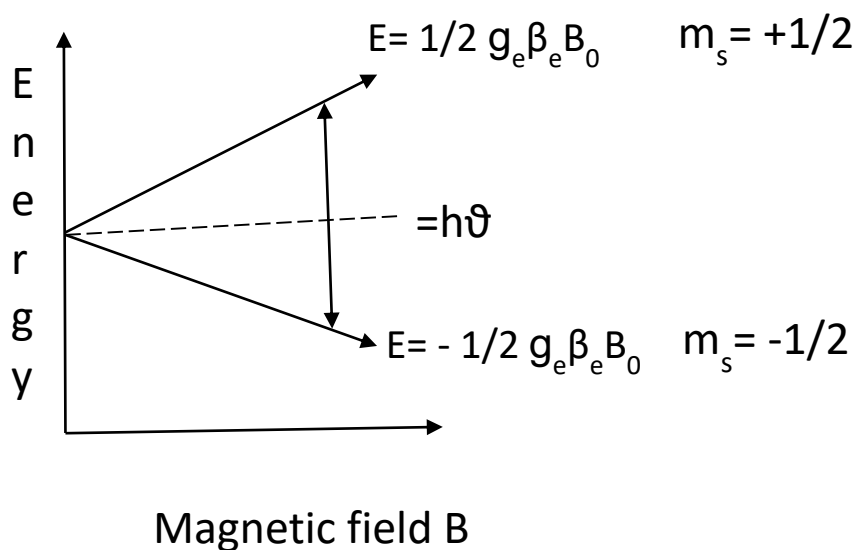


Fig.7. Zeeman splitting

The splitting of the energy level is fully depend upon the strength of the magnetic field, suppose if the magnetic field is small then the splitting will be small but if the magnetic field is large then the splitting level will be large. From the literature, we also know the value of Bohr magneton which is given in the below equation [9 – 11]

$$\beta_e \text{ (bohr magnetron)} = eh/ 4\pi me \quad \dots(8)$$

$$E= g_e\beta_e B_0 \quad \dots (9)$$

$$E= h\nu \quad \dots (10)$$

From equation 9 and 10

$$h\nu= g_e\beta_e B_0 \quad \dots (11)$$

$$h\nu= \mu B_0 \quad \dots (12)$$

The energy difference between the first energy level and the second energy level is μB_0 which falls on the radiation of microwave frequency which is at the range of $10^8 - 10^{11}$ Hz.

2.7.2 Working techniques and components of EPR spectrometer

In this topic we are going to discuss about the working principle of electron resonanace frequency spectrometer and how the principle of ESR spectrometer takes place practically. Figure 8 shows the block diagram of the ESR spectrometer, consisting of source, actuators, waveguide, detector, phase sensitive detector, modulation coil, sample cavity and electromagnets.

Source: Here, source is represented as a klystron tube which act as a source of radiation i.e. microwave radiation. The radiation is simplified after producing typically from the klystron tube which is also having an ability to tune the waves to precise phase amplitude and frequency. The radiation coming out from this has been again allowed to falls into the resonant cavity by using either coaxial cable or wave guide. Wave guide is considering as one of the most efficient method.

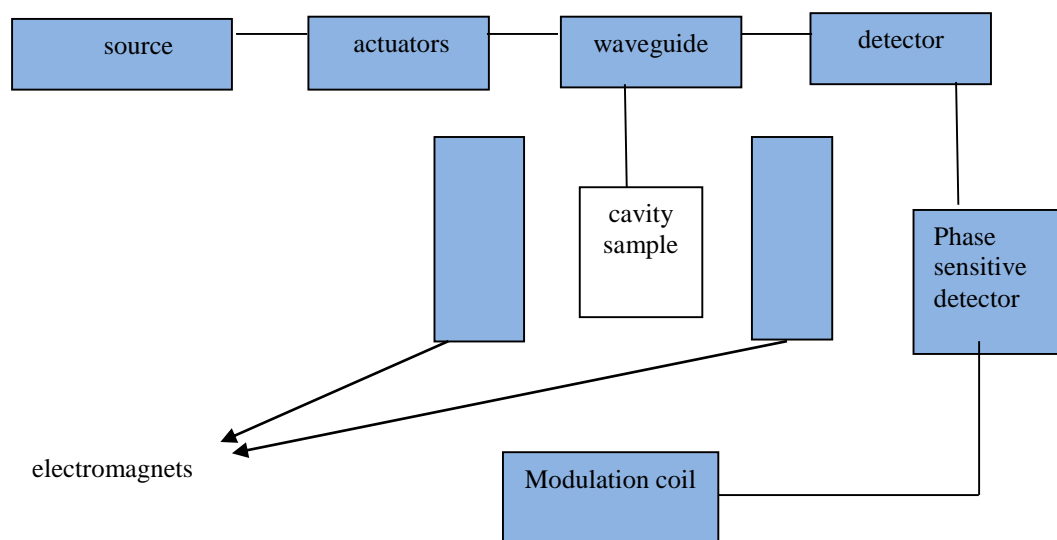


Fig.8. Block diagram of ESR spectrometer

Now we will be continuing with how the electromagnetic radiation and microwave frequencies are generated in a klystron tube. In figure 9 the schematic diagram of a klystron tube has been shown.

As we can see in the schematic diagram of a klystron tube there are three electrodes which are –

1. Heated filament

2. Anode
3. Negative reflector

Here, cathodes generate an electron from a heated filament which flows through an anode which has a hole and after which it strikes on a highly negative reflector electrode which has a negative charge. An electron has also a negative charge which causes repulsion between each other, so the electrons have been sent back to the anode from the negative reflector due to its negativity. So the motion of electron charge from anode to negative reflector and again back to the anode from hole cause an oscillating electric field so thus electromagnetic field.

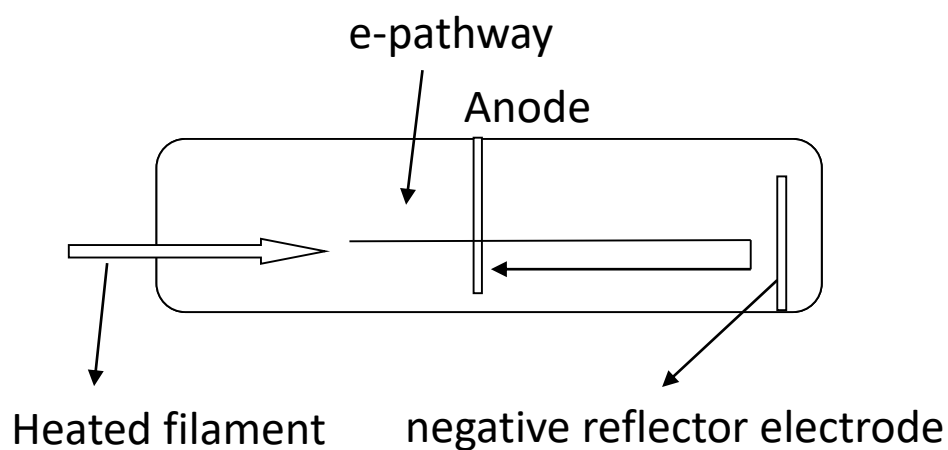


Fig.9. Klystron tube

Attenuator: Attenuator is used to adjust the microwave power sent by the source.

Waveguide: It is a rectangular brass tube having an approximate size of 0.99x0.4 inch. It is used to convey the microwave radiation or power to the sample cavity containing paramagnetic substances.

Sample cavity: Mostly sample cavity is placed between the two electromagnets and it is constructed in such a way to maximize the applied magnetic field along the sample direction. Generally, all the ESR spectrometer has dual cavity to accommodate the sample as well as to accommodate the standard material.

Electromagnets: In ESR two electromagnets are used i.e. North Pole and South Pole. ESR spectrum is recorded by slowly varying the magnetic field through the resonance condition by sweeping the current supplied to magnet by power supply. The role of electromagnets is to generate the homogeneous magnetic field and the current supply to the magnets through the power supply due to this, alternating current generates a heat therefore both the power supply and the magnet need a water cooling apparatus.

Modulation coils: The variation of magnetic field is produced by supplying an alternating current signal to modulation coils oriented with respect to samples. If the modulation is of low frequency then, coils can be mounted outside the sample cavity. If the modulation is of high frequency, the frequency coils can be mounted inside the cavity.

Crystal detector: The most common detector is the silicon crystal detector which acts as a microwave rectifier. The silicon crystal detector converts the alternating current to direct current outputs.

2.7.3 Low Temperature EPR Measurements

Temperature-dependent electron paramagnetic resonance (EPR) spectra were recorded in the X-band region on JEOL-FE3X ESR spectrometer in the range 100 – 400 K, using a liquid nitrogen (LN2) cryostat, at a fixed microwave frequency of about 9.2 GHz [12-14].

The sample temperature has been varied between the ranges 100 – 400 K by regulating the flow of cold nitrogen gas. A proper gas flow was achieved by controlling the power input to a heater, immersed in a liquid-nitrogen (LN₂) container, with the aid of a proportional, integral and derivative (PID) temperature controller. The controlling sensor used was a pre-calibrated copper-constantan thermocouple situated just outside the microwave cavity. The temperature at the sample site was monitored by another pre-calibrated copper-constantan thermocouple in close contact with the sample. The temperature stability achieved at the sample site was within ± 50 mK. The sample temperature was varied from 100 – 400 K by heating air blown through the cavity by a compressor. EPR spectrum has been recorded on empty EPR quartz tube along with thermocouple to check the presence and/or absence of any magnetic impurities of such combination.

References

1. Sajjadi, S. Pooyan, *Sol-gel process and its application in nanotechnology*, J. Polym. Eng., **13**, p38 (2005).
2. K.E.V. Schafhautl, *The latest geological hypotheses and their relation to science in general*, The royal Bavarian academy of sciences, **20**, p557 (1845).
3. A. Rabenau, *The Role of Hydrothermal Synthesis in Preparative Chemistry*, Angew. Chem., **24**, p1026 (1985)
4. K. Byrappa and M. Yoshimura, *Handbook of hydrothermal technology*, Noyes publications, p1 (2001).
5. B. D. Cullity, *Elements of X-ray diffraction*, 2nd Ed., Addison-Wesley Publishing Co. Inc., p189 (1978).
6. J. I. Goldstein, D.E. Joy, D.C. Lyman, C.E. Echlin, P. Lifshin, E. Sawyer, L. Michael, J.R., *Scanning Electron Microscopy and X-Ray Microanalysis*, 3rd edition, p21 (2003).
7. G. H. Michler, *Electron Microscopy of Polymers*, Springer, p87 (2008).
8. J. H. Hinken, “*Superconductor Electronics*”, Springer-Verlag Berlin and Heidelberg GmbH & Co. KG, p4 (1989).
9. J. A. Weil, J. R. Bolton, “*Electron paramagnetic resonance*”, 2nd Ed., A John Wiley and sons inc., publications, p58 (2007).
10. B.M. Weckhuysen, R. Heidler, R.A. Schoonheydt, *Electron Spin Resonance Spectroscopy*, Mol. Sieves, **4**, p295 (2004).
11. A. Lund, M. Shiotani, S. Shimada, *Principles and Applications of ESR Spectroscopy*, Springer, p79 (2011).

12. S.N. Kaul and V. Siruguri, *Ferromagnetic resonance evidence for long-range ferromagnetic ordering in amorphous Fe-rich $Fe_{100-x}Zr_x$ alloys*, J. Phys. Condens. Matter, **4**, p505 (1992).
13. S.N. Kaul and V. Siruguri, *Origin of magnetism in amorphous $Ni_{81.6}B_{18.4}$ alloy*, J. Phys. F: Met. Phys., **17**, pL255 (1987).
14. O.Borang, S. Srinath, S. N. Kaul, Y. Sundarayya, *Temperature driven tuning of the structure and magnetic properties of oxides of erbium and chromium at nanoscale*, IJRET, **06**, p14 (2007).

Chapter 3

Synthesis and Characterization of RCrO_4 and RCrO_3 Nanoparticles

3.1 Introduction

Since many years, various research groups have been working on the rare earth chromates and orthochromites have been synthesized by different techniques. Some of the methods used to synthesize RCrO_3 aerosol-gel synthesis, hydrothermal synthesis [1–3], solid state synthesis [4–9], microwave process [10–11], solution combustion method [12–14], citrate chemical solution [15–16]. Though, no attention has been given to RCrO_4 in the past, few research groups have started working on RCrO_4 . Some of the methods that include synthesizing RCrO_4 are solid state reaction synthesis [17–18], thermal process [19–21], hydrothermal synthesis [22], Nitrate precursor method [23 – 24], precursor method [25] etc. Few groups have reported the synthesis of RCrO_4 even at ambient pressure [26–27]. However, synthesis of RCrO_4 and RCrO_3 in nanoparticles has been given less attention to the best of our knowledge. It has been reported that the chromates undergoes a structural rearrangement and reduces to orthochromites at high temperatures [26]. In view of the present discussion, the present doctoral thesis has been aimed at the synthesis of homogeneous single phase RCrO_4 and RCrO_3 ($\text{R} = \text{Sm}, \text{Eu}, \text{Gd}, \text{Dy}$ and Er) through a modified sol-gel route followed by hydrothermal method and temperature driven tuning of the crystal structure of RCrO_4 and RCrO_3 nanoparticles.

3.2 Synthesis Procedure

Sol-gel synthesis route

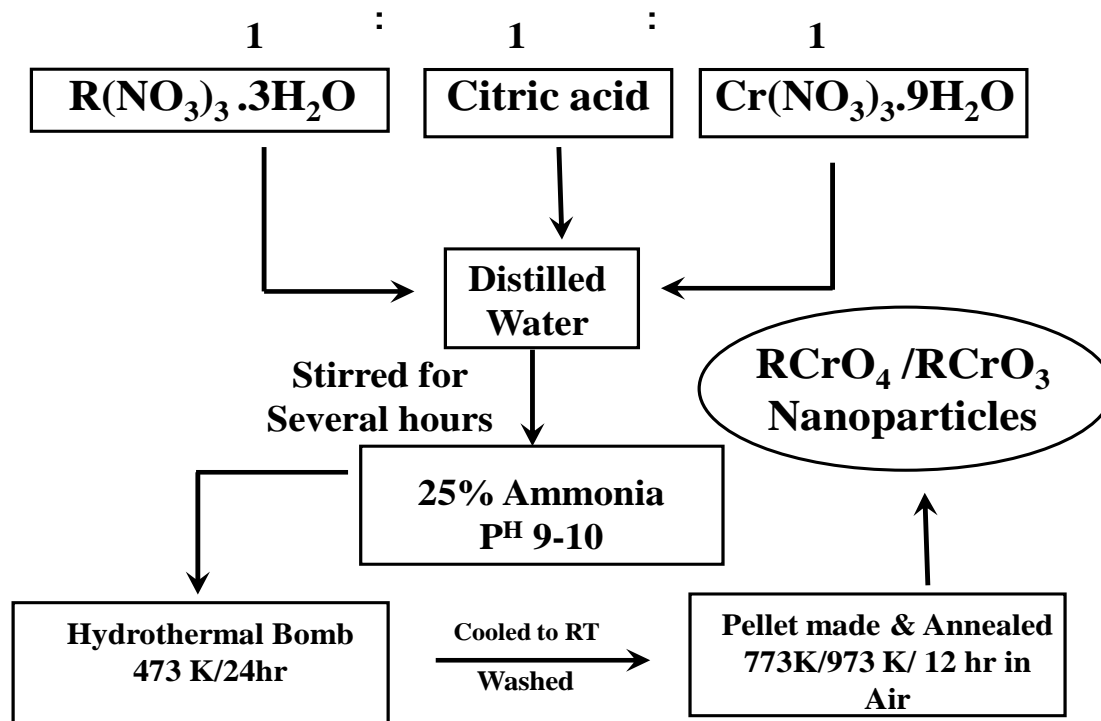


Fig. 1. Block diagram of the synthesis procedure for RCrO_4 and RCrO_3 nanoparticles.

For the present doctoral work, we have adopted modified sol-gel method along with hydrothermal synthesis followed by annealing, to obtain the homogeneous single phase nanocrystalline RCrO_4 and RCrO_3 powders from hydrated nitrate salts of rare earth and chromium [3, 4]. In the present case, the stoichiometric amounts of chromium nitrate, $\text{Cr}(\text{NO}_3)_3 \cdot 9\text{H}_2\text{O}$ (Alfa-aesar, 99.9%), rare earth nitrate hydrate $\text{R}(\text{NO}_3)_3 \cdot 3\text{H}_2\text{O}$, (Alfa-aesar, 99.9%, $\text{R} = \text{Sm}, \text{Eu}, \text{Gd}, \text{Dy}$ and Er), and citric acid (Merck, 99.5%) with 1:1:1 molar ratio were dissolved in the deionized water. A sol with pH ~ 10 is prepared by the addition of ammonia solution which is then transferred to a 200 ml bomb for hydrothermal treatment at 473 K for 24 h. The precipitate was, in turn, filtered, washed with deionized water and

dried at 423 K for 24 h. Samples are obtained by annealing the green pellets made from the as-synthesized powder at 773 K and 973 K in air for 12 hours to obtain RCrO_4 and RCrO_3 nanoparticles respectively. The same has been depicted in the form of a block diagram as shown in Figure 1.

3.3 Characterization

3.3.1 Crystal Structure

The nature of crystallinity and structural information of the powder samples have been characterised by X-ray powder diffraction (XRD) using Bruker D8 Advance diffractometer with $\text{Cu-K}\alpha$ radiation ($\lambda = 1.54056 \text{ \AA}$). The X-ray diffractograms of as-synthesized samples obtained from hydrothermal synthesis are found to be amorphous. The X-ray diffractograms of the annealed samples are analysed for Rietveld profile matching by Full-Prof software package [28]. The XRD patterns of the samples annealed at 773 K reveal the formation of zircon-type tetragonal phase of RCrO_4 with space group $I41/amd$, D_{4h}^{19} symmetry [4]. Figures 2–6 shows the Rietveld profile matching of the X-ray diffractograms of SmCrO_4 , EuCrO_4 , GdCrO_4 , DyCrO_4 , and ErCrO_4 respectively. Here the black open circles denote the intensity of the observed X-ray diffraction pattern, I_{obs} , the red line passing through the open circles denote the intensity of the simulated X-ray diffraction pattern, I_{cal} . The blue line indicates the observed intensity and calculated intensity ($I_{obs} - I_{cal}$). The green vertical lines indicate the Bragg's position for the respective reflections. The obtained lattice parameters a , b , c and volume of the unit cell of RCrO_4 ($R = \text{Sm, Eu, Gd, Dy, Er}$) are given in Table 1. The calculated volume of the unit cell of RCrO_4 is found to decrease with increase in the atomic number of the rare earth, and is in accordance with the literature [21–24]. The XRD patterns of the samples annealed at 973

K reveal the formation of orthorhombic phase of perovskite RCrO_3 with space group $Pbnm$, D_{4h}^{19} symmetry [3]. Figures 7-11 show the Rietveld profile matching of the X-ray diffractograms of SmCrO_3 , EuCrO_3 , GdCrO_3 , DyCrO_3 , and ErCrO_3 respectively. The obtained lattice parameters a , b , c and volume of the unit cell of RCrO_3 ($R = \text{Sm, Eu, Gd, Dy, Er}$) are given Table 2. The calculated volume of the unit cell of RCrO_3 is found to decrease with increase in the atomic number of the rare earth, and is in accordance with the literature [1–3].

The average crystallite size of RCrO_4 and RCrO_3 has been estimated using Scherer's formula [29], given by

$$t = \frac{0.94 \lambda}{B \cos \theta_B} \quad \dots (1)$$

Where

t – Average crystallite size

λ – Wavelength of the X-rays (= 1.54056 Å)

B – Full-width at half maximum (FWHM) of the diffraction peak

θ_B – Half of the Bragg's position

The average crystallite size of RCrO_4 for $R = \text{Sm, Eu, Gd, Dy}$ and Er , estimated from Scherer's formula is found to be 29(2), 24(1), 46(1), 52(1) and 33(2) nm respectively. And the average crystallite size of RCrO_3 for $R = \text{Sm, Eu, Gd, Dy}$ and Er is found to be 37(1), 31(1), 32 (1), 41(1), 32(1) nm respectively. It is important to note that the high pressure involved during the hydrothermal synthesis facilitates the stabilization of the metastable Cr^{5+} resulting the monodisperse single phase RCrO_4 which is unstable at high temperature.

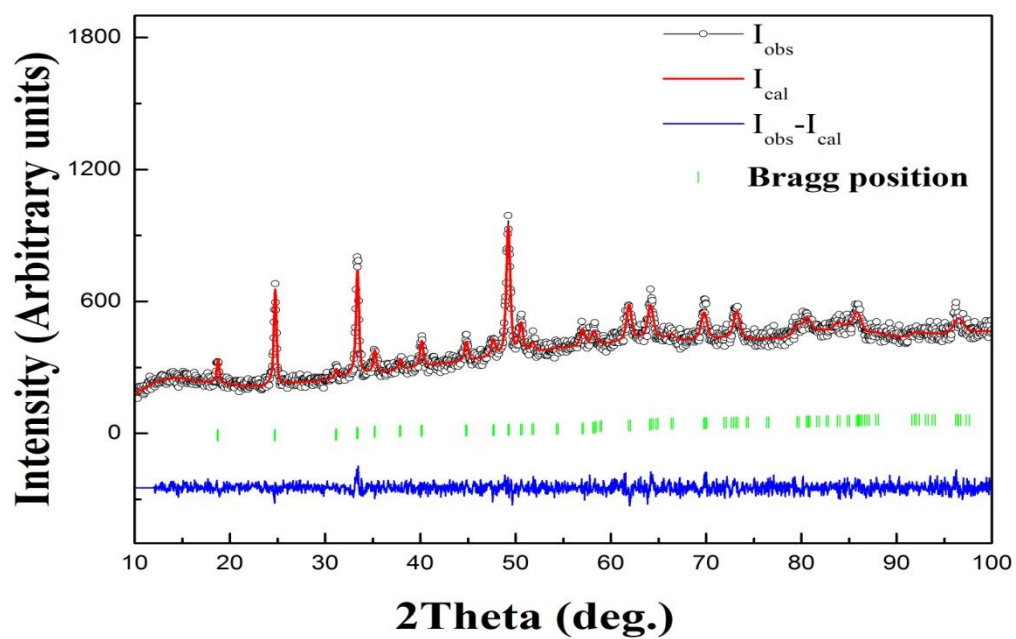


Fig. 2. Rietveld profile matching of the X-ray diffractogram of SmCrO_4 .

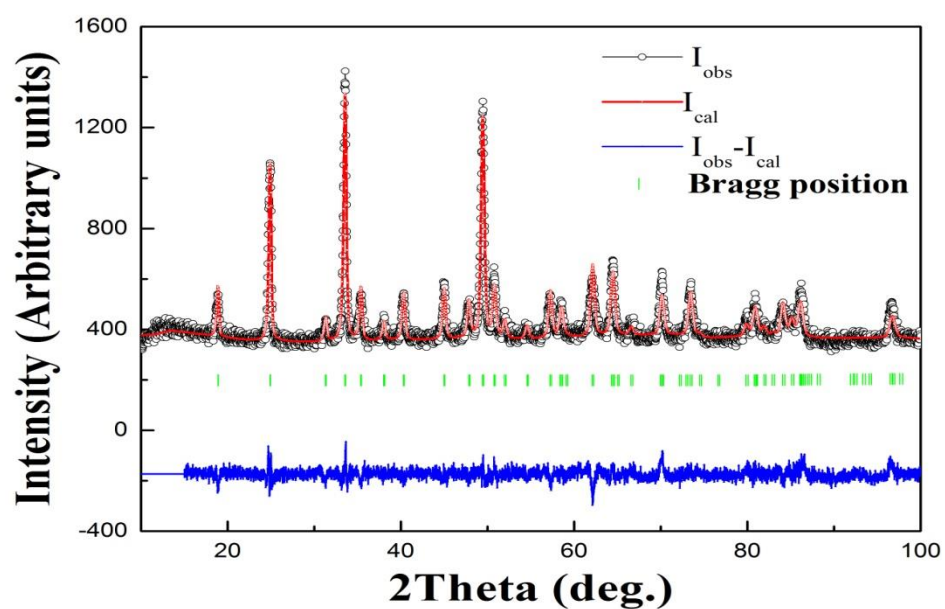


Fig. 3. Rietveld profile matching of the X-ray diffractogram of EuCrO_4 .

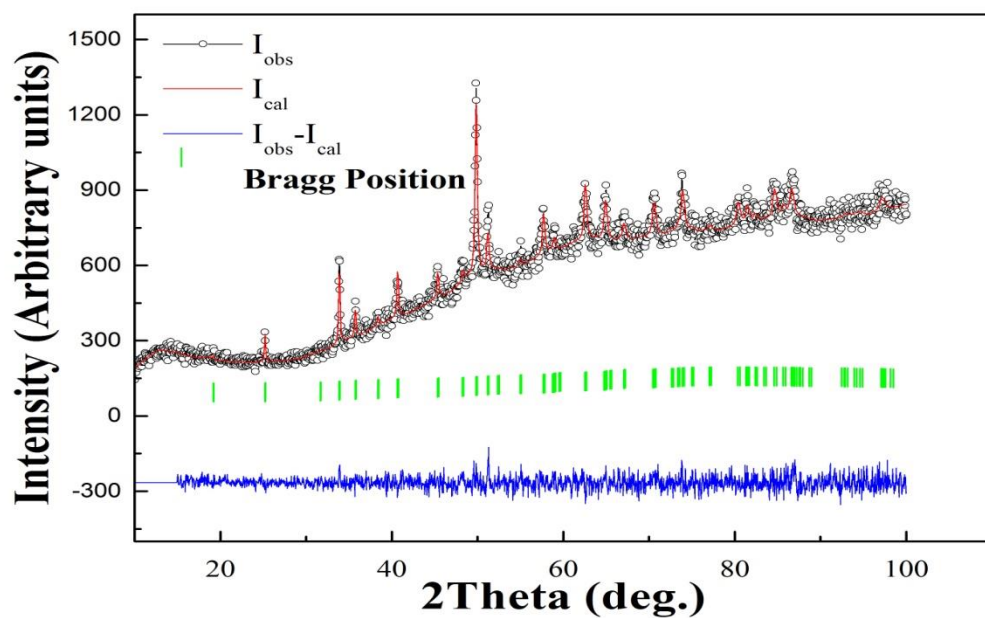


Fig. 4. Rietveld profile matching of the X-ray diffractogram of GdCrO_4 .

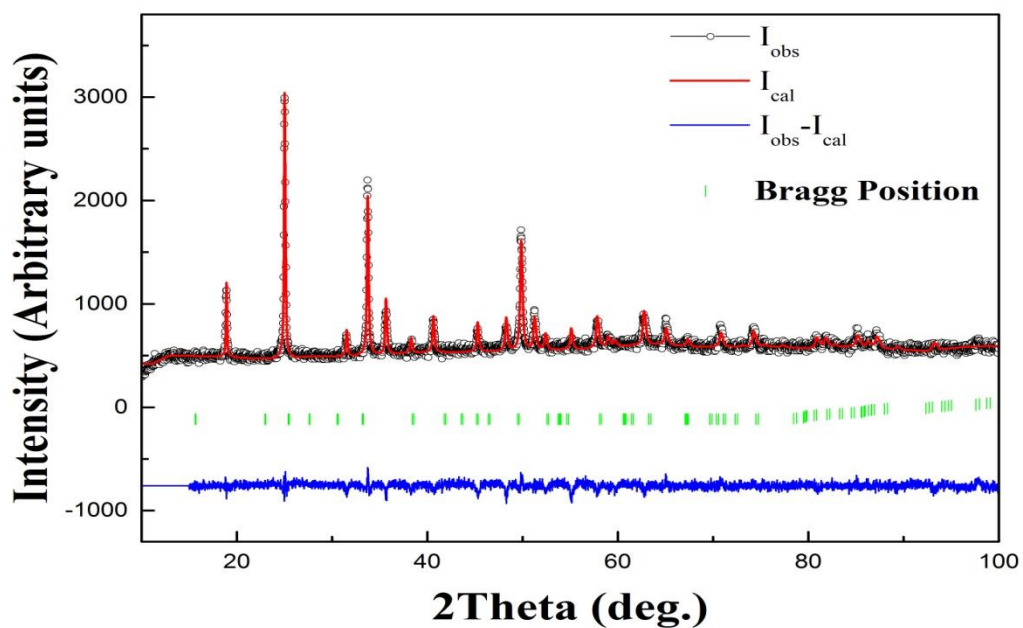


Fig. 5. Rietveld profile matching of the X-ray diffractogram of DyCrO_4 .

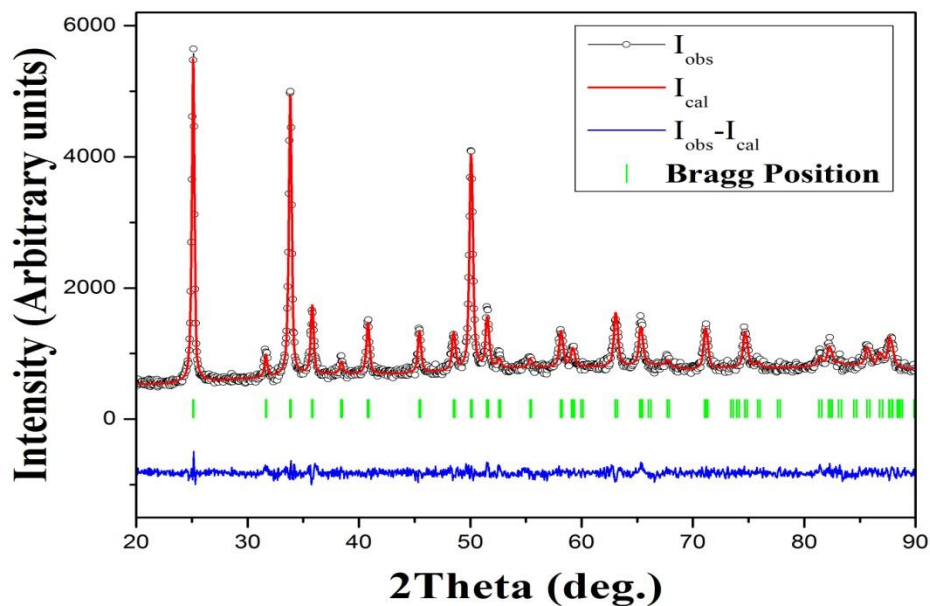


Fig. 6. Rietveld profile matching of the X-ray diffractogram of ErCrO_4 .

Table 1: Obtained lattice parameters a , b , c and volume of the unit cell of RCrO_4

($R = \text{Sm, Eu, Gd, Dy, Er}$)

Sl. No.	RCrO_4	Lattice parameters			Vol. of the
		a (Å)	b (Å)	c (Å)	Unit cell (Å ³)
1	SmCrO_4	7.2317(1)	7.2317(2)	6.3353(1)	331.34
2	EuCrO_4	7.2205(2)	7.2005(1)	6.3269(2)	328.94
3	GdCrO_4	7.2075(1)	7.2075(2)	6.3230(1)	328.48
4	DyCrO_4	7.1348(2)	7.1348(1)	6.2669(2)	319.02
5	ErCrO_4	7.1024(1)	7.1024(2)	6.2496(1)	315.26

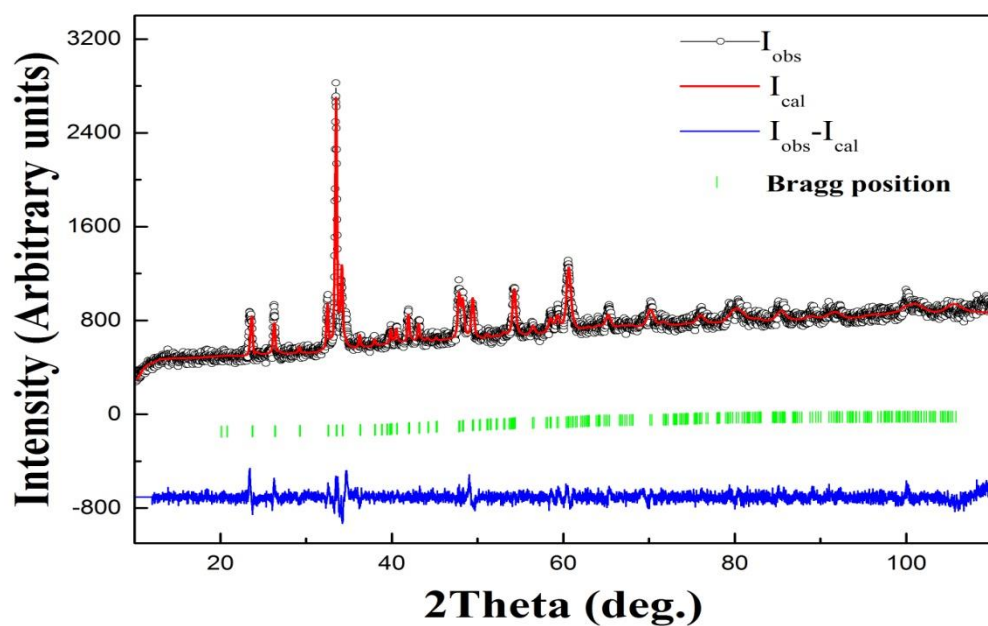


Fig. 7. Rietveld profile matching of the X-ray diffractogram of SmCrO_3 .

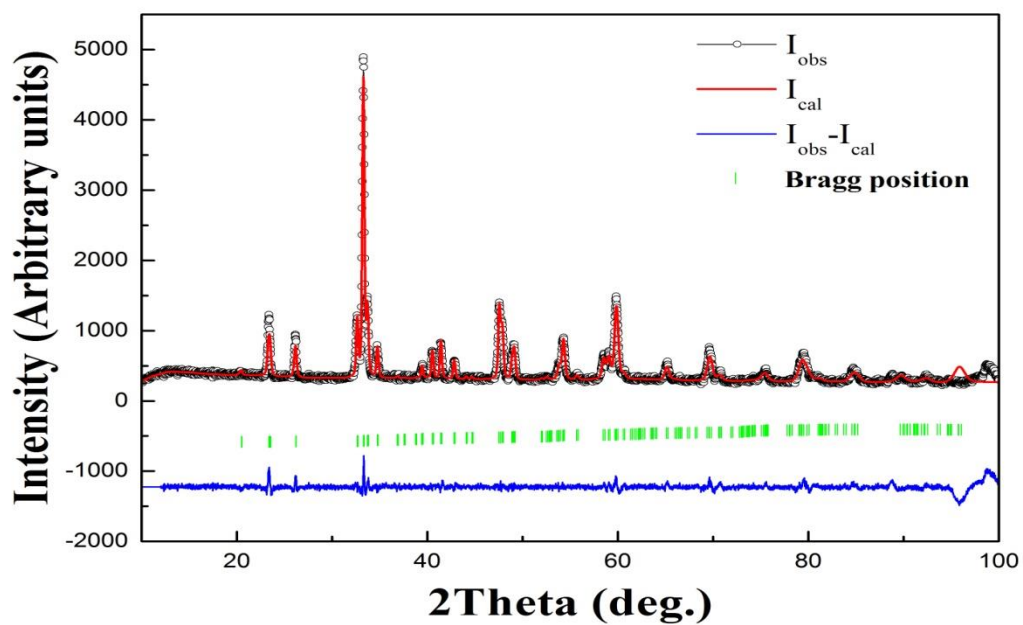


Fig. 8. Rietveld profile matching of the X-ray diffractogram of EuCrO_3 .

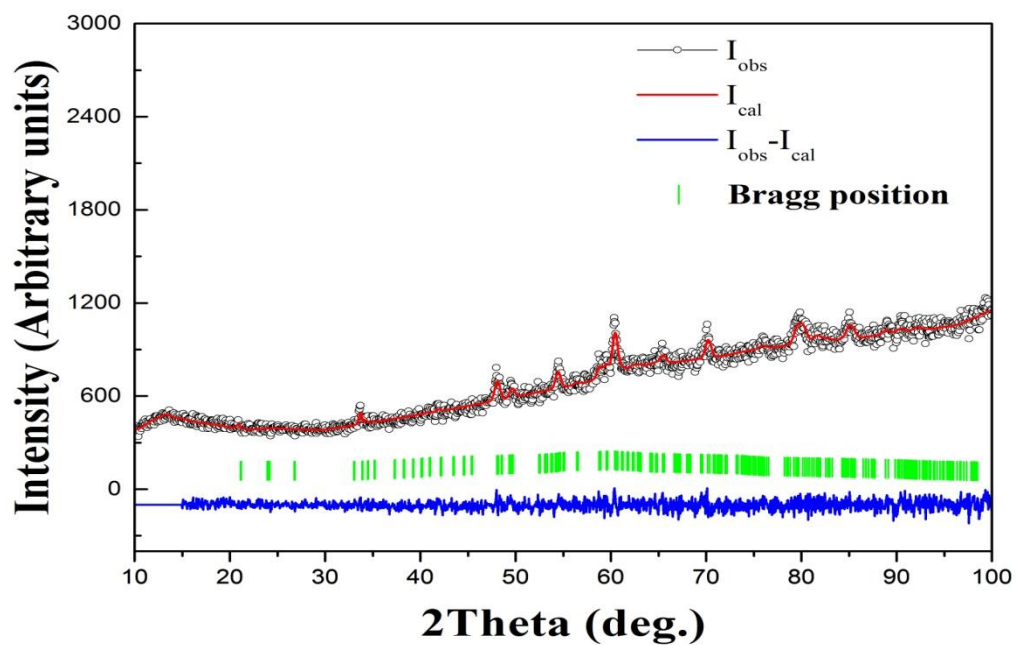


Fig. 9. Rietveld profile matching of the X-ray diffractogram of GdCrO₃.

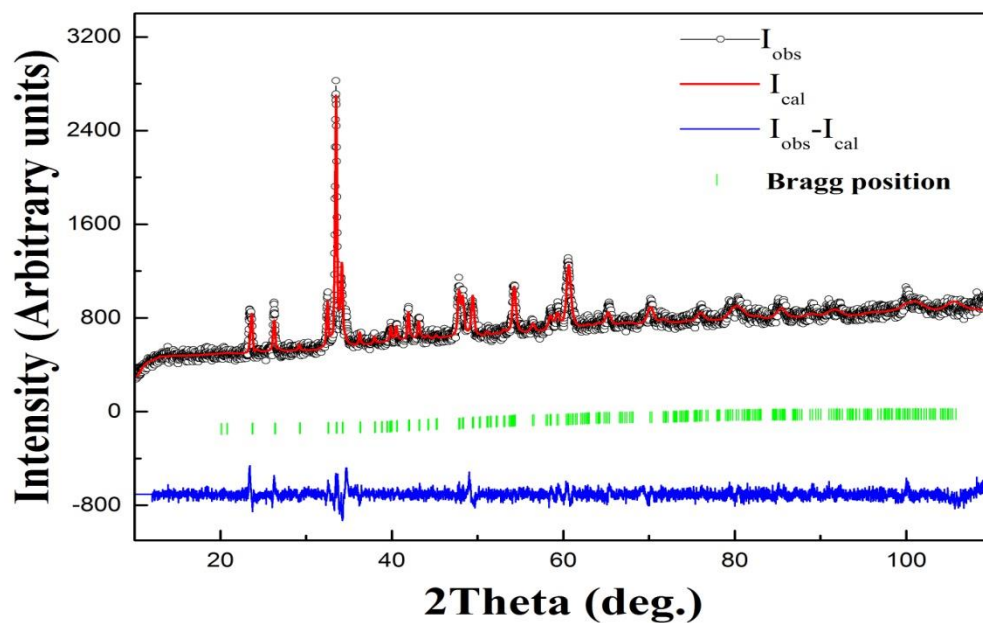


Fig. 10. Rietveld profile matching of the X-ray diffractogram of DyCrO₃.

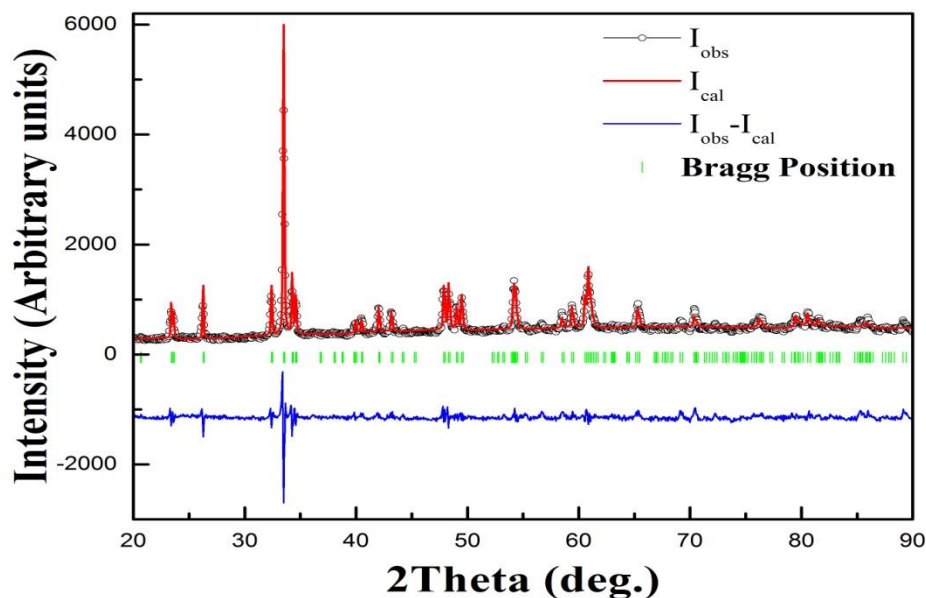


Fig. 11. Rietveld profile matching of the X-ray diffractogram of ErCrO_3 .

Table 2: Obtained lattice parameters a , b , c and volume of the unit cell of RCrO_3

($R = \text{Sm, Eu, Gd, Dy, Er}$)

Sl. No.	RCrO_3	Lattice parameters			Volume of the Unit cell (\AA^3)
		a (\AA)	b (\AA)	c (\AA)	
1	SmCrO_3	5.5017(2)	7.6438(1)	5.3693(2)	225.81
2	EuCrO_3	5.5177(1)	7.6328(2)	5.3472(1)	225.20
3	GdCrO_3	5.5446(2)	7.6101(1)	5.3183(2)	224.41
4	DyCrO_3	5.281050	7.585068	5.550888	222.35
5	ErCrO_3	5.518594	7.525871	5.229040	217.17

3.3.2 Morphological analysis of RCrO_4 and RCrO_3 nanoparticles

The morphology (shape and size) of the RCrO_4 and RCrO_3 nanoparticles has been studied by using Carl Zeiss ULTRA-55 field-emission scanning electron microscope (FESEM). To visualize the shape and size of the particles, powder samples of RCrO_4 and RCrO_3 have been dispersed in Acetone/ Ethanol solutions using an ultra-sonicator. Two to three drops of the dispersion was taken on a stub, dried in air, sputtered with gold, and mounted in the FESEM machine under high vacuum.

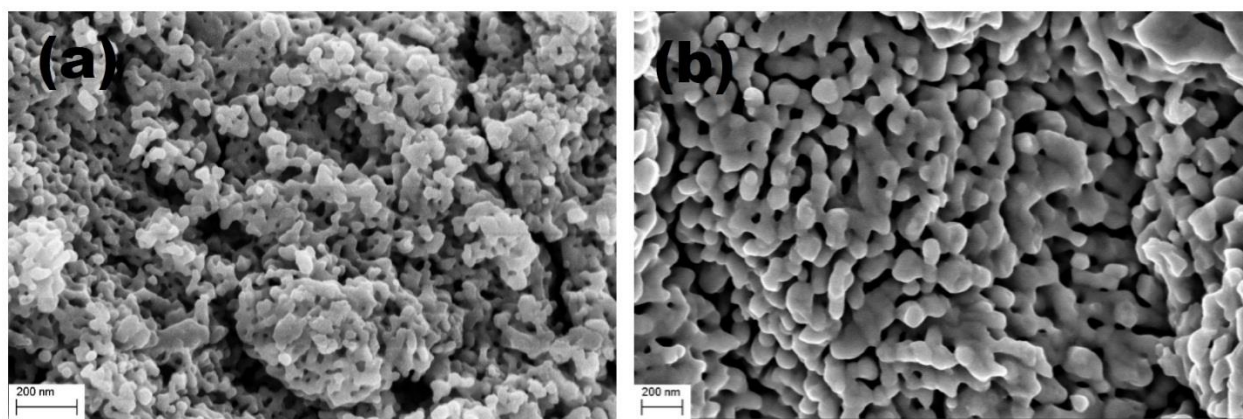


Fig.12. Morphological images of (a) SmCrO_4 and (b) SmCrO_3 nanoparticles by FESEM.

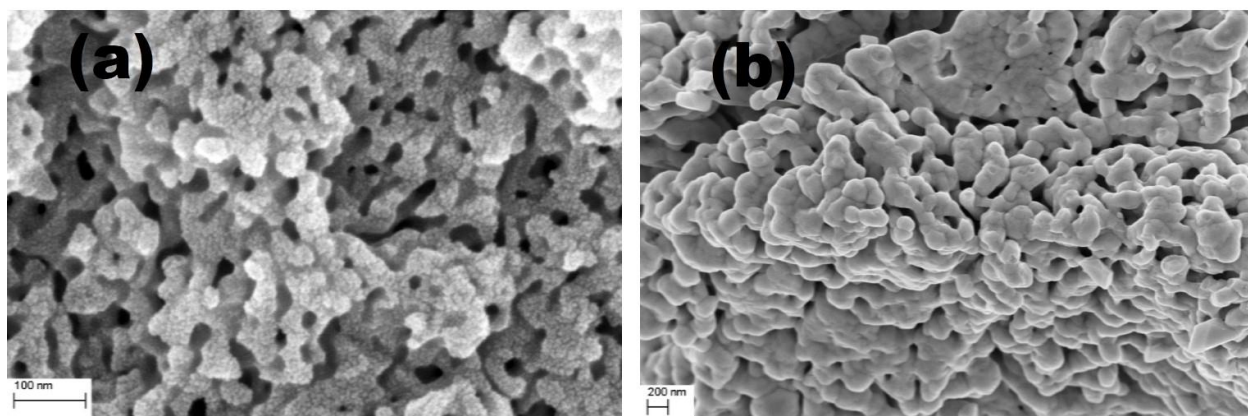


Fig.13. Morphological images of (a) EuCrO_4 and (b) EuCrO_3 nanoparticles by FESEM.

Figures 12 (a and b), 13 (a and b), 14 (a and b), 15 (a and b) and 16 (a and b) shows the morphological images of SmCrO_4 , SmCrO_3 , EuCrO_4 , EuCrO_3 , GdCrO_4 , GdCrO_3 , DyCrO_4 , DyCrO_3 , ErCrO_4 , and ErCrO_3 , respectively. These images depict the uniform size distribution of nanoparticles that has been possible due to adoption of hydrothermal synthetic procedure.

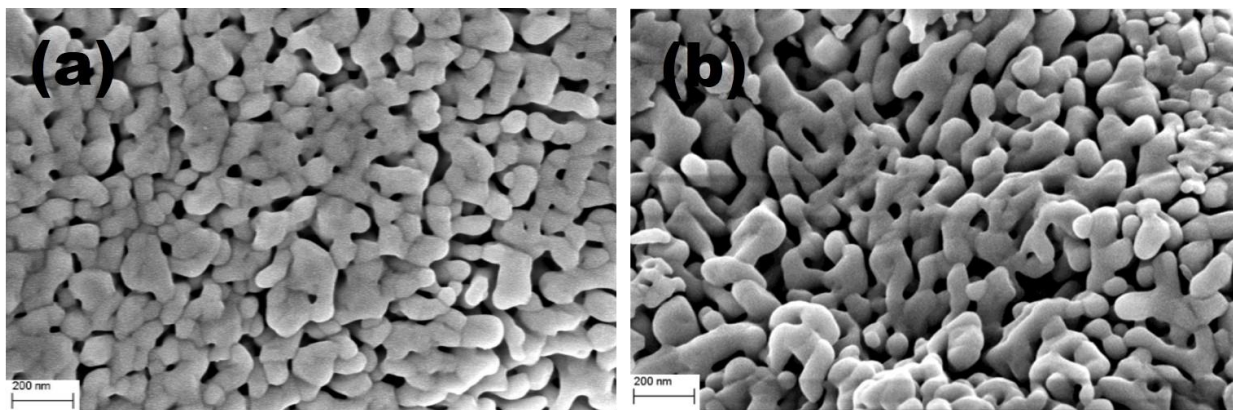


Fig.14. Morphological images of (a) GdCrO_4 and (b) GdCrO_3 nanoparticles by FESEM.

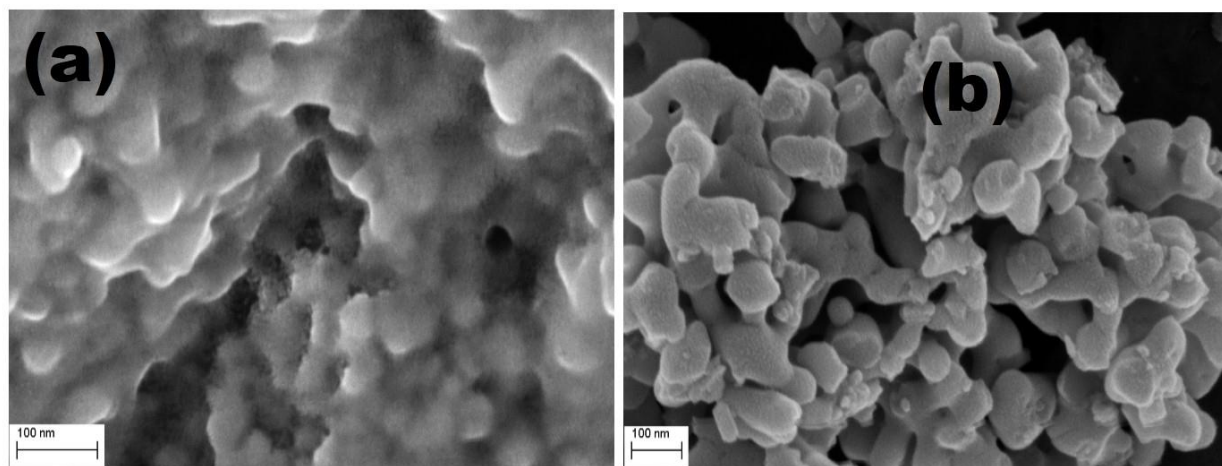


Fig.15. Morphological images of (a) DyCrO_4 and (b) DyCrO_3 nanoparticles by FESEM.

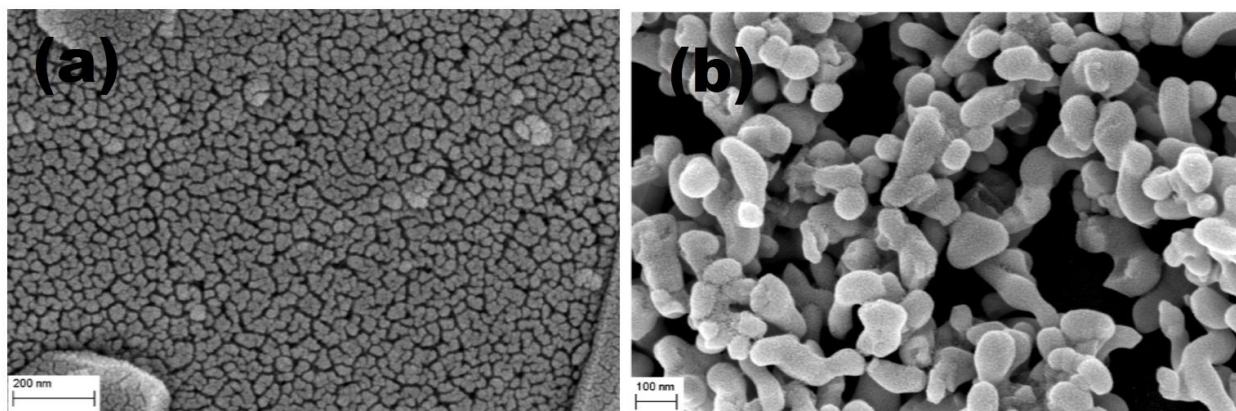


Fig.16. Morphological images of (a) ErCrO_4 and (b) ErCrO_3 nanoparticles by FESEM.

Table 3: The approximate particle sizes of RCrO_4 and RCrO_3 nanoparticles.

Approximate Particle Size (nm)		Approximate Particle Size (nm)	
RCrO_4 Nanoparticles		RCrO_3 Nanoparticles	
SmCrO_4	30	SmCrO_3	70
EuCrO_4	30	EuCrO_3	160
GdCrO_4	70	GdCrO_3	150
DyCrO_4	40	DyCrO_3	90
ErCrO_4	20	ErCrO_3	70

It is to be noted that RCrO_4 ($\text{R} = \text{Sm}, \text{Eu}, \text{Gd}, \text{Dy}$ and Er) nanoparticles have been obtained by annealing the as-synthesized amorphous at 773 K for 12 hr at ambient pressure in air. This results in the formation of RCrO_4 , $\text{R} = \text{Sm}, \text{Eu}, \text{Gd}, \text{Dy}$ and Er nanoparticles respectively with sizes 30, 30 70, 40 and 20 nm. RCrO_3 nanoparticles have been obtained by annealing the as-synthesized amorphous powder at 973 K for 12 hr at ambient pressure in air with particle sizes 70, 160, 150, 90 and 70 nm respectively for RCrO_3 with $\text{R} = \text{Sm}$,

Eu, Gd, Dy and Er, as given in Table 3. It is evident from the annealing temperatures that RCrO_4 forms at low temperatures with lesser particle size and RCrO_3 at high temperatures with higher particle sizes respectively. That is the temperatures involved in the synthesis control the growth of particles and the size of the particle in turn favours the formation of tetragonal RCrO_4 and orthogonal RCrO_3 crystalline phases respectively. The size of the particle in turn tunes the magnetic properties. This implies the size dependent tuning of the crystal structures and magnetic properties of rare earth chromium oxides at nanoscale with the aid of annealing temperature.

3.3.3 Elemental Analysis of RCrO_4 and RCrO_3 nanoparticles

The elemental analysis, i.e. the atomic percentage and/ or the weight percentage of RCrO_4 and RCrO_3 nanoparticles has been examined by an elemental analysis attachment provided in the Carl Zeiss–ULTRA-55 field-emission scanning electron microscopy (FESEM). To analyse the presence of R, Cr and O, powder samples of RCrO_4 and RCrO_3 have been dispersed in Acetone/ Ethanol solutions using an ultra-sonicator. Two to three drops of the dispersion was taken on a stub, dried in air, sputtered with gold, and mounted in the FESEM machine under high vacuum at an accelerating voltage of 20 kV. The representative EDAX spectra for RCrO_4 (R = Gd) and RCrO_3 (R = Er) has been given in Figures 17 and 18 respectively.

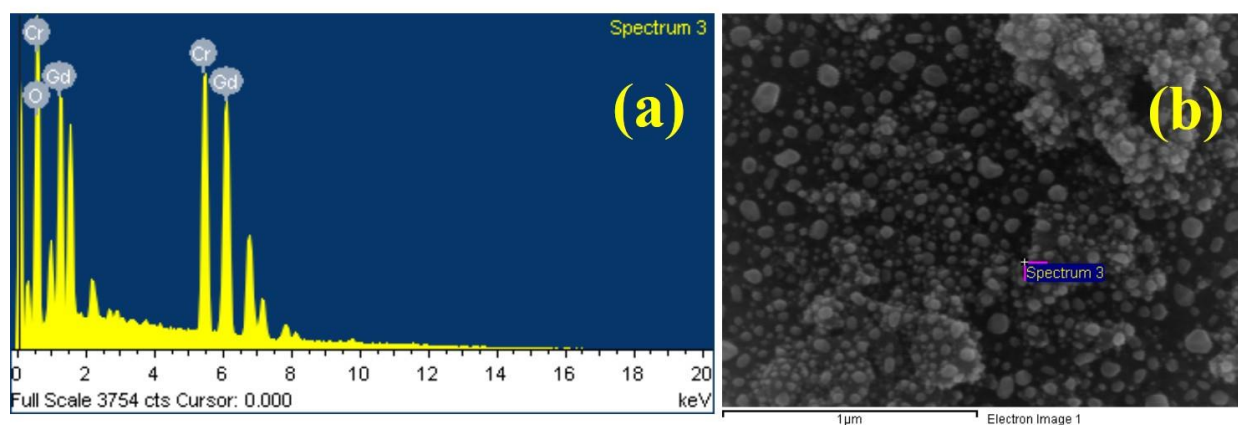


Fig.17. (a) The EDAX Spectrum of GdCrO₄ nanoparticles, and
(b) The location of EDAX recorded on GdCrO₄ nanoparticles.

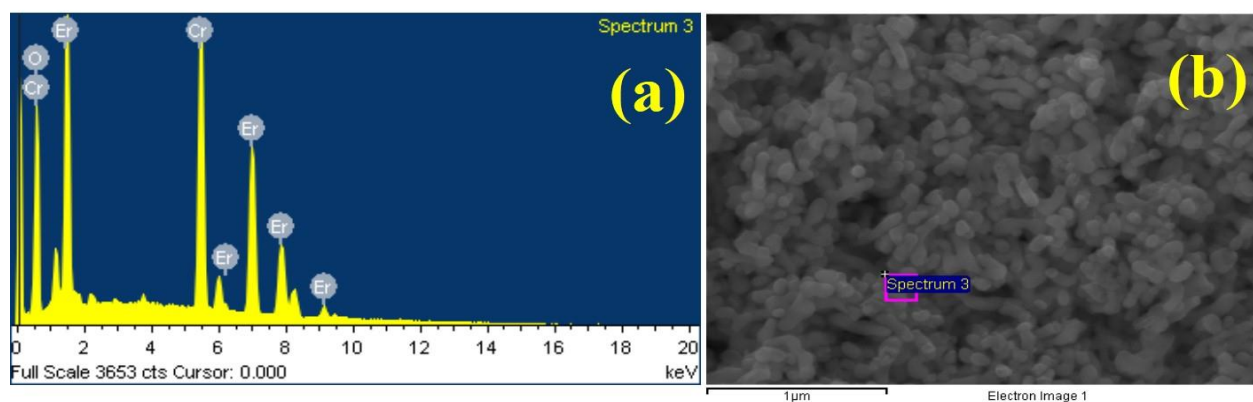


Fig.18. (a) The EDAX Spectrum of ErCrO₃ nanoparticles, and
(b) The location of EDAX recorded on ErCrO₃ nanoparticles.

Figure 17 (a and b) shows the elemental composition spectrum of GdCrO₄ nanoparticles and the location of the GdCrO₄ nanoparticles at which the EDAX spectrum has been recorded. Figure 18 (a and b) shows the elemental composition spectrum of ErCrO₃

nanoparticles and the location of the ErCrO_3 nanoparticles at which the EDAX spectrum has been recorded. Table 4 shows the weight percentage and atomic percentage of R, Cr and O in GdCrO_4 and ErCrO_3 nanoparticles. It has been found that the ratio of atomic percentages of Gd, Cr and O in GdCrO_4 nanoparticles is 1:1:4 within the experimental error. Similarly, the ratio of atomic percentages of Er, Cr and O in ErCrO_3 nanoparticles is found to be 1:1:3. Thus, elemental analysis confirms the presence of R, Cr and O in RCrO_4 and RCrO_3 nanoparticles in the ratios 1:1:4 and 1:1:3 respectively.

Table 4: The weight percentage and atomic percentage of R, Cr and O in GdCrO_4 and ErCrO_3 nanoparticles.

GdCrO₄ Nanoparticles			ErCrO₃ Nanoparticles		
Element	Weight Percentage	Atomic Percentage	Element	Weight Percentage	Atomic Percentage
Gadolinium	57.99	16.86	Erbium	59.83	18.52
Chromium	18.65	16.39	Chromium	21.64	21.54
Oxygen	23.36	66.75	Oxygen	18.53	59.94
Total	100	100	Total	100	100

3.4 Conclusions

Homogeneous single phase zircon-type RCrO_4 and perovskite RCrO_3 nanoparticles have been synthesized through a modified sol-gel route followed by hydrothermal method from a single precursor. Heat treatment of the as-synthesized amorphous powder at 773 K favours the crystallization of zircon-type tetragonal RCrO_4 with Chromium stabilized in

unusual Cr^{5+} state and 973 K results the of formation orthorhombic RCrO_3 with a stable Cr^{3+} at ambient pressure. The high pressure involved during the hydrothermal synthesis facilitates the stabilization of the metastable Cr^{5+} resulting the monodisperse single phase RCrO_4 which is unstable at high temperature. It has been observed that the formation of RCrO_4 nanoparticles with smaller sizes while an increase of particle has been observed in respective RCrO_3 nanoparticles. The particle size plays a major role in tuning the crystal structures and respective magnetic properties of rare earth chromium oxides at nanoscale with the aid of annealing temperature. Elemental analysis of the samples demonstrated the presence of R, Cr and O in RCrO_4 and RCrO_3 nanoparticles in the ratios 1:1:4 and 1:1:3 respectively.

References

1. K. Sardar, Martin R. Lees, R.J. Kashtiban, J. S. and R.I. Walton, *Direct Hydrothermal Synthesis and Physical Properties of Rare earth and Yttrium Orthochromite Perovskites*, Chem. Mater., **23**, p48 (2011).
2. M.C. Weber, J. Kreisel, P.A. Thomas, M. Newton, K. Sardar, and R. I. Walton, *Phonon Raman scattering of $RCrO_3$ perovskites ($R = Y, La, Pr, Sm, Gd, Dy, Ho, Yb, Lu$)*, Phy. Rev. B, **85**, p054303 (2012).
3. O. Borang, S.Srinath, S.N. Kaul, and Y. Sundarayya, *Probing the magnetic transitions in europium chromite through electron paramagnetic resonance*, Fazl Ali College Journal, **7**, p120-127 (2017).
4. A. Midya, N. Khan, D. Bhoi and P. Mandal, *3d-4f spin interaction and field-induced metamagnetism in $RCrO_4$ ($R = Ho, Gd, Lu$) compounds*, J. Appl. Phys., **115**, p17E114 (2014)
5. S. Kumar, I. Coondoo, M. Vasundhara, S. Kumar, A.L. Kholkin, and N. Panwar, *Structural, Magnetic, Magnetocaloric and Specific heat Investigations on Mn doped $PrCrO_3$ Orthochromites*, J. Phys.: Condens. Matter, **29**, p195802 (2017).
6. K.R.S.P. Meher, A. Wahl, A. Maignan, C. Martin, and O. I. Lebedev, *observation of electric polarization reversal and magnetodielectric effect in orthochromites: a comparison between $LuCrO_3$ and $ErCrO_3$* ,), Phy. Rev. B., **89**, p144401 (2014)
7. J.-S. Zhou, J. A. Alonso, V. Pomjakushin, J. B. Goodenough, Y. Ren, J.-Q. Yan and J.-G. Cheng, *Intrinsic structural distortion and superexchange interaction in the orthorhombic rare earth perovskites $RCrO_3$* , Phys. Rev. B, **81**, p214115 (2010).

8. B. Tiwari, M.K. Surendra and M.S.R. Rao, *HoCrO₃ and YCrO₃: a comparative study*, J. Phys. Condens. Matter, **25**, p216004 (2013).
9. V.S. Bhadram, D. Swain, R Dhanya, M. Polentarutti, A. Sundaresan and C. Narayana, *Effect of pressure on octahedral distortions in RCrO₃(R= Lu, Tb, Gd, Eu, Sm): the role of R-ion size and its implications*, Mater Res Express, **1** , p026111 (2014).
10. J.P. Gonjal, R. Schmidt, D. Avila, U. Amador, E. Moran, *Structural and physical properties of microwave synthesized orthorhombic perovskite erbium chromite ErCrO₃*, J. Eur. Ceram. Soc, **32**, p611 (2012).
11. R. Schmidt, J.P. Gonjal, D. Ávila, U. Amador and E. Morán, *Electron microscopy of microwave-synthesized rare earth chromites, microscopy*, Adv. Sci. Res. Edu., **2**, p819 (2014).
12. M. Taheri and F.S. Razavi, *Magnetic structure, magnetoelastic coupling, and thermal properties of EuCrO₃ nanopowders*, Phys.Rev.B., **93**, p104414 (2016)
13. M. Taheri, R.K. Kremer, S. Trudel and F.S. Razavi, *Exchange bias effect and glassy-like behavior of EuCrO₃ and CeCrO₃ nano-powders*, J. Appl. Phys., **118**, 124306 (2015).
14. A. Duran, A.M.A. Lopez , E.C. Martinez , M.G. Guaderrama, E.Moran , M.P.Cruz , F. Fernandez, M.A.A. Franco, *Magneto thermal and dielectric properties of biferroic YCrO₃ prepared by combustion synthesis*, J. Solid State Chem., **183** , p1863 (2010).
15. A. McDannald, L. Kuna, M.S. Seehra, M. Jain, *Magnetic exchange interactions of rare earth-substituted DyCrO₃ bulk powders*, Phys. Rev. B ., **91**, p224415 (2015).
16. T. Ahmad and I.H. Lone, *Citrate precursor synthesis and multifunctional properties of YCrO₃ nanoparticles*, New J. Chem., **40**, p3216 (2016).

17. Y.W. Long, L.X. Yang, Y. Yu, F.Y. Li, R.C. Yu, and C.Q. Jin, *Synthesis, structure, magnetism and specific heat of $YCrO_4$ and its zircon-to-scheelite phase Transition*, Phys. Rev. B, **75**, p104402 (2007).
18. A. Midya, N. Khan, D. Bhoi, and P. Mandal, *3d-4f spin interaction induced giant magnetocaloric effect in zircon-type $DyCrO_4$ and $HoCrO_4$ compounds*, Appl. Phys. Lett, **103**, p092402 (2013).
19. E. Palacios, C. Tomasi, R. Saez-Puche, A. J. Dos santos-Garcia, F. Fernandez-Martinez, and R. Burriel, *Effect of Gd polarization on the large magnetocaloric effect of $GdCrO_4$ in a broad temperature range*, Phy. Rev. B, **93**, p064420 (2016)
20. R. Shukla, V. Bedekar, S.M. Yusuf, P. Srinivasu, A. Vinu, and A.K. Tyagi, *Nanocrystalline $HoCrO_4$: Facile Synthesis and Magnetic Properties*, J. Nanosci. Nanotechnol., **9**, p501 (2009)
21. E. Jiménez, J. Isasi, R.S. Puche, *Synthesis, structural characterization and magnetic properties of $RCrO_4$ oxides $R = Nd, Sm, Eu$ and Lu* , J. Alloys Comp. **312**, p53 (2000).
22. Y. Sundarayya, K.A. Kumar, R. Sondge, S.Srinath and S.N. Kaul, *hydrothermal synthesis and magnetic properties of $ErCrO_4$ nanoparticles*, solid state physics, **1591 A**, p529 (2014).
23. E. Jiménez, J. Isasi, M.T. Fernández, R. Sáez-Puche, *Magnetic behavior of $ErCrO_4$ oxide*, J. Alloys Comp., **344**, 369 (2002).
24. E.J. Melero, P.C.M. Gubbens, M.P. Steenvoorden, S.Sakarya, A.Goosens, P.D.D. Reotier, A. Yaouanc, J. R. Carvajal, B. Beuneu, J. Isasi, R. S. Puche, U. Zimmerman and J. L. Martinez, *A combined studies of the magnetic properties of $GdCrO_4$* , J. Phys.: Condens. Matt., **18**, p7893 (2006).

25. E. Climent, J.M. Gallardo, J. Romero de Paz, N. Taira, R.S. Puche, *Phase transition induced by pressure in TbCrO₄ oxide: Relationship structure-properties*, J. Alloys Compd., **488**, p524 (2009).
26. Y. Long, Q. Liu, Y. Lv, R. Yu, C. Jin, *Various 3d-4 f spin interactions and field-induced metamagnetism in the Cr⁵⁺ system DyCrO₄*, Phys. Rev. B, **83**, p024416 (2011).
27. Y.W. Long, L.X. Yang, Y. Yu, F.Y. Li, R.C. Yu, and C.Q. Jin, *Synthesis, structure, magnetism and specific heat of YCrO₄ and its zircon-to-scheelite phase Transition*, Phys.Rev.B., **75**, p104402 (2007)
28. L.B. McCusker, R.B. Von Dreele, D.E Cox, D. Louer, and P.Scaldi, *Rietveld refinement guidelines*, J. Appl. Cryst., **32**, p36 (1999).
29. B. D. Cullity, *Elements of X-ray diffraction*, 2nd Ed., Addison-Wesley Publishing Co. Inc., p189-226 (1978).

Chapter 4

Magnetic properties of Rare earth Chromate Nanoparticles

4.1 Introduction

RCrO_4 belongs to a family of compounds where the Chromium is stabilized in an unusual oxidation state of +5 [1, 2]. As described in the previous chapters, RCrO_4 crystallizes into tetragonal structure with space groups $I41/amd$ (No. 141, $Z=4$ with crystal symmetry D_{4h}^{19}) and/or $I41/a$ (No. 88, $Z=4$ with crystal symmetry C_{4h}^6) referred as zircon and scheelite phases respectively [3,4]. The two phases are inter-convertible into one another at appropriate temperature and/or pressure conditions. The rare – earth ion, R^{3+} ($4f^{1-14}$) is located in an eight-coordinated RO_8 triangular dodecahedra while the chromium ion, Cr^{5+} ($4s^1 3d^0$) in distorted CrO_4 tetrahedra. In RCrO_4 , Cr exists in paramagnetic Cr^{5+} state that orders ferromagnetically with Curie temperature, $T_C \sim 10$ K in the presence of non-magnetic rare earth, as shown in YCrO_4 [5]. When R is magnetic, rare- earth orders antiferromagnetically with $T_N < 20$ K. Depending on the anisotropy of the R, the ground state of RCrO_4 is either ferromagnetic or antiferromagnetic. It has been reported that the magnetic structure of RCrO_4 with $\text{R} = \text{Nd} - \text{Yb}$ is described as ferromagnetic and $\text{R} = \text{Sm}$, Eu and Lu are shown to be antiferromagnetic [6, 7]. Moreover, it has been reported the magnetic behaviour of these compounds is field- dependent [8]. When the ferromagnetic and antiferromagnetic exchange interactions are comparable, a field- induced metamagnetism is observed in RCrO_4 with $\text{R} = \text{Ho}$, Gd and Lu . This is due to the strong competition between the super exchange interactions of ferromagnetic $3d$ spins of Cr^{5+} ions and antiferromagnetic $4f$ spins of R^{3+} ions [9]. Thus the complicated magnetic

structure of RCrO_4 requires an attention to study. The XRD analysis reveals that the RCrO_4 nanoparticles synthesized in the present piece of work belong to zircon- type RCrO_4 . Henceforth, the magnetic properties of zircon-type RCrO_4 nanoparticles are discussed in the following sections.

4.2 Magnetic Properties of RCrO_4 nanoparticles

DC Magnetic measurements on RCrO_4 ($\text{R} = \text{Sm, Gd, Dy and Er}$) nanoparticles were carried out with a vibrating sample magnetometer in a Physical Property Measurement System (PPMS) using stable mode option.

4.2.1 Magnetization (M) vs. Temperature (T) Measurements

Zero-Field Cooled (ZFC) and Field- Cooled (FC) magnetization measurements on rare earth chromates, RCrO_4 ($\text{R} = \text{Sm, Gd, Dy and Er}$) nanoparticles were carried out in the presence of an external magnetic field, $H = 100$ Oe in the temperature range $2.5 \text{ K} \leq T \leq 350 \text{ K}$. Figure 1 shows the ZFC and FC magnetization of SmCrO_4 nanoparticles. It reveals the ZFC and FC magnetization data smoothly overlap on one another with decreasing temperature from 300 K to nearly 100 K. Though the ZFC and FC are apparently found to be bifurcating at ~ 100 K, It has been observed that the magnetization (both ZFC and FC) data exhibit a magnetic transition at 12 K, as shown in the inset of figure 1. This transition may be referred as paramagnetic (PM) to ferromagnetic transition and the transition temperature is referred as Curie temperature, T_C . It is observed that, ZFC and FC magnetization increase below 12 K. The FC magnetization of SmCrO_4 nanoparticles measured at 2.5 K is 7.7×10^{-3} emu/gm. Figure 2 shows the ZFC and FC magnetization of GdCrO_4 nanoparticles.

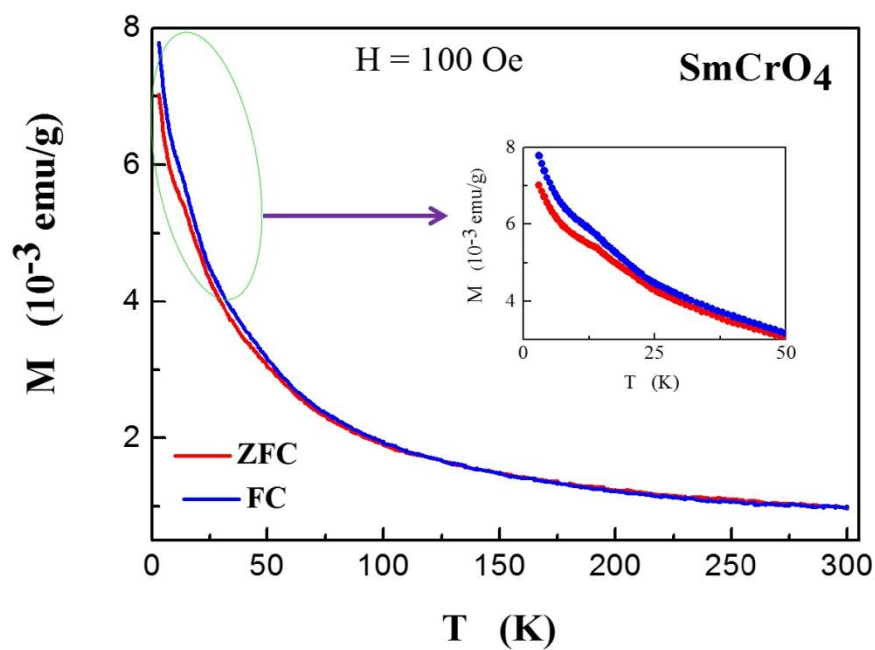


Fig. 1. Zero-Field Cooled (ZFC) and Field-Cooled (FC) Magnetization of SmCrO_4 .

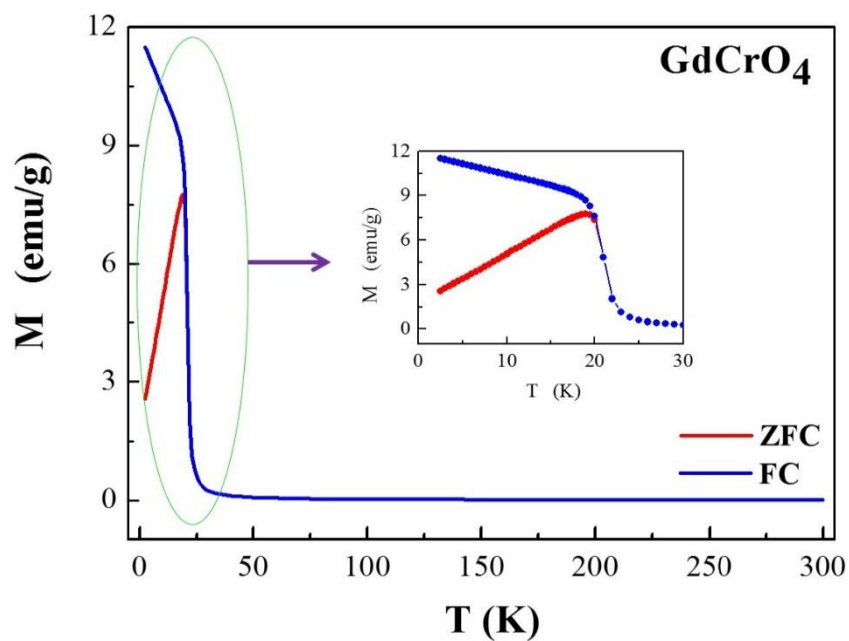


Fig. 2. Zero-Field Cooled (ZFC) and Field-Cooled (FC) Magnetization of GdCrO_4 .

It reveals the ZFC and FC magnetization data smoothly overlap on one another with decreasing temperature from 300 K to nearly 25 K. Below 25 K, The ZFC and FC magnetization data increases before the bifurcation is observed at 21 K, marked as transition temperature, T_C , as shown in the inset of figure 2. Further decrease in temperature decreases the ZFC magnetization and increases the FC magnetization. The FC magnetization of GdCrO₄ nanoparticles measured at 2.5 K is 11.5 emu/gm. Figure 3 shows the ZFC and FC magnetization of DyCrO₄ nanoparticles. It reveals the ZFC and FC magnetization data smoothly overlap on one another with decreasing temperature from 300 K to nearly 25 K. Below 22 K, The ZFC and FC magnetization data increase before the bifurcation is observed at 22 K, noticed as Curie temperature, T_C , as shown in the inset of figure 3. Further decrease in temperature decreases the ZFC magnetization and increases the FC magnetization. The FC magnetization of DyCrO₄ nanoparticles measured at 2.5 K is 17.7 emu/gm. Figure 4 shows the ZFC and FC magnetization of ErCrO₄ nanoparticles. It reveals the ZFC and FC magnetization data smoothly overlap on one another with decreasing temperature from 300 K to nearly 20 K. Below 20 K, The ZFC and FC magnetization data increase before the bifurcation is observed at 16 K, perceived as transition temperature, T_C , as shown in the inset of figure 4. Further decrease in temperature decreases the ZFC magnetization and increases the FC magnetization. The FC magnetization of ErCrO₄ nanoparticles measured at 2.5 K is 6.3 emu/gm. The observed transition temperatures for RCrO₄ are found to decrease with increase in the atomic number of the rare earth. Moreover, the M-T gives a direct measurement for the blocking temperature distribution.

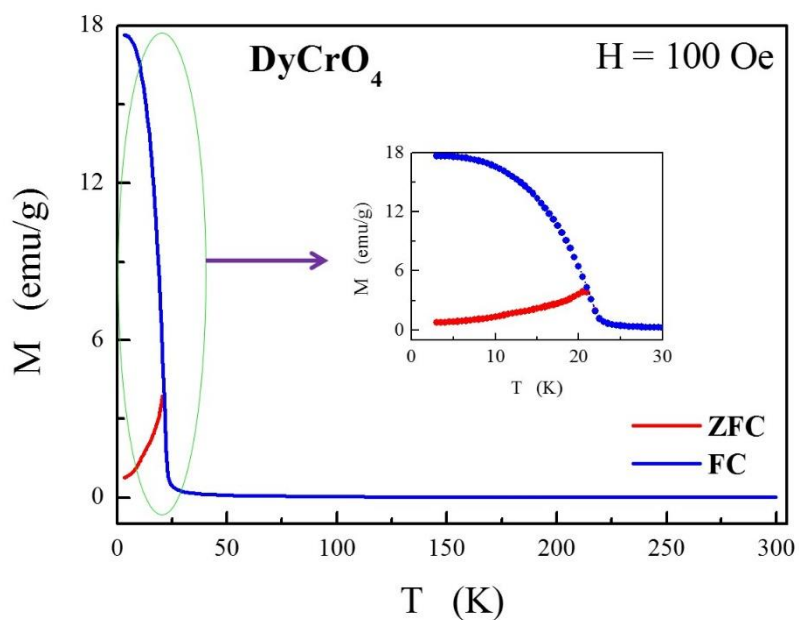


Fig. 3. Zero-Field Cooled (ZFC) and Field-Cooled (FC) Magnetization of DyCrO_4 .

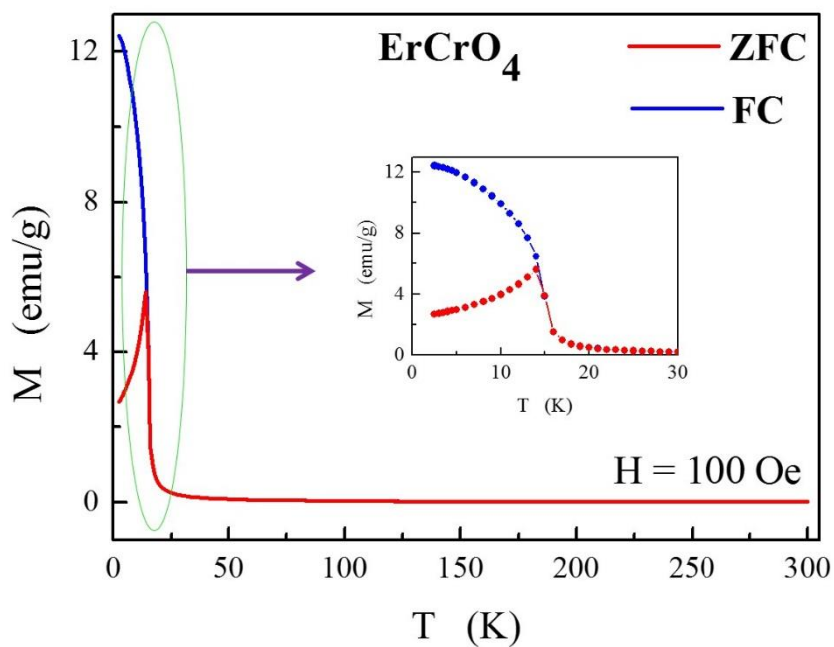


Fig. 4. Zero-Field Cooled (ZFC) and Field-Cooled (FC) Magnetization of ErCrO_4 .

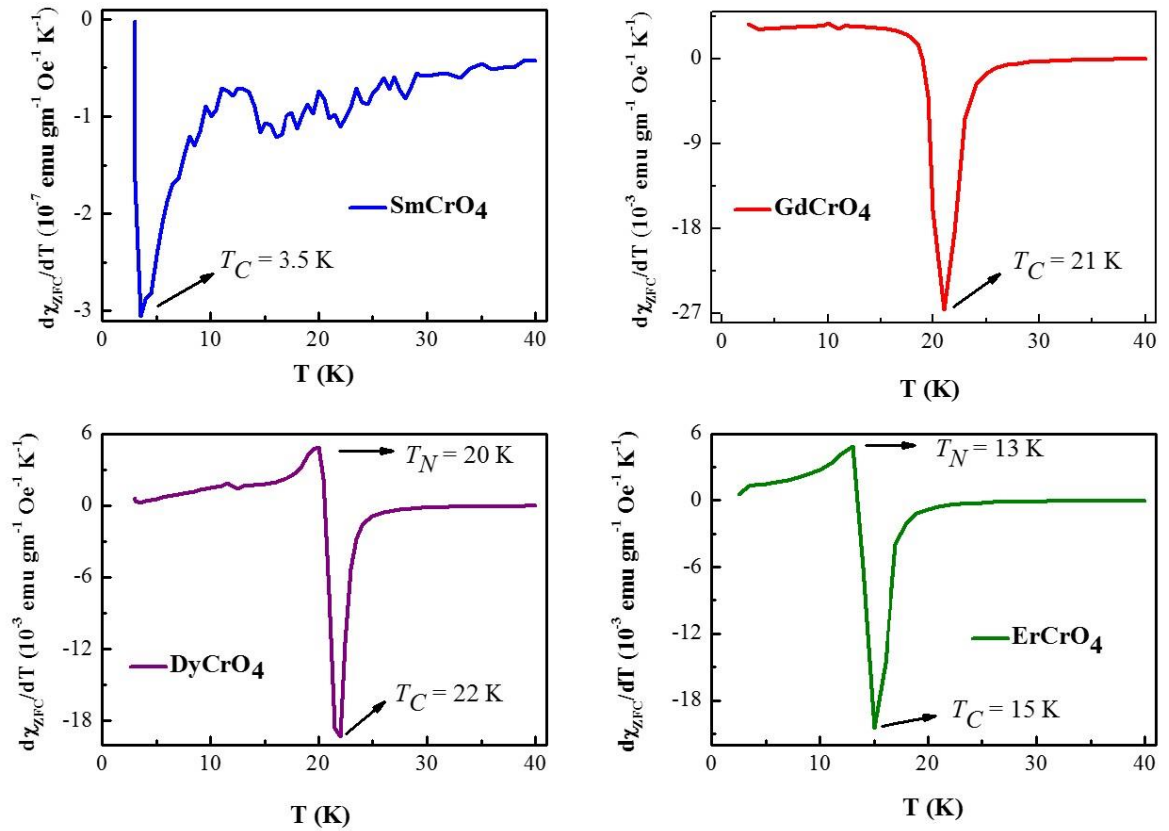


Fig. 5. Derivative of Zero-Field Cooled (ZFC) Magnetization of $R\text{CrO}_4$ nanoparticles.

However, the transition temperatures observed from M-T plots are the net outcome of ferromagnetic ordering of Cr^{5+} ions and antiferromagnetic ordering of magnetic R^{3+} ions. The former ordering results in Curie temperature, T_C and later gives Néel temperature, T_N . In the present study, the FM Curie temperature (T_C) and AFM Néel temperature (T_N) for $R\text{CrO}_4$ nanoparticles have been obtained from the temperature (T) vs. derivative of ZFC magnetization plots, as shown in figure 5. It reveals that ferromagnetic interactions of Cr^{5+} dominate over antiferromagnetic interactions in GdCrO_4 nanoparticles with a $T_C = 21$ K. However, competing Cr^{5+} ferromagnetic and R^{3+} antiferromagnetic interactions exist in DyCrO_4 and ErCrO_4 nanoparticles that result in T_C and T_N . The observed values of T_C and T_N for DyCrO_4 are 22 and 20 K respectively. The observed values of T_C and T_N for ErCrO_4

are 15 and 13 K respectively. Similar analysis for SmCrO_4 results in a Curie temperature, $T_C = 3.5$ K. However, such T_C may not be accounted due to extremely low values of $d\chi_{ZFC}$ (of the order of 10^{-7} emu gm^{-1} Oe^{-1} K^{-1}).

4.2.2 Curie-Weiss Analysis

Temperature (T) versus field-cooled inverse susceptibility (χ^{-1}) graphs have been plotted to understand and analyze the dominant magnetic behavior of RCrO_4 nanoparticles below the transition temperature. The plots are expected to be linear in the paramagnetic regime, known to be Curie-Weiss (C-W) plots. Figure 6 shows the T vs χ^{-1} plots for SmCrO_4 , GdCrO_4 , DyCrO_4 and ErCrO_4 nanoparticles respectively. The figure reveals the non-linear C-W behavior of RCrO_4 nanoparticles. It is more evident from the T vs χ^{-1} plot for SmCrO_4 . The deviation of χ^{-1} of RCrO_4 from Curie-Weiss behavior is due to the spacing of the multiplet levels of R^{3+} is not compared to kT thus making the some of the R^{3+} ions in excited states, as suggested by Van Vleck and Frank [10,11]. In particular, due to the population of the non-magnetic ground term 7F_0 of Sm^{3+} the χ of Sm^{3+} is overshadowed by the χ of Cr^{5+} . This leads to the sole contribution of χ due to paramagnetic Cr^{5+} in SmCrO_3 [11]. Since χ is greater than that given by Hund's equation, and J is small compared to S and L for Sm^{3+} , the susceptibility involves the $\alpha(J)$ term that makes a flat χ at low temperatures. This gives a non-linear behavior to χ^{-1} of SmCrO_4 nanoparticles and makes it different from C-W law, observed for Sm^{3+} compounds [11]. Similar observation has been reported in EuCrO_4 [10, 12]. Hence the non-linear T vs χ^{-1} plots of RCrO_4 nanoparticles have been analyzed by using the modified Curie-Weiss equation given by [10, 11]

$$\chi^{-1} = \left[\left(\frac{C_{cw}}{T - \theta_{cw}} \right) + \chi^* \right]^{-1} \quad \dots (1)$$

Where C_{cw} = Curie-Weiss constant and θ_{cw} = Curie-Weiss temperature. In figure 6, the open black circles denote the T vs. χ^{-1} data and the solid red line represents the modified Curie-Weiss fits. The obtained values of C_{cw} and θ_{cw} are fed to obtain the effective magnetic moment, μ_{eff} of RCrO_4 nanoparticles by using the formula

$$\mu_{eff} = \left[\frac{3\kappa_{\beta} C_{cw}}{N\mu_{\beta}^2} \right]^{1/2} \quad \dots (2)$$

Where, χ = susceptibility

κ_{β} – Boltzman's constant

N – avogadro's number

μ_{β} – Bohr magnetron

C_{cw} – curie constant

The values of Curie-Weiss constant, C_{cw} , Curie-Weiss temperature, θ_{cw} , obtained from modified C-W fit and calculated μ_{eff} for RCrO_4 nanoparticles are given in Table 1. The positive value of θ_{cw} of SmCrO_4 indicates the dominance of ferromagnetic (FM) interaction over antiferromagnetic (AFM) interaction in the magnetic ground state. A negative of θ_{cw} obtained for GdCrO_4 , DyCrO_4 and ErCrO_4 indicates the presence of AFM interactions at low temperatures. The high value of θ_{cw} obtained for SmCrO_4 may be attributed to the possible existence of short- range ordering. The obtained effective magnetic moments, μ_{eff} for RCrO_4 nanoparticles are in accordance with the literature [1–7].

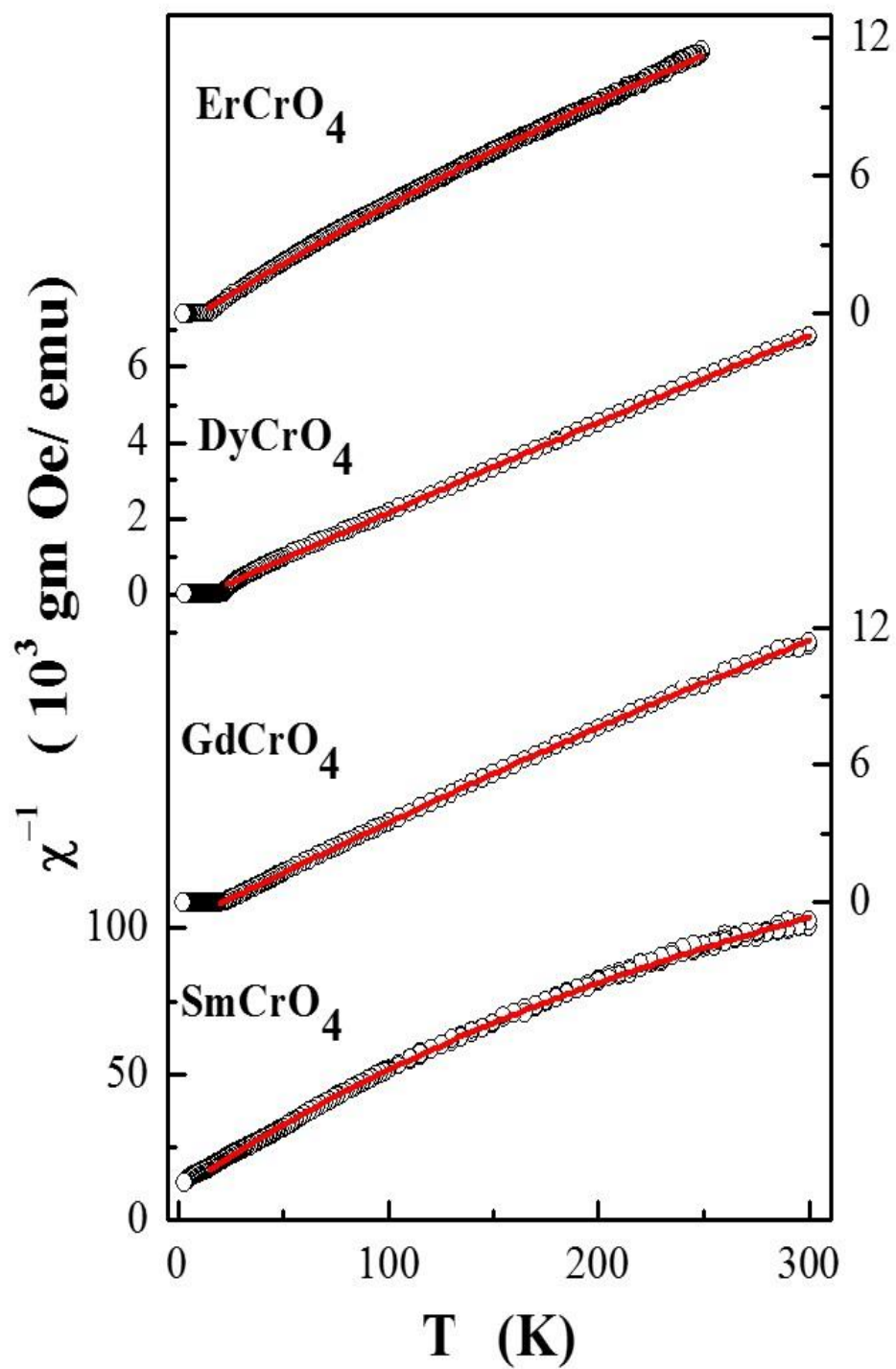


Fig. 6. Curie-Weiss fits of $R\text{CrO}_4$ nanoparticles.

Table 1: Curie -Weiss constant, C_{CW} , Curie-Weiss temperature, θ_{CW} , and calculated effective magnetic moment (μ_{eff}) for $R\text{CrO}_4$ nanoparticles.

Sl. No.	$R\text{CrO}_4$	Curie's Constant(C)	Curie-Weiss Temperature (θ_{CW})	Effective magnetic moment, μ_{eff} (μ_B)
1	SmCrO_4	0.00261	+32.66	2.36
2	GdCrO_4	0.02462	-14.59	7.34
3	DyCrO_4	0.04180	-11.55	9.65
4	ErCrO_4	0.02131	-2.75	6.95

4.2.3 Magnetization (M) vs. Magnetic Field (H) Measurements

Magnetization versus external magnetic field measurements (M-H curves) have been carried out on $R\text{CrO}_4$ ($R = \text{Sm, Gd, Dy and Er}$) nanoparticles in the field range -9 to +9 T at 5 K and 300 K. The M-H curves recorded on $R\text{CrO}_4$ nanoparticles at 320 K are found to be linear and indicate the paramagnetic nature of the samples, as shown in figure 7. Figures 8–11 shows the M-H curves recorded on $R\text{CrO}_4$ nanoparticles at 5 K in the field range -1 to +1 T. The insets of figures 8–11 shows the same measurements in the field range -9 to +9 T. The nearly linear behavior with zero hysteresis show the antiferromagnetic interactions exist in SmCrO_4 . The presence of hysteresis $H_c = 137, 2284$ and 414 Oe respectively reveal the presence of weak ferromagnetic R-O-Cr-O-R exchange coupling in $\text{GdCrO}_4, \text{DyCrO}_4, \text{ErCrO}_4$. At high fields, the magnetization of $\text{DyCrO}_4, \text{ErCrO}_4$ varies linearly with external field. The extrapolation of the plot to zero-field gives the ferromagnetic component with $M_z = 110$ and 100 emu/gm respectively for $\text{DyCrO}_4, \text{ErCrO}_4$.

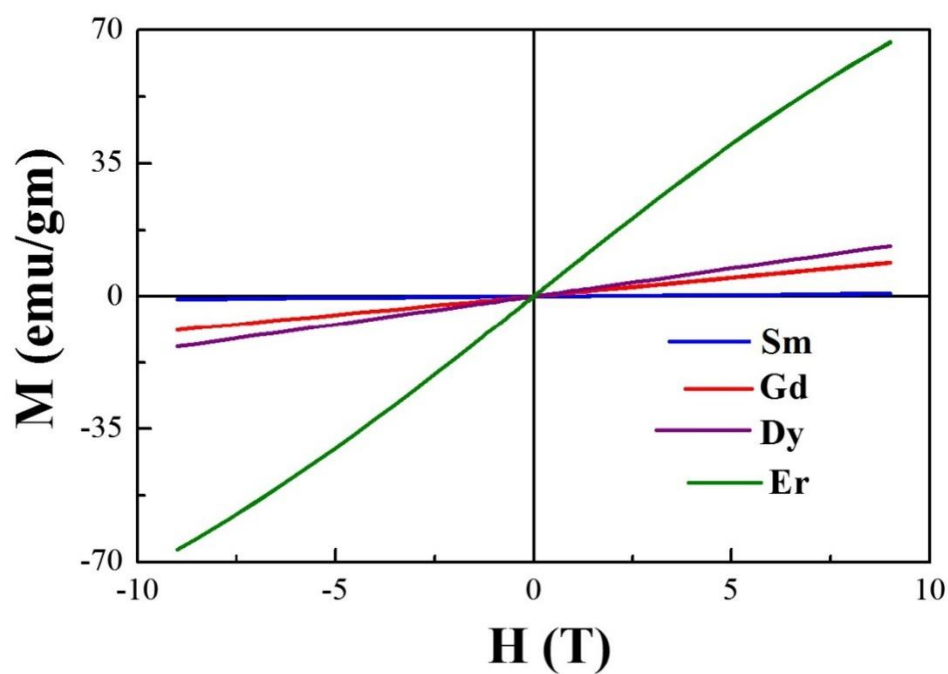


Fig. 7. M - H curve of RCrO_4 recorded at 300 K (in PM regime) in the range $H = -9$ T to $+9$ T.

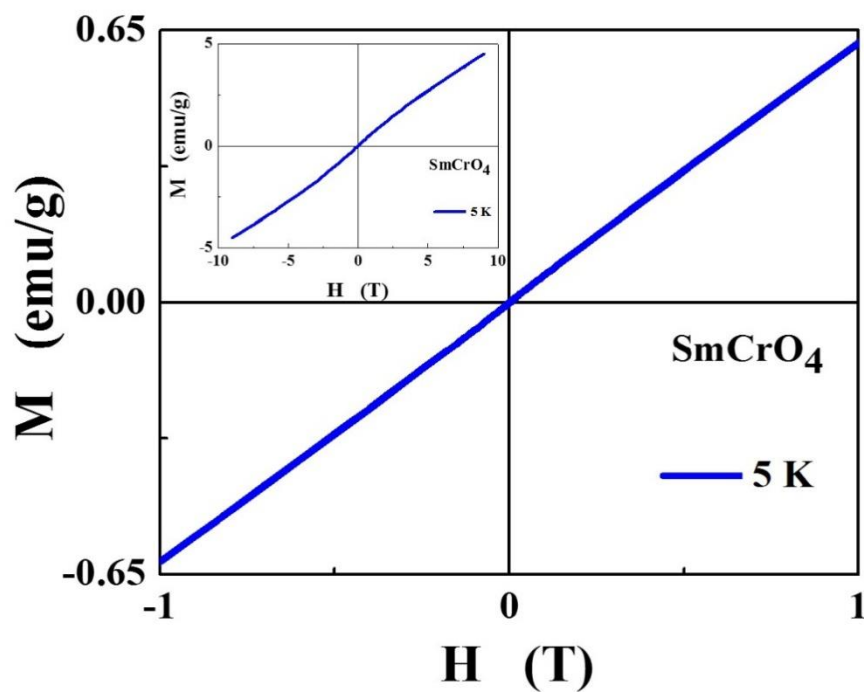


Fig. 8. M - H curve of SmCrO_4 nanoparticles recorded at 5 K.
The inset shows the curves in the range $H = -9$ T to $+9$ T.

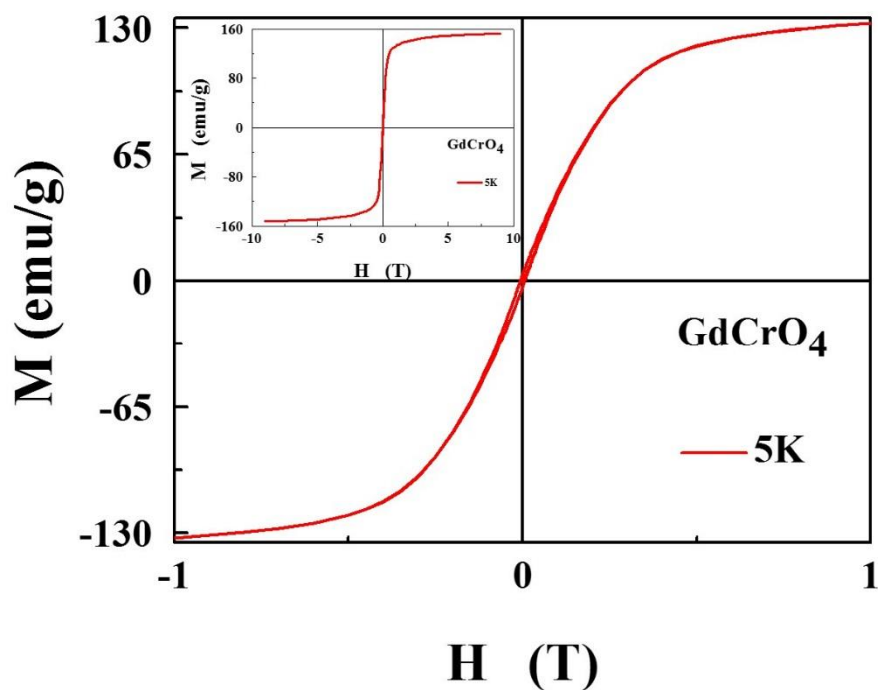


Fig. 9. M - H curve of GdCrO_4 nanoparticles recorded at 5 K.

The inset shows the curves in the range $H = -9 \text{ T}$ to $+9 \text{ T}$.

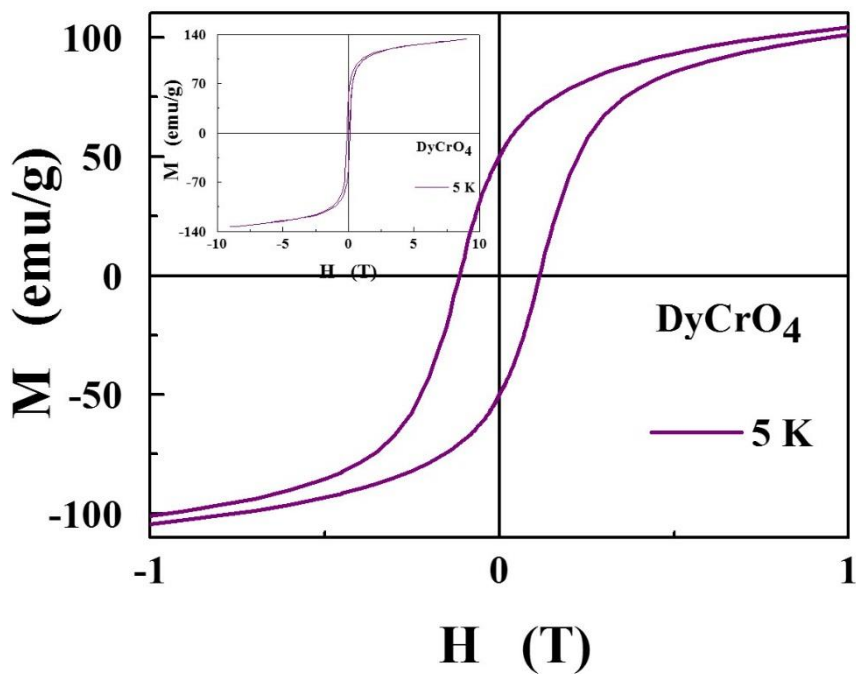


Fig. 10. M - H curve of DyCrO_4 nanoparticles recorded at 5 K.

The inset shows the curves in the range $H = -9 \text{ T}$ to $+9 \text{ T}$.

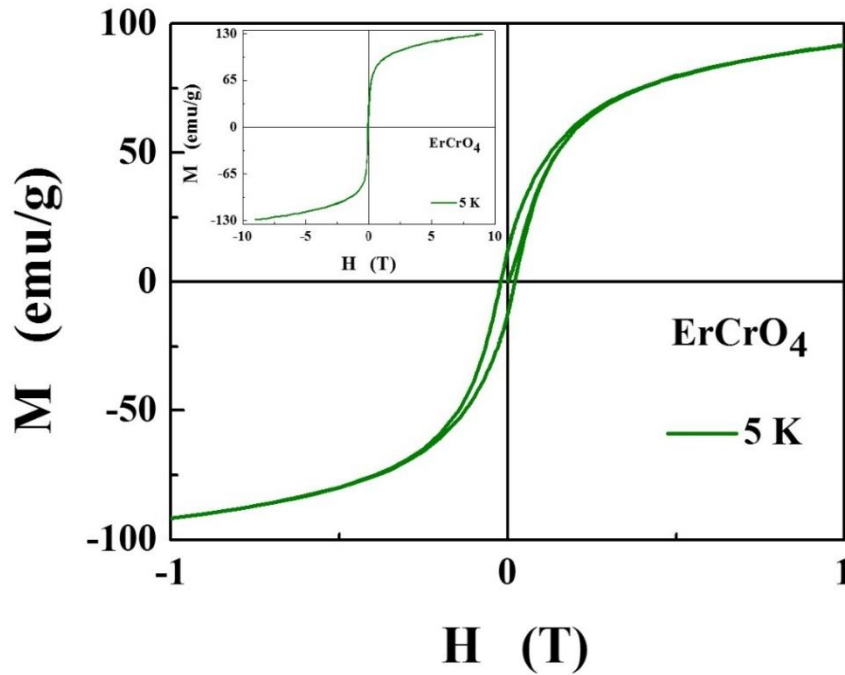


Fig. 11. M - H curve of ErCrO_4 nanoparticles recorded at 5 K.

The inset shows the curves in the range $H = -9 \text{ T}$ to $+9 \text{ T}$.

However, the magnetization of GdCrO_4 was found to saturate at high fields with $M_z = 152$ emu/gm. Since Cr^{5+} is nonmagnetic, the contribution to the measured magnetic moment is expected to be solely from the rare earth, R^{3+} . Similar to SmCrO_4 , the nearly linear M - H plot reveals the presence of antiferromagnetic interactions in SmCrO_3 .

4.3 Conclusions

The DC Magnetization measurements on the RCrO_4 ($\text{R} = \text{Sm}, \text{Gd}, \text{Dy}$ and Er) nanoparticles exhibit magnetic transition temperature as a result of antiferromagnetic ordering of R^{3+} and ferromagnetic ordering of Cr^{5+} ions. The analysis of by $d\chi_{\text{ZFC}}/dT$ curves confirm the

presence of antiferromagnetic ordering of R^{3+} sublattice and ferromagnetic ordering Cr^{5+} sublattice with a closely spaced Néel and Curie temperatures (T_N and T_C) at low temperatures. The presence of a non-zero hysteresis and unsaturation of spontaneous magnetization at high fields observed in M-H curves validate the simultaneous competing antiferromagnetic and ferromagnetic interactions that lead to magnetic frustration in RCrO_4 with a ferromagnetic ground state. The non-linear behavior of Curie-Weiss fits confirms the VanVleck contribution due to rare earth ions. The magnetic moment per formula unit estimated from modified Curie-Weiss fits are accounted for Cr^{5+} moments along with R^{3+} moment in RCrO_4 nanoparticles respectively and found to be in accordance with the literature.

References

1. E. Jiménez, J. Isasi, M.T. Fernández, R. Sáez-Puche, *Magnetic behaviour of ErCrO_4 oxide*, J. Alloys Comp., **344**, p369 (2002).
2. R.S. Puche, E. Climent, M.G. Rabie, J. Romero, and J.M. Gallardo, *Neutron diffraction characterization and magnetic properties of the scheelite-type ErCrO_4 polymorph*, J.Phys.:Conf. Series, **325**, p012012 (2011).
3. E.J. Melero, P.C.M. Gubbens, M.P. Steenvoorden, S. Sakarya, A. Goosens, P.D.D. Reotier, A. Yaouanc, J.R. Carvajal, B. Beuneu, J. Isasi, R.S. Puche, U. Zimmerman and J. L. Martinez, *A combined studies of the magnetic properties of GdCrO_4* , J. Phys.: Condens. Matt., **18**, p7893 (2006).
4. Y. Long, Q. Liu, Y. Lv, R. Yu, C. Jin, *Various 3d-4 f spin interactions and field-induced metamagnetism in the Cr^{5+} system DyCrO_4* , Phys. Rev. B, **83**, p024416 (2011).
5. Y.W. Long, L.X. Yang, Y. Yu, F.Y. Li, R.C. Yu, and C.Q. Jin, *Synthesis, structure, magnetism and specific heat of YCrO_4 and its zircon-to-scheelite phase Transition*, Phys.Rev.B, **75**, p104402 (2007).
6. H. Walter, H.G. Kahle, K. Mulder, H.C. Schopper, H. Schwarz, *Magnetic phase transitions in rare earth chromates*, Int.J.Magn., **5**, p129 (1973).
7. E. Jiménez, J. Isasi, R. S. Puche, *Synthesis, Structural characterization and magnetic properties of $R\text{CrO}_4$ oxides, $R = \text{Nd}, \text{Sm}, \text{Eu}$ and Lu* , J. Alloys Comp., **312**, p53 (2000).
8. E. Jiménez, J. Isasi, R.S. Puche, *Structural and Magnetic Characterization of Zircon-Type PrCrO_4 Oxide*, J. Alloys Comp., **323**, p115 (2001).

9. A. Midya, N. Khan, D. Bhoi and P. Mandal, *3d-4f spin interaction and field-induced metamagnetism in $RCrO_4$ ($R = Ho, Gd, Lu$) compounds*, J. Appl. Phys., **115**, p17E114 (2014).
10. J.H. Van Vleck, *Theory of Electric and Magnetic Susceptibilities*, Oxford University Press, p86 (1965).
11. A.H. Morrish, *The Physical Principles of Magnetism*, Wiley-IEEE Press, p46, New York (2001).
12. A. M. Sánchez, F. Fernández and R.S. Puche, *Magnetic properties of rare earth chromates $RCrO_4$ ($R=Nd, Sm$ and Eu)*, J. Alloy. Comp., **201**, p161 (1993).

Chapter 5

Magnetic Properties of Rare earth Orthochromite Nanoparticles

5.1 Introduction

Rare earth orthochromites, RCrO_3 (R = rare earth/ Yttrium), are a class of oxides that exhibit unusual magnetic properties due to their electronic correlations [1–5]. As described in earlier chapters, the chromium ions, Cr^{3+} occupy the octahedral B- site while the rare earth ions, R^{3+} occupy nine-coordinated A- site. Due to DM interaction, the Cr^{3+} spins undergo a paramagnetic (PM) to antiferromagnetic transition (AFM) with a canting of spins in the chromium sublattices, forms Γ_4 (G_x, A_y, F_z) magnetic ground state, as reported in YCrO_3 [6–7]. The ground state Γ_4 remains the same and the magnetic property of RCrO_3 ($R = \text{Y, La}$) is solely governed by Chromium unless affected by the presence of a magnetic rare earth. The presence of a magnetic R^{3+} ion brings in magnetic anisotropy that promotes phenomena like negative magnetization, magnetic compensation and spin- reorientation (SR) in RCrO_3 [8–9]. This temperature-dependent $3d-4f$ interaction between magnetic R^{3+} and Cr^{3+} may give rise to Γ_2 (F_x, C_y, G_z) and/or Γ_1 (A_x, G_y, C_z) ground state spin configurations with Γ_1 being the collinear antiferromagnetic spin structure of Cr sublattice [10–11]. This necessitates studying the complex magnetic behavior of RCrO_3 . In addition, the size effects due to the controlled particle growth are expected to alter the magnetic properties of RCrO_3 due to competing sublattice magnetizations. This may be reflected with a change in the transition temperature (T_C or T_N), Compensation temperature (T^*), and spin-reorientation temperature (T_{SR}). In view of such exciting magnetic behavior, we

report the magnetic properties of RCrO_3 ($\text{R} = \text{Sm, Gd, Dy and Er}$) nanoparticles through DC magnetization measurements in the present chapter.

5.2 Magnetic Properties of RCrO_3

DC Magnetic measurements on RCrO_3 ($\text{R} = \text{Sm, Gd, Dy and Er}$) were carried out with a vibrating sample magnetometer in a Physical Property Measurement System (PPMS) using stable mode option.

5.2.1 Magnetization (M) vs. Temperature (T) Measurements

Zero-Field Cooled (ZFC) and Field-Cooled (FC) magnetization measurements on rare earth orthochromites, RCrO_3 ($\text{R} = \text{Sm, Gd, Dy and Er}$) nanoparticles were carried out in the presence of an external magnetic field, $H = 100 \text{ Oe}$ in the temperature range $2.5 \text{ K} \leq T \leq 350 \text{ K}$. Figure 1 shows the ZFC and FC magnetization of SmCrO_3 nanoparticles. It reveals the ZFC and FC magnetization data smoothly overlap on one another with decreasing temperature from 350 K to 198 K. The ZFC and FC magnetization bifurcates at 198 K indicating the paramagnetic (PM) to canted antiferromagnetic (CAFM) transition, marked as Néel temperature, T_N^{Cr} as shown in inset (a) of figure 1. The transition is due to the canting of antiferromagnetically ordered spins at Cr sublattices as a result of antisymmetric Dzyaloshinskii-Moriya interaction [12]. The FC magnetization increases with decrease in temperature at 198 K for SmCrO_3 due to weak ferromagnetic moment that arises due to the canting of Cr^{3+} spins at the Chromium sublattices. Further, the decrease in FC magnetization reveals that SmCrO_3 nanoparticles undergo a spin-reorientation (SR) with spin-reorientation temperature, $T_{\text{SR}} = 80 \text{ K}$, as shown in the inset (b) of figure 1.

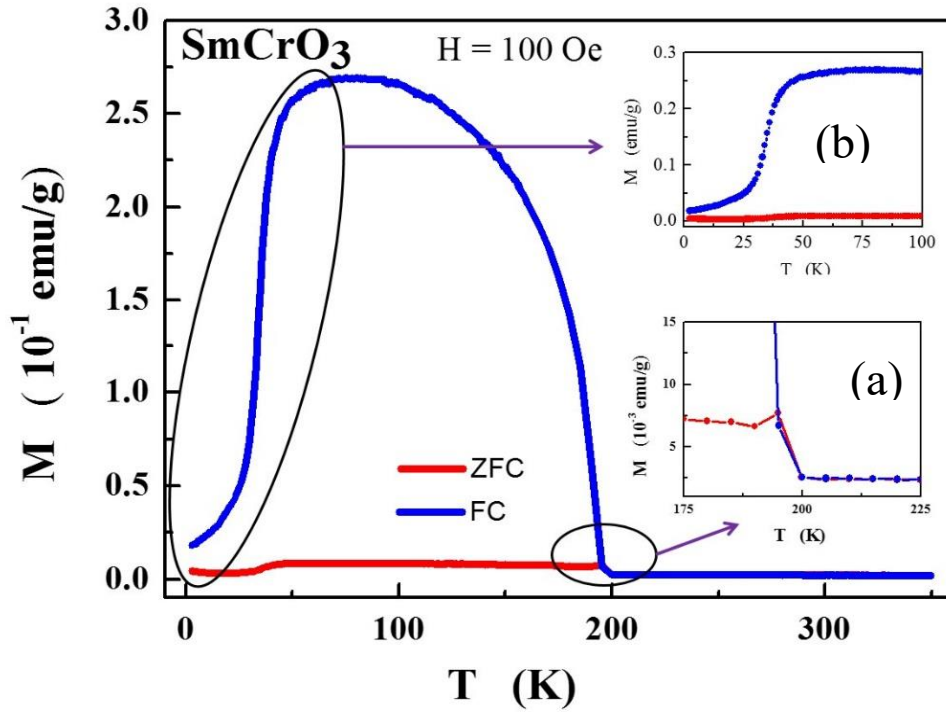


Fig. 1. Zero-Field Cooled (ZFC) Field-Cooled (FC) Magnetization of SmCrO_3 nanoparticles.

Figure 2 shows the ZFC and FC magnetization of GdCrO_3 nanoparticles. It reveals the ZFC and FC magnetization data smoothly overlap on one another with decreasing temperature from 350 K to 168 K. The ZFC and FC magnetization bifurcates at 168 K indicating the PM to CAFM transition, noticed as Néel temperature, T_N^{Cr} as shown in inset (a) of figure 2. However, it is observed that the magnetization of the GdCrO_3 nanoparticles is not analogous to the bulk GdCrO_3 [13]. Both Zero field-cooled and field-cooled magnetization of the GdCrO_3 nanoparticles shows anomalous behavior. Below the T_N^{Cr} ($= 168$ K), the FC increases initially and undergoes a spin-reorientation (SR) with a compensation temperature, $T^* \sim 128$ K, as shown in the insets (a) and (b) of figure 2. Below 128 K, the sample exhibits a negative magnetization and shows further anomalies at 25, 19 and 13 K before it shoots up to attain saturation value 2.69 emu/gm at 2.5 K. This

is due to the competition between the sub-lattice magnetization of Chromium and Gadolinium sub-lattices, and is expected in oxide materials.

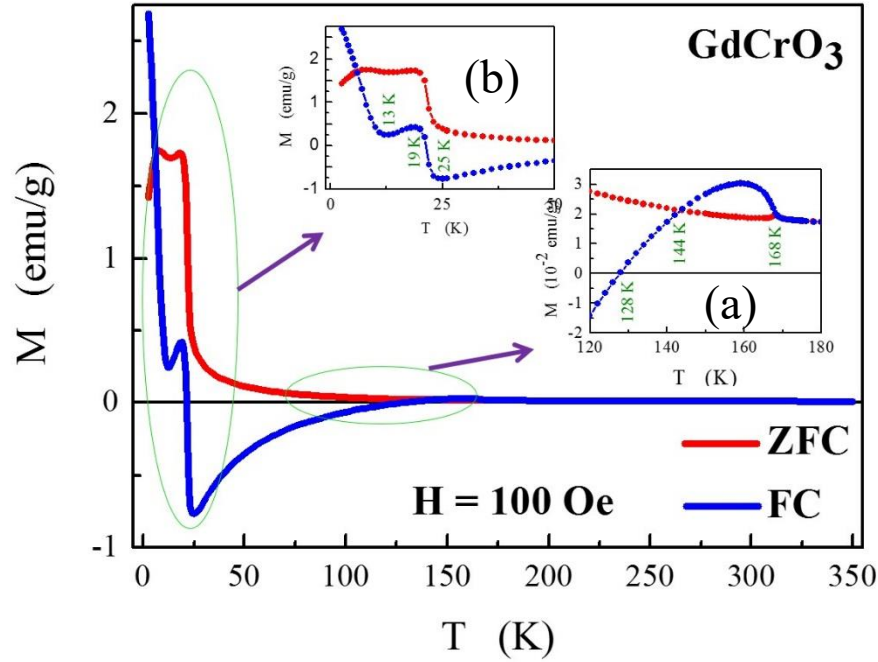


Fig. 2. Zero-Field Cooled (ZFC) Field-Cooled (FC) Magnetization of GdCrO_3 nanoparticles.

Figure 3 shows the ZFC and FC magnetization of DyCrO_3 nanoparticles. It reveals the ZFC and FC magnetization data smoothly overlap on one another with decreasing temperature from 350 K to 143 K. The ZFC and FC magnetization bifurcates at 143 K indicating the PM to CAFM transition, observed as Néel temperature, T_N^{Cr} as shown in inset (a) of figure 3. Below the Néel temperature, $T_N^{\text{Cr}} = 143$ K, the FC magnetization increases with decreasing temperature and DyCrO_3 nanoparticles undergoes a spin-reorientation at $T_{\text{SR}} \sim 5$ K, as shown in inset (b) of figure 3. Below T_{SR} , the FC magnetization drops rapidly to nearly zero emu/gm.

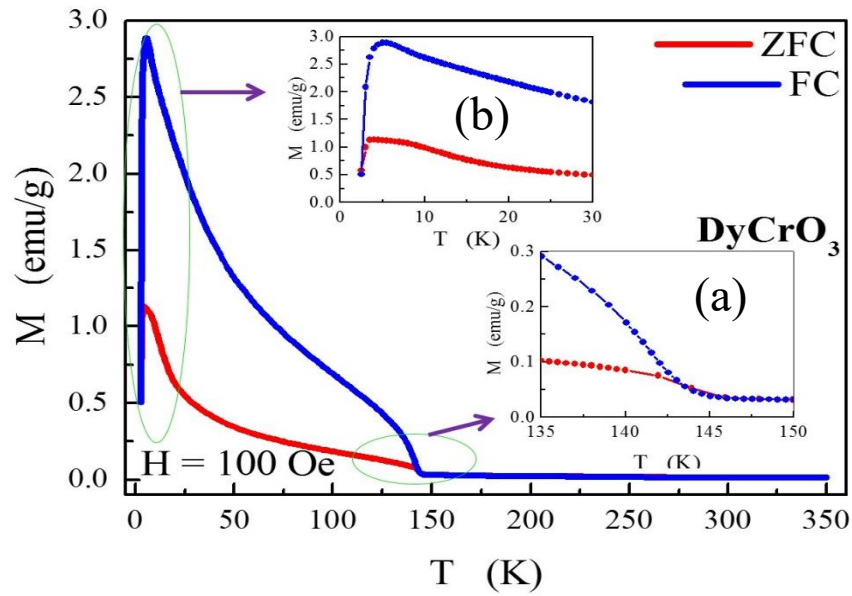


Fig. 3. Zero-Field Cooled (ZFC) Field-Cooled (FC) Magnetization of DyCrO_3 nanoparticles.

Figure 4 shows the ZFC and FC magnetization of ErCrO_3 nanoparticles. It reveals the ZFC and FC magnetization data smoothly overlap on one another with decreasing temperature from 350 K to 143 K. The ZFC and FC magnetization bifurcates at 133 K indicating the PM to CAFM transition, perceived as Néel temperature, T_N^{Cr} as shown in inset (a) of figure 4. Below the Néel temperature, $T_N^{\text{Cr}} = 133$ K, the FC magnetization increases with decreasing temperature and ErCrO_3 nanoparticles undergoes a spin-reorientation at $T_{\text{SR}} \sim 16$ K, as shown in inset (b) of figure 4. Below T_{SR} , the FC magnetization drops to nearly zero emu/gm. The observed Néel temperatures for RCrO_3 nanoparticles are found to decrease with increase in the atomic number of the rare earth. It is to be noted that the observed value of T_N^{Cr} for RCrO_3 nanoparticles matches with the literature and confirms size effects do not play a role in altering the Néel temperature [8, 9 and 14].

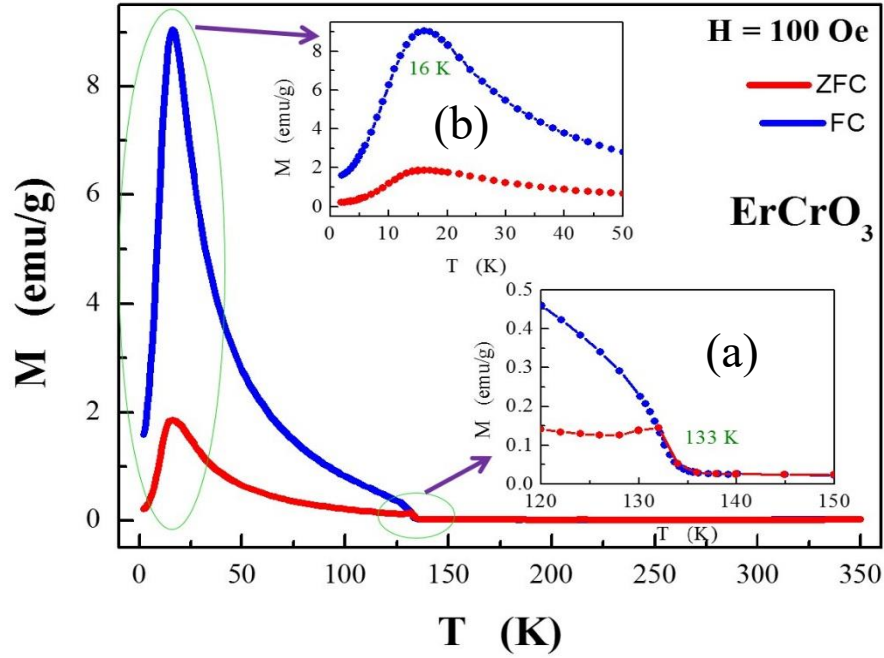


Fig. 4. Zero-Field Cooled (ZFC) Field-Cooled (FC) Magnetization of ErCrO_3 nanoparticles.

Temperature (T) vs. derivative of ZFC magnetization ($d\chi_{\text{ZFC}}/dT$) curves of $R\text{CrO}_3$ (R = Sm, Gd, Dy and Er) nanoparticles are plotted to confirm the Néel temperature (T_N^{Cr}) obtained from M-T measurements, as shown in Figure 5 (a–d). Since a weak ferromagnetic moment exists in $R\text{CrO}_3$ below T_N^{Cr} due to the canted antiferromagnetic coupling of the Cr^{3+} spins, the peak values on the negative side of ($d\chi_{\text{ZFC}}/dT$) are taken to be T_N^{Cr} , against the procedure adopted in chapter 4. The obtained values of Néel temperature T_N^{Cr} are 200, 169, 144 and 133 K respectively for SmCrO_3 , GdCrO_3 , DyCrO_3 and ErCrO_3 as depicted in figure 5 (a – d).

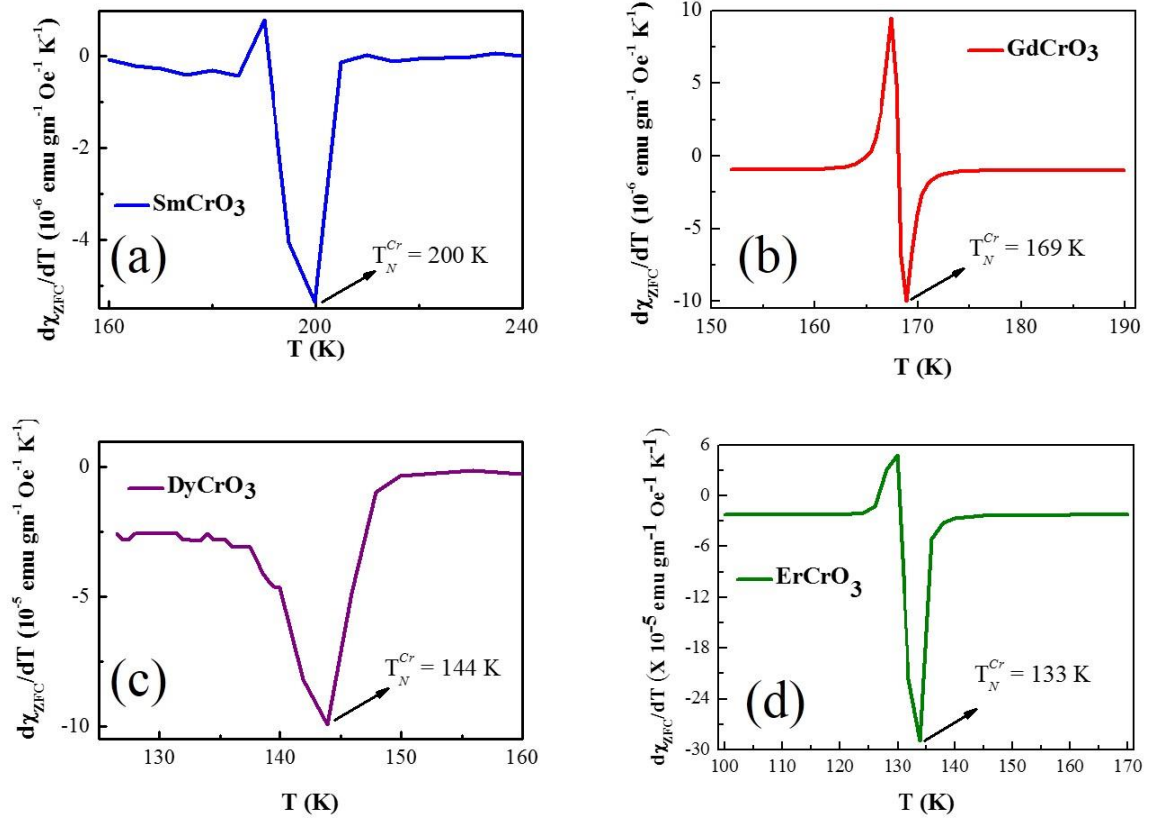


Fig. 5. Derivative of Zero-Field Cooled (ZFC) Magnetization of $R\text{CrO}_3$ nanoparticles.

5.2.2 Curie -Weiss Analysis

Temperature (T) versus field- cooled inverse susceptibility (χ^{-1}) graphs have been plotted to understand and analyze the dominant magnetic behavior of $R\text{CrO}_3$ nanoparticles below Néel temperature, T_N^{Cr} . The plots are expected to be linear in the paramagnetic regime, known to be Curie- Weiss (C-W) plots. Figure 6 shows the T vs. χ^{-1} plots for SmCrO_3 , GdCrO_3 , and DyCrO_3 and ErCrO_3 nanoparticles respectively.

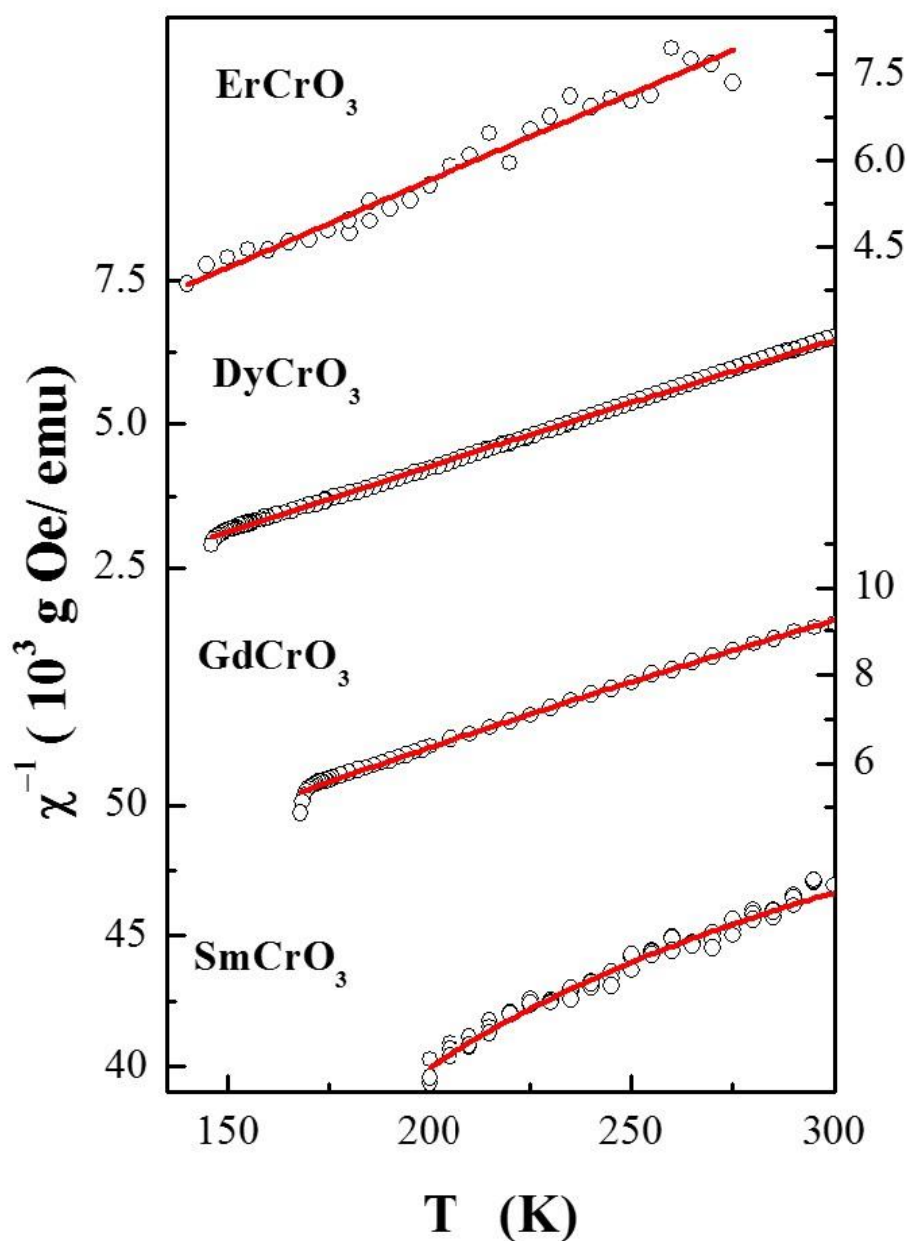


Fig. 6. Modified Curie-Weiss fits of $R\text{CrO}_3$ nanoparticles.

It is observed that the $R\text{CrO}_3$ nanoparticles do not exhibit C- W behavior, i.e. linear behavior. It is more evident from the T vs χ^{-1} plots for SmCrO_3 . The deviation of χ^{-1} of $R\text{CrO}_3$ from Curie-Weiss behavior is due to the spacing of the multiplet levels of R^{3+} is

not compared to kT thus making some of the R^{3+} ions in excited states, as suggested by Van Vleck and Frank [15, 16]. In particular, due to the population of the non-magnetic ground term $^7\text{F}_0$ of Sm^{3+} , the χ of Sm^{3+} is overshadowed by the χ of Cr^{3+} . This leads to the sole contribution of χ due to paramagnetic Cr^{3+} in SmCrO_3 [15–17]. Similar observation may be made in EuCrO_3 . Since χ is greater than that given by Hund equation, and J is small compared to S and L for Sm^{3+} , the susceptibility involves the $\alpha(J)$ term that makes a flat χ at low temperatures. This gives a non-linear behavior to χ^{-1} of SmCrO_3 nanoparticles and makes it different from C-W law, observed for Sm^{3+} compounds. Similar observation has been made in RCrO_4 nanoparticles, as explained in the previous chapter [17].

Hence the non-linear T vs χ^{-1} plots of RCrO_3 nanoparticles have been analyzed by using the modified Curie-Weiss equation given by [18]

$$\chi^{-1} = \left[\left(\frac{C_{cw}}{T - \theta_{cw}} \right) + \chi^* \right]^{-1} \quad \dots (1)$$

Where C_w = Curie-Weiss constant and θ_w = Curie-Weiss temperature. In figure 5, the open black circles denote the data and the solid red line represents the modified Curie- Weiss fits. The obtained values of C_{cw} and θ_{cw} are fed to obtain the effective magnetic moment, μ_{eff} of RCrO_3 nanoparticles by using the formula

$$\mu_{eff} = \left[\frac{3\kappa_{\beta} C_{cw}}{N\mu_{\beta}^2} \right]^{1/2} \quad \dots (2)$$

Where, χ = susceptibility

κ_{β} – Boltzmann's constant

N – Avogadro's number

μ_B – Bohr magnetron

C_{cw} – curie constant

The values of Curie-Weiss constant, C_{cw} , Curie-Weiss temperature, θ_{cw} , obtained from modified C-W fit and calculated μ_{eff} for $R\text{CrO}_3$ nanoparticles are given in Table 1. From the table, it is evident that the positive value of θ_{cw} for SmCrO_3 and GdCrO_3 nanoparticles indicates the dominant weak-ferromagnetic (WFM) interactions over antiferromagnetic interactions with possible existence of Γ_2 (F_x , C_y , G_z) phase ground state. The high value of θ_{cw} obtained for SmCrO_3 may be attributed to the possible existence of short-range ordering. It immediately follows that chromium ions do not exist in collinear magnetic ground state. The negative values of θ_{cw} for DyCrO_3 and ErCrO_3 nanoparticles demonstrate the dominance of AFM interactions and confirms the possible existence of Γ_1 (A_x , G_y , C_z) phase ground state. The μ_{eff} for $R\text{CrO}_3$ nanoparticles are in accordance with the literature for bulk $R\text{CrO}_3$ [19].

Table 1: Curie-Weiss constant, C_{cw} , Curie-Weiss temperature, θ_{cw} , and calculated effective magnetic moment (μ_{eff}) for $R\text{CrO}_3$.

Sl. No.	$R\text{CrO}_3$	Curie-Weiss Constant, C_{cw}	Curie-Weiss Temperature, θ_{cw} (K)	Effective magnetic moment, μ_{eff} (μ_B)
1	SmCrO_3	0.00109	+533.92	1.57
2	GdCrO_3	0.03467	+19.59	8.42
3	DyCrO_3	0.04505	-8.66	9.78
4	ErCrO_3	0.03306	-12.86	8.41

5.2.3 Magnetization (M) vs. Magnetic Field (H) Measurements

Magnetization versus external field measurements (M–H curves) has been carried out on RCrO_3 nanoparticles in the field range -9 to +9 T at 2.5 K and 320 K. The M–H curves recorded on RCrO_3 nanoparticles at 320 K are found to be linear and indicate the paramagnetic nature of the samples, as shown in figure 7.

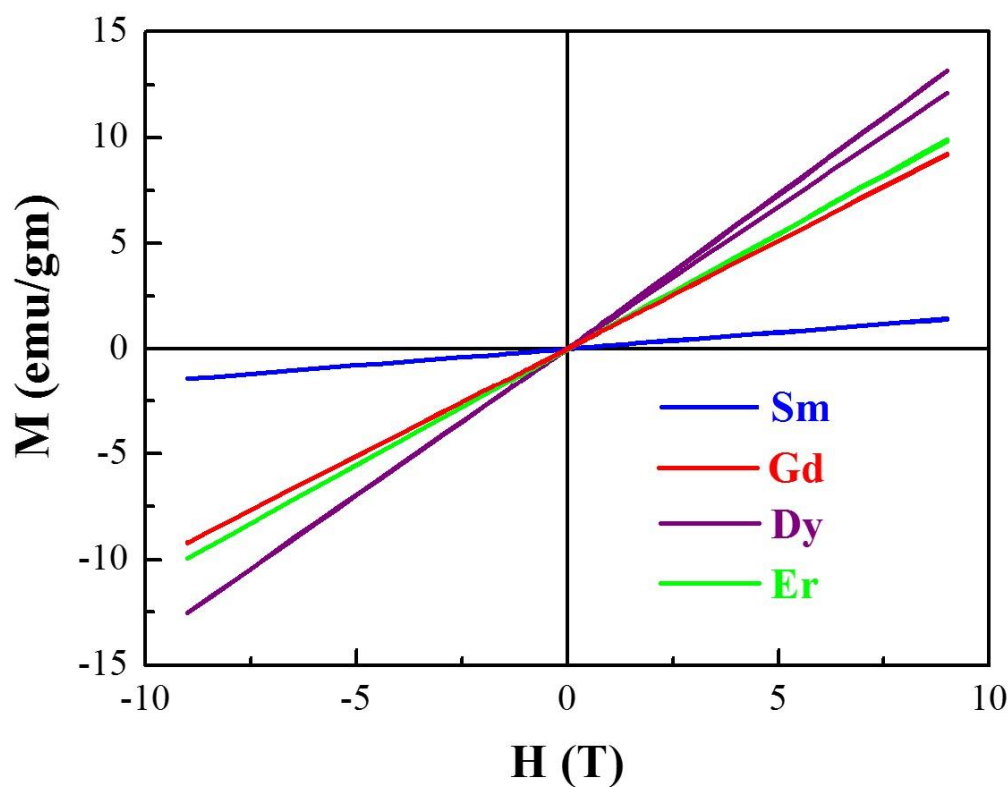


Fig. 7. M-H curve of RCrO_3 recorded at 320 K (in PM regime) in the range $H = -9$ T to +9 T.

Figures 8–11 show the M-H curves recorded on RCrO_3 nanoparticles at 2.5 K in the field range -1 to +1 T. The insets show the figures 8–11 as the same measurements in the field range -9 to +9 T. From this, the observed values of hysteresis, H_c for RCrO_3 nanoparticles are 170, 483, 682, 1497 Oe respectively for $R = \text{Sm, Gd, Dy and Er}$.

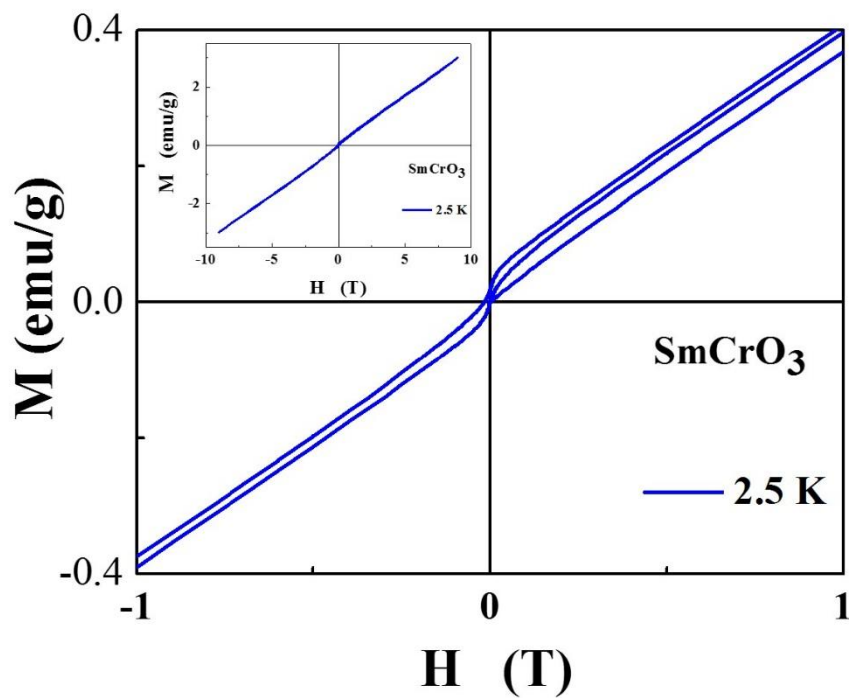


Fig. 8. M - H curve of SmCrO_3 nanoparticles recorded at 5 K.
The inset shows the curves in the range $H = -9$ T to $+9$ T.

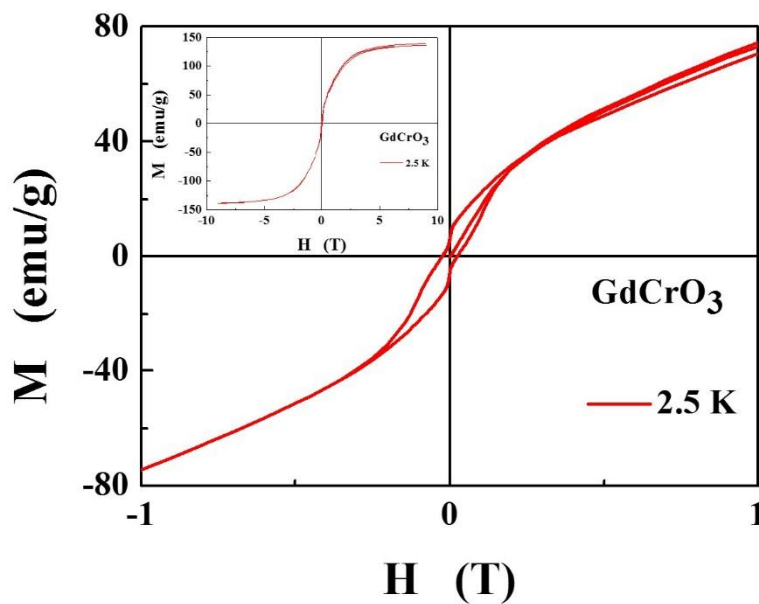


Fig. 9. M - H curve of GdCrO_3 nanoparticles recorded at 2.5 K.
The inset shows the curves in the range $H = -9$ T to $+9$ T.

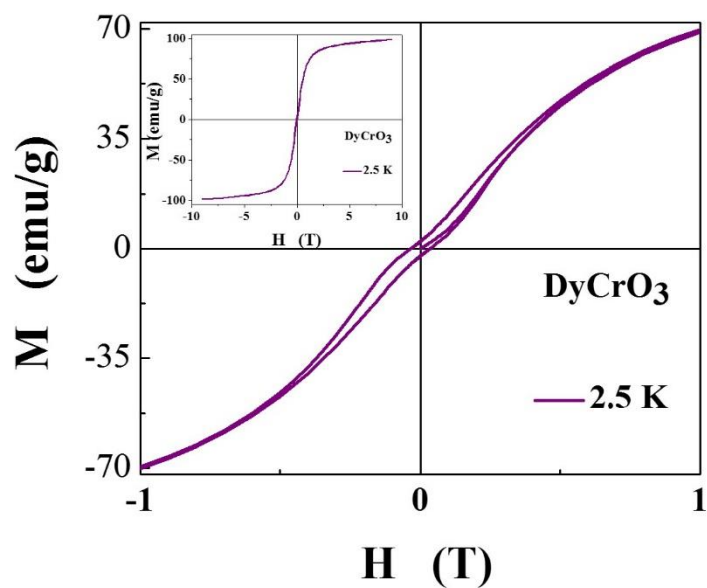


Fig. 10. M - H curve of DyCrO_3 nanoparticles recorded at 2.5 K.

The inset shows the curves in the range $H = -9 \text{ T}$ to $+9 \text{ T}$.

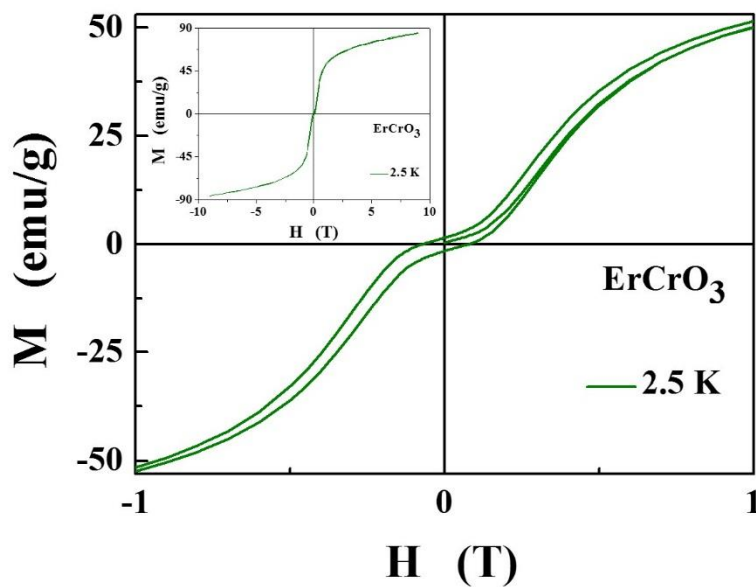


Fig. 11. M - H curve of ErCrO_3 nanoparticles recorded at 2.5 K.

The inset shows the curves in the range $H = -9 \text{ T}$ to $+9 \text{ T}$.

The observed nearly linear M–H plot for $SmCrO_3$ nanoparticles reveal the presence of antiferromagnetic interactions, as shown in figure 8. Figure 9 shows that the magnetization of $GdCrO_3$ was found to saturate at high fields with the magnetic moment at zero-field, $M_z (0 \text{ Oe}) = 136 \text{ emu/gm}$. The pinning of the magnetization near to zero external fields shows the presence of canting of Cr^{3+} sublattices in $GdCrO_3$. Thus, the observed magnetization in $GdCrO_3$ nanoparticles is the result of weak ferromagnetic component due to canting of Cr sublattices with an additional contribution from the paramagnetic Gd^{3+} . Figures 10 and 11 reveals the smooth nature of spontaneous magnetization near to zero fields with nearly zero hysteresis for $DyCrO_3$ and $ErCrO_3$ reveal the collinear antiferromagnetic ordering of the Cr sublattices with zero canting in the ground state. At high fields, the magnetization of $DyCrO_3$, $ErCrO_3$ found not to saturate with observed magnetic moments, M_z at zero-field 86 and 60 emu/gm respectively. Due to the absence of canting of Cr sublattices, the M_z values observed for $DyCrO_3$ and $ErCrO_3$ are expected to be totally from the paramagnetic Dy^{3+} and Er^{3+} ions respectively. It was shown in orthoferrites, isostructural to orthochromites that the magnetization tends to zero as a result of collinear antiferromagnetic ordering of Cr sublattices with the presence of non-magnetic rare earth [20]. Thus, it may be concluded that the contribution to ground state magnetization at zero-field in $RCrO_3$ with a magnetic R and zero canting of the Cr sublattices is solely from the paramagnetic rare earth.

5.3 Conclusions

The DC magnetization measurements on the $RCrO_3$ ($R = Sm, Gd, Dy$ and Er) nanoparticles reveal the antiferromagnetic ordering of the Chromium sublattices with a canting of Cr^{3+}

spins resulting a weak ferromagnetic moment. The weak ferromagnetic moment below T_N^{Cr} makes RCrO_3 to exhibit a non-negligible ferromagnetic hysteresis loop with a pinning at the origin of the M-H curves. M-T curves demonstrate that SmCrO_3 , DyCrO_3 and ErCrO_3 are found to be in antiferromagnetic ground state while GdCrO_3 is in weak ferromagnetic. The magnetic moment per formula unit estimated from modified Curie-Weiss fits are accounted for Cr^{3+} moments along with R^{3+} moment in RCrO_3 nanoparticles respectively and found to be in accordance with the literature.

References

1. I.E. Dzyaloshinskii, *On the magneto-electrical effect in antiferromagnets*, Sov. Phys., **10**, p628 (1960).
2. D.N. Astrov, *Magnetoelectric effect in antiferromagnets*, Sov. Phys., **11**, p708 (1960).
3. G.T. Rado and V.J. Folen, *Observation of the magnetically induced magnetoelectric effect and evidence for antiferromagnetic domains*, Phys. Rev. Lett., **7**, p310 (1961).
4. R.L. White, *Review of recent work on the magnetic and spectroscopic properties of the rare earth orthoferrites*, J. Appl. Phys., **40**, p1061 (1969).
5. L.T Tsymbal, Y.B Bazaliy, V.N. Derkachenko, V.I Kamenev, G.N Kakazei, F.J Palamares and P.E Wigen, *Magnetic and structural of spin-reorientation transitions in orthoferrites*, J. Appl. Phys., **101**, p123919 (2007).
6. I. Singh, A.K. Nigam, K. Landfester, R.M. Espi and A. Chandra, *Anamolous magnetic behavior below 10 K in YCrO_3 nanoparticles obtained under under droplet confinement*, Appl. Phys. Lett., **103**, p182902 (2013).
7. C.R. Serrao, A.K. Kundu, S.B. Krupanidhi, U.V. Waghmare, and C.N.R. Rao, *Biferroic YCrO_3* , Phys. Rev. B (Rapid Comm.), **72**, p220101 (2005).
8. J. Shi, S. Yin, M. S. Seehra, and M. Jain, *Enhancement in magnetocaloric properties of ErCrO_3 via A-site Gd substitution*, J. Appl. Phys., **123**, p193901 (2018).
9. S. Kumar, I. Coondoo, M. Vasundhara, A.K. Patra, A.L. Kholkin, and N. Panwar, *Magnetization reversal behavior and magnetocaloric effect in $\text{SmCr}_{0.85}\text{Mn}_{0.15}\text{O}_3$ chromites*, J. Appl. Phys., **121**, p043907 (2017).
10. E. F. Bertaut, *In Magnetism III*, Academic, New York, **3**, p149 (1968).

11. E. F. Bertaut, G. Bassi, G. Buisson, P. Burlet, J. Chappert, A. Delapalme, J. Mareschal, G. Roult, R. Aleonard, R. Pouthenet, and J. P. Rebouillat, *Some Neutron-Diffraction Investigations at the Nuclear Center of Grenoble*, J. Appl. Phys., **37**, p1038 (1966).
12. G. Alvarez, H. Montiel, M.P. Cruz, A.C. Duran and R. Zamorano, *Resonant and non-resonant microwave absorption in the magnetoelectric $YCrO_3$ through ferro-paraelectric transition*, J. Alloy Compd., **509**, pL331 (2011).
13. Y.Sundarayya and S.Srinath, *Synthesis and magnetic properties of $GdCrO_3$ nanoparticles*, AIP Conf. Proc., **1665**, p050126 (2015).
14. L.H. Yin, J. Yang, P. Tong, X. Luo, C.B. Park, K.W. Shin, W.H. Song, J.M. Dai, K.H. Kim, X.B. Zhu, Y.P. Sun, *Role of rare earth in the magnetic, magnetocaloric and magnetoelectric properties of $RCrO_3$ ($R=Dy, Nd, Tb, Er$) crystals*, J. Mater. Chem. C, **4**, p47 (2016).
15. J.H. Van Vleck, *Theory of Electric and Magnetic Susceptibilities*, Oxford University Press, p86, (1965).
16. A.H. Morrish, *The Physical Principles of Magnetism*, Wiley-IEEE Press, p46-483, New York (2001).
17. A.M. Sánchez, F. Fernández and R.S. Puche, *Magnetic properties of rare earth chromates $RCrO_4$ ($R=Nd, Sm$ and Eu)*, J. Alloy. Comp., **201**, p161 (1993).
18. O. Borang, S.Srinath, S.N. Kaul, and Y. Sundarayya, *Probing the magnetic transitions in europium chromite through electron paramagnetic resonance*, Fazl Ali College Journal, **7**, p120 (2017).

19. K. Sardar, Martin R. Lees, R. J. Kashtiban, J. S. and R. I. Walton, *Direct Hydrothermal Synthesis and Physical Properties of Rare earth and Yttrium Orthochromite Perovskites*, Chem. Mater., **23**, p48 (2011).
20. Y Sundarayya, P Mandal, A Sundaresan and C.N.R Rao, *Mossbauer spectroscopic study of spin reorientation in Mn-substituted Yttrium orthoferrite*, J. Phys. Condens. Matt., **23**, p436001 (2011).

Chapter 6

Electron Paramagnetic Resonance of RCrO_3 (R = Eu, Gd and Er)

6.1 Introduction

RCrO_3 compounds crystallize into orthorhombic structure in such a way that the Cr^{3+} spins at B- site undergo a paramagnetic-canted antiferromagnetic transition below Néel temperature (T_N^1) due to antisymmetric Dzyaloshinskii-Moriya(DM) exchange interaction between neighboring Cr^{3+} spins [1–2]. It is to be noted that the ground state spin configuration of RCrO_3 is Γ_4 (G_x, A_y, F_z) with a weak ferromagnetic moment for R = Y, La [3–5]. The ground state is collinear antiferromagnetic in the case of ErCrO_3 with Γ_1 (A_x, G_y, C_z) spin structure with expected magnetic moment to be zero at T = 0 K [6–7]. For R = Ce, Pr, Nd, Pm, Sm, Eu, Gd, Tb, Dy, Ho, Tm, Yb and Lu, RCrO_3 is found to settle in canted antiferromagnetic ground state with Γ_2 (F_x, C_y, G_z) spin arrangement [8–10]. This may give rise to a non-zero magnetic moment at zero kelvin. This indicates a non-magnetic rare earth favors the Γ_4 spin structure. The presence of magnetic rare earth brings in a temperature-dependent $3d-4f$ interaction between magnetic R^{3+} and Cr^{3+} that may give rise to Γ_2 and/or Γ_1 ground state spin configuration in RCrO_3 [7]. In addition, the presence of a magnetic R^{3+} ion (in place of non-magnetic Y^{3+}) brings in magnetic anisotropy that promotes the phenomena like negative magnetization, magnetic compensation and spin-reorientation (SR) in RCrO_3 [11,12]. Since the magnetism due to R^{3+} is masked by Cr^{3+} over a wide range down to low temperatures, limited is known about the magnetic anisotropy of the rare earth in RCrO_3 oxides [13, 14]. In view of this, temperature – dependent electron paramagnetic resonance (EPR) spectra have been recorded on RCrO_3

and analyzed through Landau-Lifshitz-Gilbert (LLG) equation to understand the role played by the magnetic anisotropy of rare earth.

6.2 Critical View on Magnetic Properties of RCrO_3 ($\text{R} = \text{Eu, Gd and Er}$)

It is shown from the previous chapter that RCrO_3 compounds do not obey Curie-Weiss behavior, i.e. a linear form of reciprocal susceptibility with temperature in the paramagnetic regime that makes us to analyze the data using a modified Curie-Weiss equation. Figures 1 and 2 show the zero-field cooled (ZFC) and field-cooled (FC) magnetization (M) and reciprocal susceptibility (χ^{-1}) of ErCrO_3 with temperature respectively in the range 3–350 K. The Néel temperature of ErCrO_3 being 137 K, it is expected that the χ^{-1} follows a straight line above 137 K in the paramagnetic regime. In fact, the χ^{-1} exhibits a non-CW behavior above 137 K, as shown in figure 2. Moreover, the χ^{-1} is found to decrease in the temperature range 280 – 350 K. This is corroborated by a bifurcation of ZFC and FC magnetization in the same temperature range, as revealed in the inset of Figure 1. Similar observation has been made on EuCrO_3 nanoparticles as shown figures 3 and 4. It shows zero-field cooled (ZFC) and field-cooled (FC) magnetization (M) and reciprocal susceptibility (χ^{-1}) of EuCrO_3 with temperature respectively in the range 3 – 350 K. The Néel temperature of EuCrO_3 being 181 K, it is expected that the χ^{-1} follows a straight line above 181 K in the paramagnetic regime. In fact, the χ^{-1} exhibits a non C-W behavior above 181 K, as shown in figure 4. Moreover, the χ^{-1} is found to deviate from the non-linear behavior in the temperature range 250 – 350 K. This is corroborated by a bifurcation of ZFC and FC magnetization in the same temperature range, as revealed in the inset of Figure 3. Figure 5 and 6 show the zero-field cooled (ZFC) and field-cooled (FC) magnetization (M) and reciprocal susceptibility (χ^{-1}) of GdCrO_3 with temperature

respectively in the range 3 – 350 K. The Néel temperature of GdCrO_3 being 168 K and it is found that the χ^{-1} follows a linear behavior above 168 K in the paramagnetic regime and exhibits a CW behavior, as shown in figure 6. Moreover, no bifurcation has been observed in ZFC and FC magnetization in the temperature range 250 – 350 K, as depicted in the inset of Figure 5. This prompted us to study the complex magnetic behavior of RCrO_3 to search for a magnetic anomaly/transition in this temperature range. Since the RCrO_3 is in the paramagnetic state in this range that gives nearly zero magnetization, we have studied the magnetic property of RCrO_3 ($\text{R} = \text{Eu}, \text{Gd}$ and Er) through temperature dependent electron paramagnetic resonance (EPR) spectroscopy.

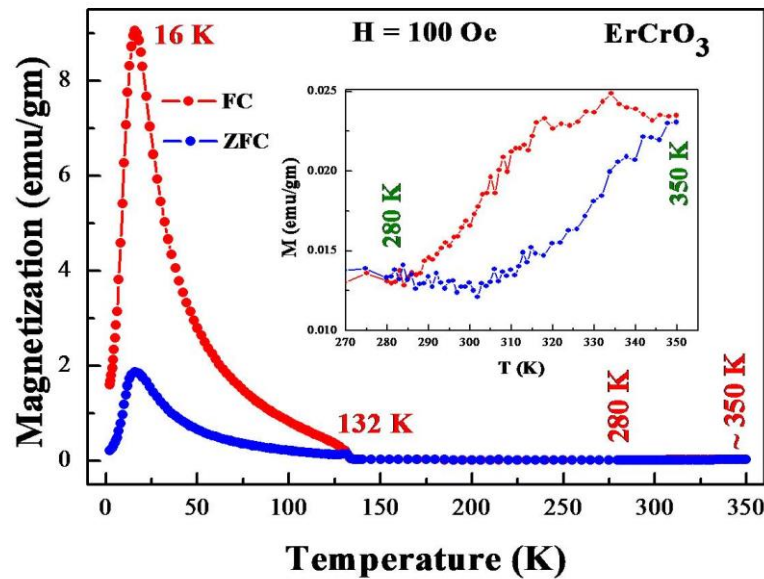


Fig.1. Magnetization of ErCrO_3 with temperature. The inset shows the bifurcation of ZFC and FC magnetization in the range 280 – 350 K.

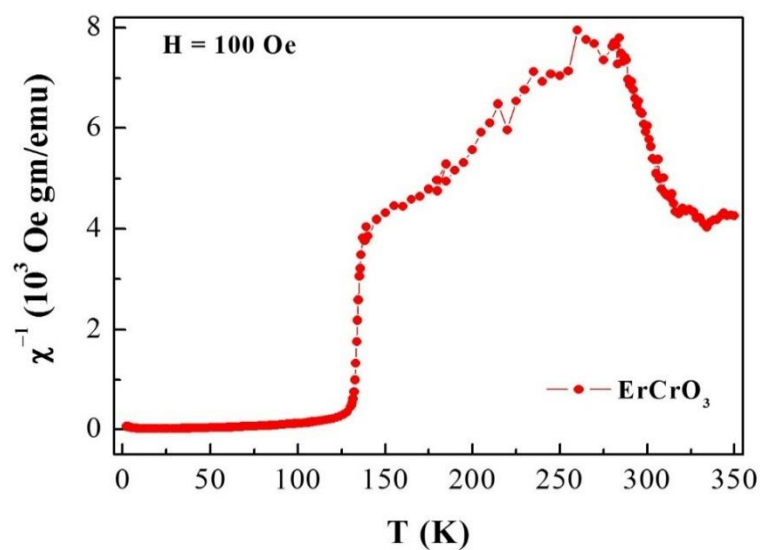


Fig. 2. Reciprocal Susceptibility (χ^{-1}) of ErCrO_3 with temperature.

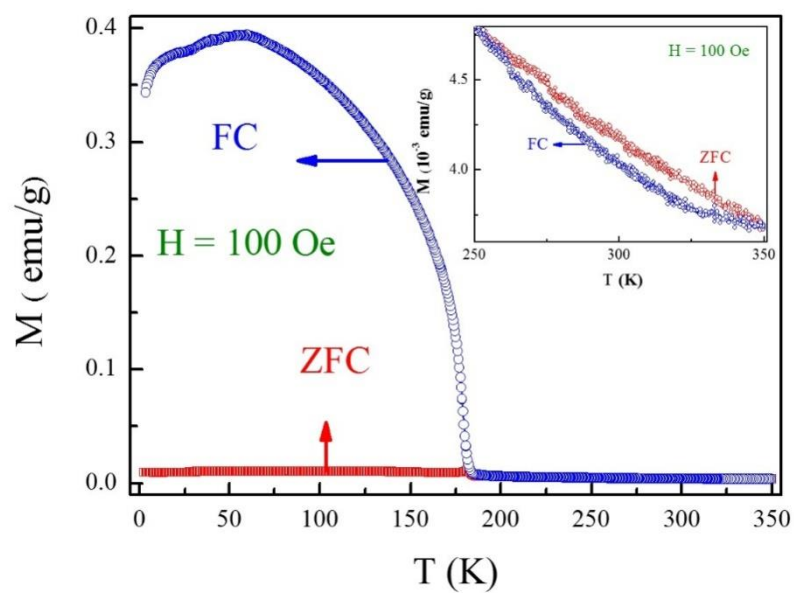


Fig.3. Magnetization of EuCrO_3 with temperature. The inset shows the bifurcation of ZFC and FC magnetization in the range 250 – 350 K.

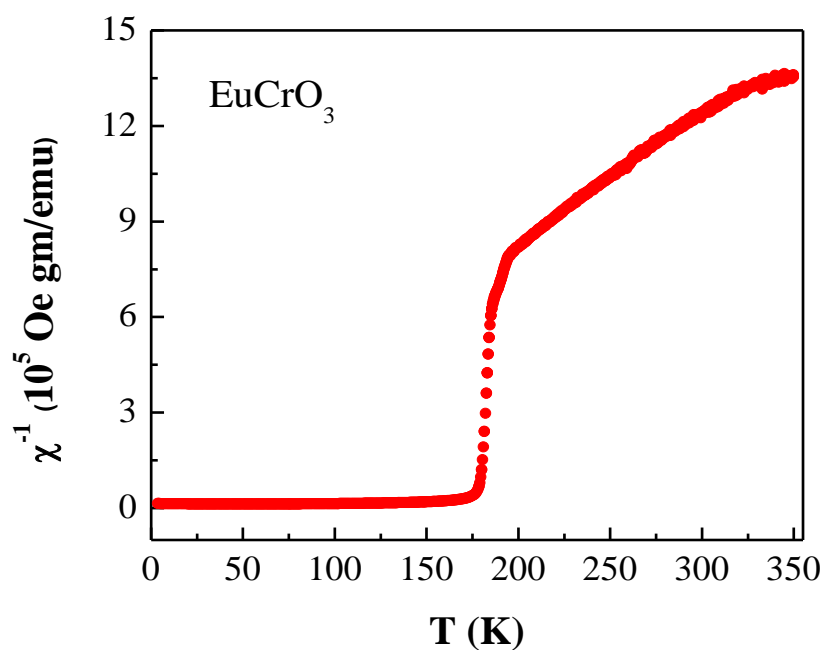


Fig. 4. Reciprocal Susceptibility (χ^{-1}) of EuCrO_3 with temperature.

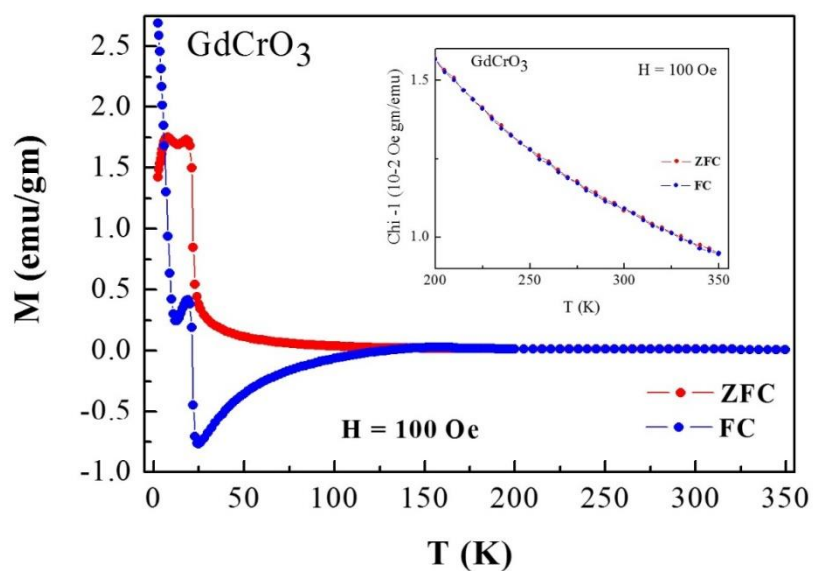


Fig.5. Magnetization of GdCrO_3 with temperature. The inset shows the bifurcation of ZFC and FC magnetization in the range 200 – 350 K.

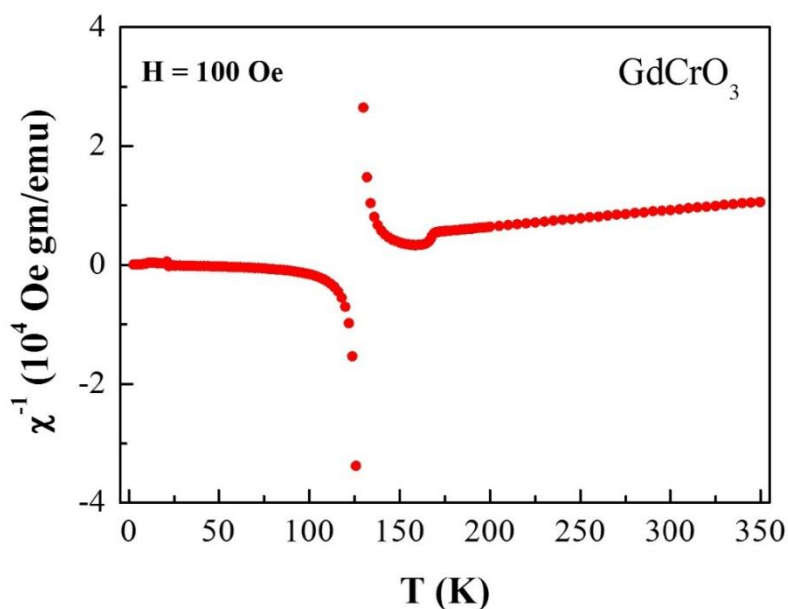


Fig. 6. Reciprocal Susceptibility (χ^{-1}) of GdCrO_3 with temperature.

EPR is a powerful tool to study the dynamics of spin states across the transition in a magnetic system, canted antiferromagnets in particular. An appropriation of the EPR for the variation of the research intended is stated by its ability to differentiate clearly between the different kinds of magnetic order because they give rise to significantly different variations of the EPR line width with temperature.

6.3 Room-temperature EPR Spectra of RCrO_3 ($\text{R} = \text{Eu}, \text{Gd}$ and Er)

Figure 7 shows the electron paramagnetic resonance spectra of EuCrO_3 , GdCrO_3 , and ErCrO_3 nanoparticles at 373 K, with rate of power, dP/dH absorbed on the Y-axis with respect to the external magnetic field, H on the X-axis at a fixed frequency of 9.2 GHz, shown by open circles. The thick red line passing through the data is the Landau-Lifshitz-Gilbert (LLG) non-linear least square fit, explained in the forth coming discussion. The EPR spectral parameters that have been obtained from the observed spectral analysis are

the resonance field, H_{res} (the field where the $dP/dH = 0$ line cuts the dP/dH versus H curve), the peak-to-peak width, ΔH_{pp} (the field difference between the extrema of the dP/dH versus H curve), the peak-to-peak differential intensity, ΔI_{pp} (the spectral intensity difference between the extrema of dP/dH versus H curve). The observed values for the resonance field, H_{res} and the line-width, ΔH_{pp} and differential intensity, ΔI_{pp} at 373 K are given in Table 1. The observed value of the g -factor at 373 K is nearly 2 and confirms the paramagnetic nature of RCrO_3 nanoparticles.

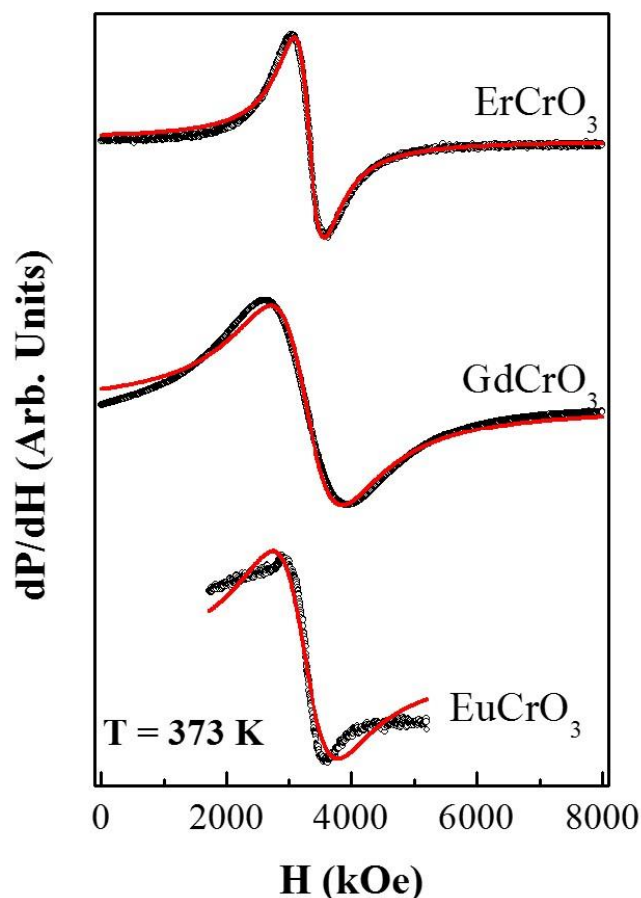


Fig.7. EPR spectra of EuCrO_3 , GdCrO_3 , and ErCrO_3 nanoparticles at 373 K.

Table 1: The observed values of the resonance field, H_{res} , the line-width, ΔH_{pp} and differential intensity, ΔI_{pp} at 373 K.

Sl. No.	$R\text{CrO}_3$	Resonance field, H_{res} (Oe)	Peak-to-peak width, ΔH_{pp} (Oe)	Differential intensity, ΔI_{pp} (Arb. Units)
1	EuCrO_3	3380	2227	2851
2	GdCrO_3	3282	1149	2910
3	ErCrO_3	3285	484	1855

6.4 Temperature-dependent EPR Spectra of $R\text{CrO}_3$ ($R = \text{Eu, Gd and Er}$)

To examine the magnetic transitions, temperature dependent electron paramagnetic resonance spectra (EPR) were recorded on EuCrO_3 , GdCrO_3 , and ErCrO_3 nanoparticles in the X-band region in the range 116 – 373 K using a liquid nitrogen cryostat, as described in chapter 2. Figures 8, 9 and 10 show the electron paramagnetic resonance spectra of EuCrO_3 , GdCrO_3 and ErCrO_3 nanoparticles at three different temperatures in the range 116 – 373 K with rate of power, dP/dH absorbed on the Y-axis with respect to the external magnetic field, H on the X-axis. The change of spectral line shape observed for EuCrO_3 at 118, 273 and 373 K indicates that EuCrO_3 may exists in three different magnetic states, as observed in figure 8. Similar observation may be made for ErCrO_3 at 116, 203, 373 K respectively, as given in figure 9. However, the nearly similar line shape observed for GdCrO_3 at 253 and 373 K may indicate that GdCrO_3 exists in the same magnetic state at 253 and 373 K. A different line shape with change of spectral intensity at 123 K reveals the presence of different magnetic state, as shown in figure 10.

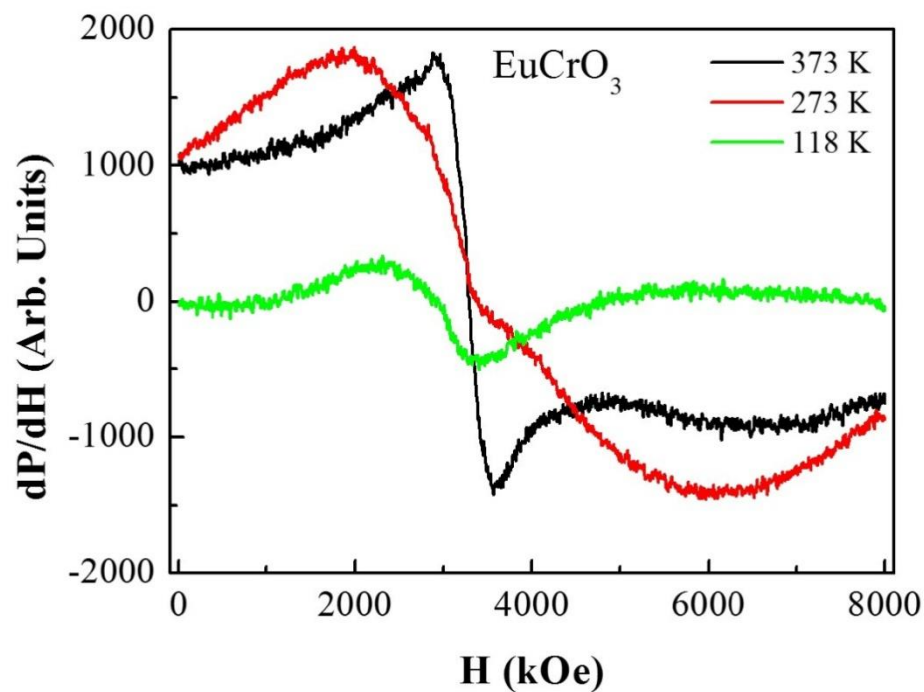


Fig. 8. As-recorded EPR spectra of EuCrO_3 nanoparticles as a function of temperature.

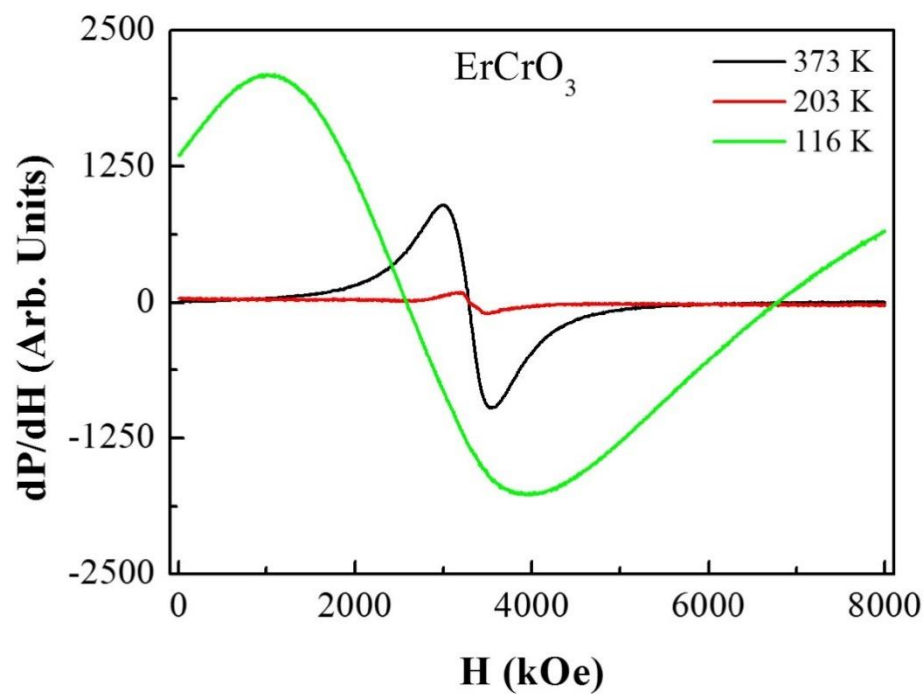


Fig. 9. As-recorded EPR spectra of ErCrO_3 nanoparticles as a function of temperature.

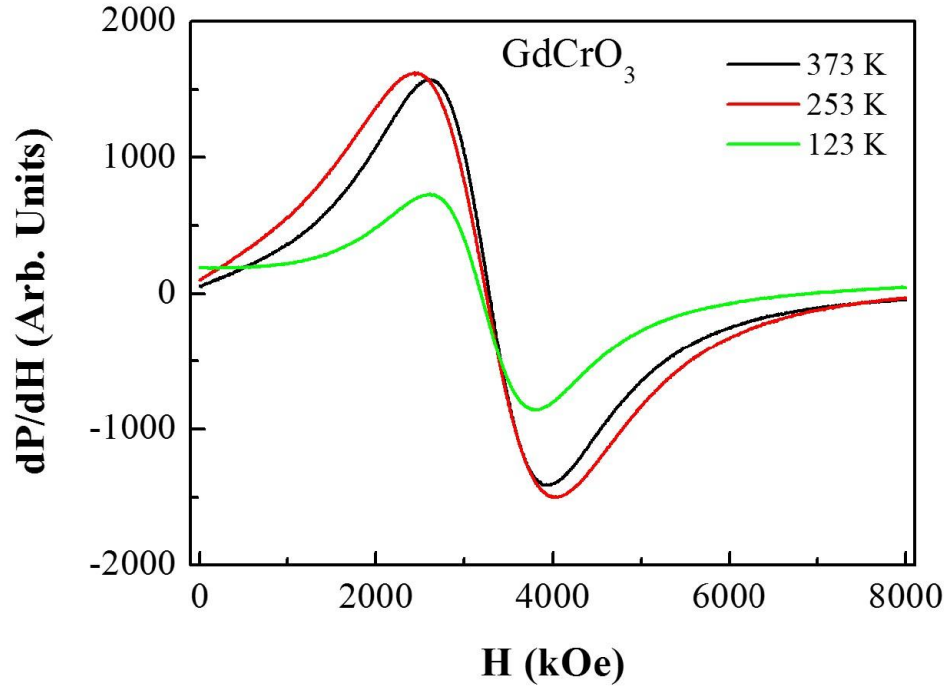


Fig.10. As-recorded EPR spectra of GdCrO_3 nanoparticles as a function of temperature.

To ascertain the nature of magnetic anisotropy of rare earth on the chromium sublattice, the EPR spectra have been analyzed by line-shape analysis [15, 16]. The complete line shape of dP/dH versus H curves recorded at different temperatures of EuCrO_3 , GdCrO_3 and ErCrO_3 have been analyzed with the aid of a non-linear least square fit program in the light of Landau-Lifshitz-Gilbert (LLG) equation for a polycrystalline material. The program treats the Lande's splitting factor g , saturation magnetization $4\pi M_s$ as free-fitting parameters and makes use of the observed values of $\Delta H_{pp} (= 1.45\lambda\omega/\gamma^2 M_s)$. The values of anisotropy field H_k are derived from the lineshape analysis using the resonance condition given by

$$[(\omega/\gamma)^2 + \Gamma^2] = (H_{res} + 4\pi M_s + H_k)(H + H_k) \quad \dots (1)$$

$$[(\omega/\gamma)^2 + \Gamma^2] = (H_{res} + 4\pi M_s - H_k)(H - H_k) \quad \dots (2)$$

by solving the dynamic magnetization motion from Landau Lifshitz- Gilbert equation

$$\frac{dM}{dt} = -\gamma (M \times H_{\text{eff}}) + \frac{\lambda}{\lambda M_S^2} \left(M \times \frac{dM}{dt} \right) \quad \dots (3)$$

Where $\Gamma = \lambda\omega/\gamma^2 M_S$ is the line width of parameter, $\gamma = ge/2mc$, magneto mechanical ratio and λ is the Gilbert damping factor, H_{eff} is the effective magnetic moment of the spins. In addition, the line shape analysis reveals that the Lande's splitting factor g has a temperature-independent value of about 2.00 throughout the temperature range, which resembles the paramagnetic nature of the RCrO_3 ($R = \text{Eu, Gd and Er}$). This is due to the fact that RCrO_3 contains two magnetic viz. R^{3+} and Cr^{3+} species. It is to be noted that Cr^{3+} spins undergo a PM–CAFM transition below Néel temperature, while the R^{3+} spins may remain to be paramagnetic down to low temperatures that gives rise to nearly constant value of the Lande's splitting factor. The parameters obtained from the detailed analysis of temperature dependent EPR spectra are the peak-to-peak width, ΔH_{pp} , the peak-to-peak differential intensity, ΔI_{pp} , termed as EPR parameters and the spontaneous magnetization, $4\pi M_S$ (emu/cm³) and magnetic anisotropy field, H_k (kOe), named as magnetic parameters.

Figures 11(a) shows the variation of observed values of ΔI_{pp} as a function of temperature of EuCrO_3 . It reveals that the values of ΔI_{pp} are nearly constant from 118 K to 178 K. Further increase in temperature results an abrupt increase in ΔI_{pp} values has been observed in the temperature range 178 – 188 K, depicts a magnetic transition. Above 188 K, the ΔI_{pp} values decrease gradually up to 373 K with a dip around 293 K. Figures 11(b) shows the variation of observed values of ΔH_{pp} as a function of temperature of EuCrO_3 . It reveals that the values of ΔH_{pp} do not vary appreciably from 118 K to 178 K. A sudden increase in ΔH_{pp} values has been observed at temperature 178 K, corroborated by a magnetic

transition with an abrupt change of ΔI_{pp} values. This is attributed to canted antiferromagnetic to paramagnetic transition of the Cr^{3+} spin structure in EuCrO_3 with Néel temperature, $T_N = 181$ K, observed from DC magnetic measurements. Further increase in temperature results a gradual increase of ΔH_{pp} values from 183 – 297 K. Further, an abrupt decrease of the ΔH_{pp} values has been observed from 297 – 312 K; similar to a dip in ΔI_{pp} values around 293 K, indicates the presence of a magnetic transition in EuCrO_3 .

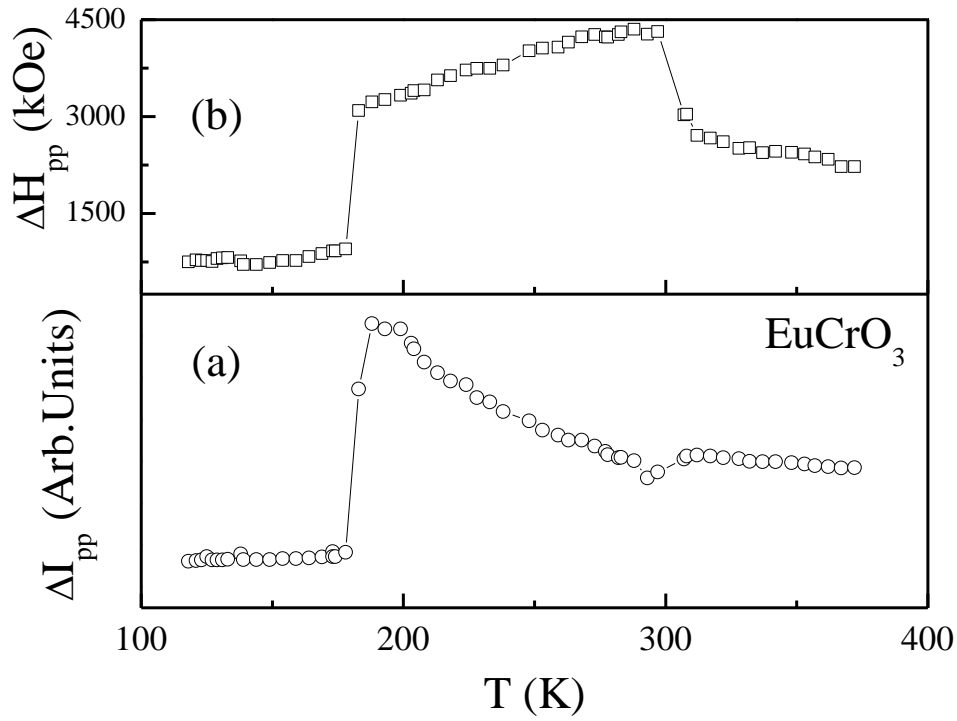


Fig. 11. The EPR spectral parameters peak-to-peak width (ΔH_{pp}) and differential intensity (ΔI_{pp}) of EuCrO_3 with temperature.

Figures 12(a) and 12(b) shows the variation of spontaneous magnetization, magnetic anisotropy field, H_k (kOe) and $4\pi M_S$ (emu/cm³) of EuCrO_3 in the temperature range 118

– 373 K, obtained from the analysis of temperature dependent EPR spectra using LLG equations.

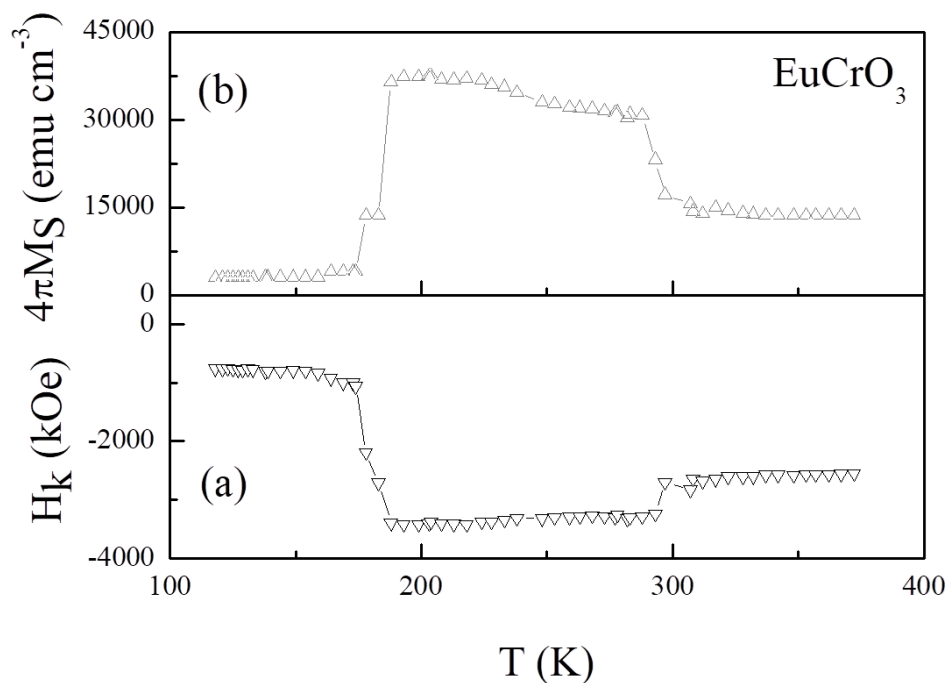


Fig. 12. The magnetic parameters spontaneous magnetization ($4\pi M_s$) and magnetic anisotropy field (H_k) of EuCrO_3 as a function of temperature.

The spontaneous magnetization undergoes a rapid increase from 173 K to 183 K with increasing temperature, indicating the canted antiferromagnetic to paramagnetic transition in EuCrO_3 . Above 183 K, the $4\pi M_s$ value is nearly constant up to 288 K with a sudden decrease in the temperature range 288 – 308 K. In addition, the spontaneous magnetization is almost constant above 308 K, in the paramagnetic regime. Figure 12(b) reveals that the values $4\pi M_s$ do not vary appreciably in the temperature range 118 – 173 K. Figure 12(a) demonstrates that the values of magnetic anisotropy field (H_k) are nearly constant in the temperature range 118 – 173 K before the H_k values undergo a rapid decrease in the range

118 – 183 K. Again, the anisotropy field values do not change noticeably in the range 183 – 288 K and undergo a sudden increase in the range 288 – 308 K above the H_k values become nearly constant. A similar trend has been observed in the case of spontaneous magnetization, $4\pi M_S$ values. It should be noted that the variation of $4\pi M_S$ and H_k in the range is attributed to the canted antiferromagnetic to paramagnetic transition of Cr^{3+} spin structure in EuCrO_3 , supported by the variation of ΔH_{pp} and ΔI_{pp} values. However, the magnetic transition observed in the temperature range 288 – 308 K, supported by the variation of ΔH_{pp} , ΔI_{pp} , $4\pi M_S$ and H_k with the apparent non-linear behavior of inverse susceptibility (χ^{-1}) in the paramagnetic regime of EuCrO_3 is not known and needs further investigation.

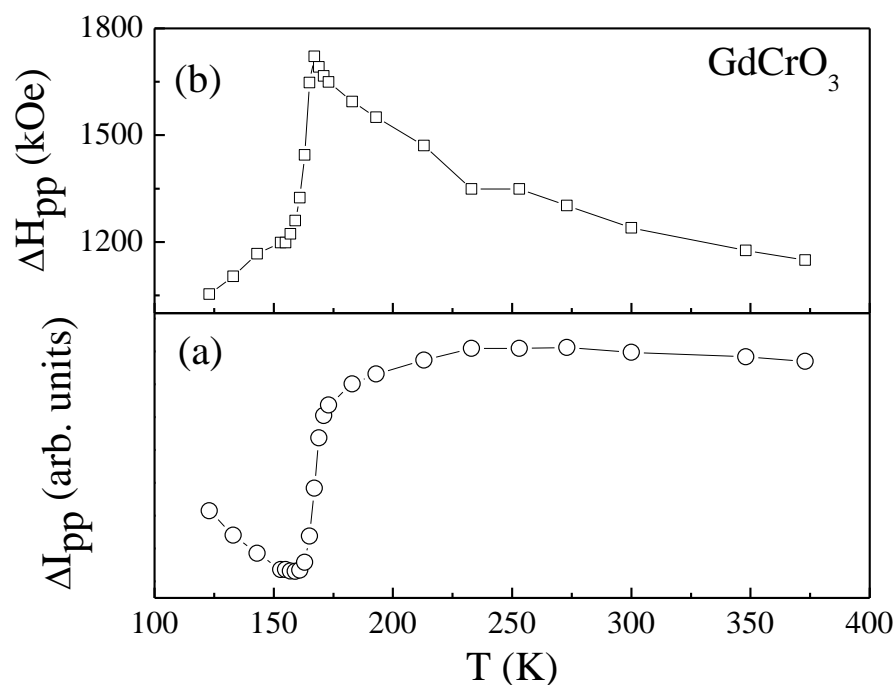


Fig. 13. The EPR spectral parameters peak-to-peak width (ΔH_{pp}) and differential intensity (ΔI_{pp}) of GdCrO_3 with temperature.

Figures 13(a) shows the variation of observed values of ΔI_{pp} as a function of temperature of GdCrO_3 . It reveals that the value of intensity goes smoothly decreasing until it reaches around 163 K which is a transition temperature. Above 163 K, it shoots up suddenly. The second figure which is figure 13 (b) is showing the peak to peak delta versus temperature of GdCrO_3 . It has been observed from the graph that the values of ΔH_{pp} undergo a sharp increase at nearly 167 K in GdCrO_3 , above which it gradually decreases, which indicates the changes occurring in the material. This is attributed to canted antiferromagnetic to paramagnetic transition of the Cr^{3+} spin structure in GdCrO_3 with Néel temperature, $T_N = 168$ K, observed from DC magnetic measurements.

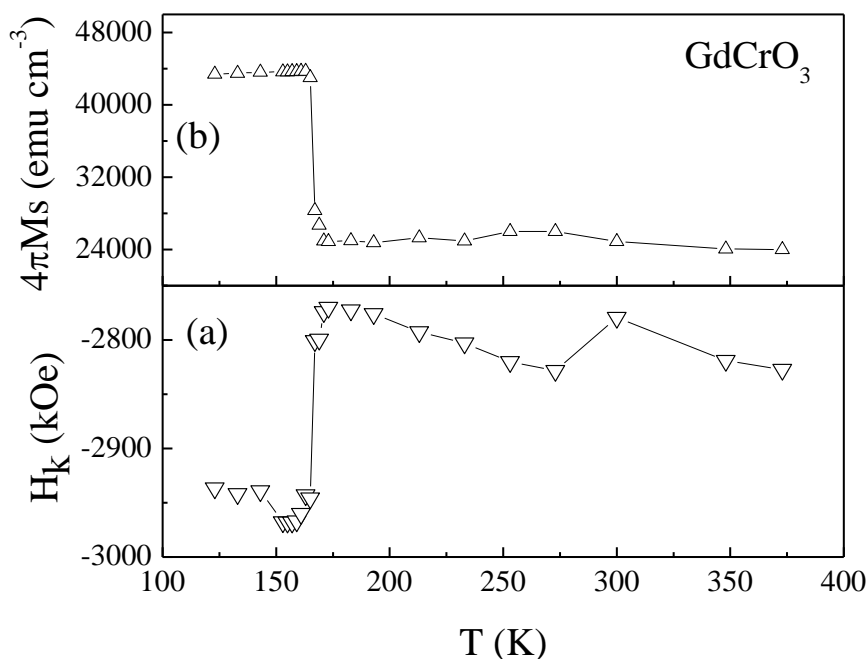


Fig. 14. The magnetic parameters spontaneous magnetization ($4\pi M_s$) and magnetic anisotropy field (H_k) of GdCrO_3 as a function of temperature.

Figures 14(a) and 14(b) show the variation of spontaneous magnetization, $4\pi M_s$ (emu/cm^3) and magnetic anisotropy field, H_k (kOe) of GdCrO_3 in the temperature range 118 – 373 K,

obtained from the analysis of temperature dependent EPR spectra using LLG equations. Figure 14(b) reveals that the value of $4\pi M_S$ almost follows the constant trends until it reaches 163 K. Above 163 K the value of $4\pi M_S$ suddenly decreases and gets neutral upto the highest temperature range. Figure 14(a) demonstrates that the values of magnetic anisotropy field (H_k) are nearly equal value at the starting but when it reaches 163 K, it started increasing abruptly. Above 163 K the anisotropy value follows the constant path. A similar trend has been observed in the case of spontaneous magnetization, $4\pi M_S$ values. It should be noted that the variation of $4\pi M_S$ and H_k in the range is attributed to the canted antiferromagnetic-paramagnetic transition of Cr^{3+} spin structure in GdCrO_3 , supported by the variation of ΔH_{pp} and ΔI_{pp} values.

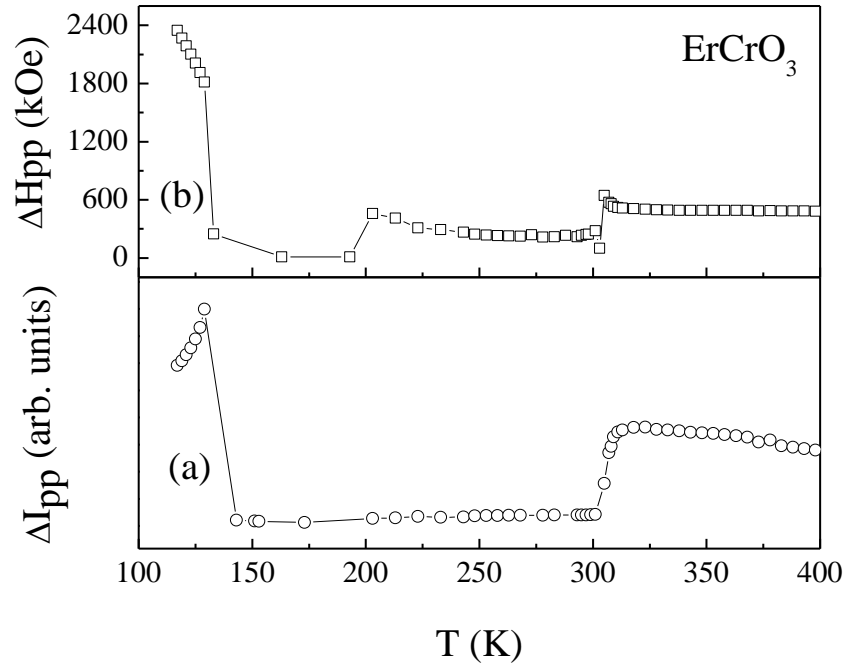


Fig. 15. The EPR spectral parameters peak-to-peak width (ΔH_{pp}) and differential intensity (ΔI_{pp}) of ErCrO_3 with temperature.

Figures 15(a) shows the variation of observed values of ΔI_{pp} as a function of temperature. It reveals that the values of spectra of ΔI_{pp} are slowly increasing with an increasing order of temperature. But when it reaches at around 133 K it races down rapidly up to 139 K after which it follows constant and again shoots up suddenly at 300 K which depicts a magnetic transition. Like EuCrO_3 even in this compound, we can see two transitions depending upon the temperature.

Figure 15(b) shows the variation of observed values of ΔH_{pp} as a function of temperature. From here we can see that, the spectra is decreasing with an increasing order of temperature but at around 139 K it has almost follows the constant trend until it reaches the temperature range of 300 K.

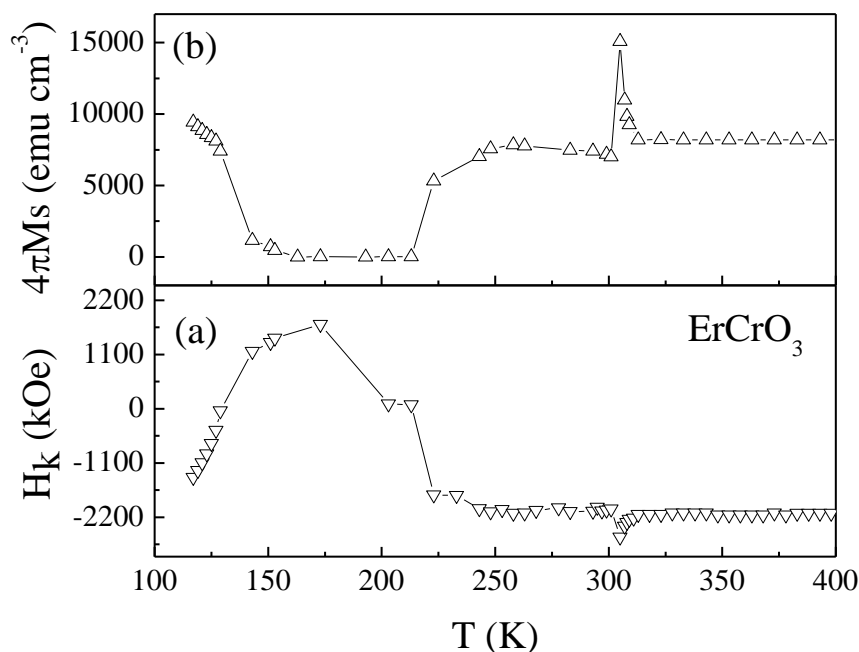


Fig. 16. The magnetic parameters spontaneous magnetization ($4\pi M_s$) and magnetic anisotropy field (H_k) of ErCrO_3 as a function of temperature.

Figures 16(a) and 16(b) show the variation of spontaneous magnetization, magnetic anisotropy field, H_k (kOe) and $4\pi M_S$ (emu/cm³) of ErCrO_3 in the temperature range 116 – 373 K, obtained from the analysis of temperature dependent EPR spectra using LLG equations. Figure 16(a) demonstrates that the values of magnetic anisotropy field (H_k) are constantly increasing in the temperature range 117 – 173 K before the H_k values undergo a rapid decrease in the range 173 – 243 K. Again, the anisotropy field values do not change noticeably in the range 243 – 301 K and undergo a sudden decrease and then increase in the range 301 – 313 K before the H_k values become nearly constant. From figure 16 (b) we can observe that the magnetization is decreasing gradually with an increasing temperature and became almost constant until a mild increase. When it reaches at around 300 K it has a sudden increase which we have been showed in other parameters too.

A similar trend has been observed in the case of anisotropy field, H_k values. It should be noted that the variation of $4\pi M_S$ and H_k in the range is attributed to the canted antiferromagnetic- paramagnetic transition of Cr^{3+} spin structure in ErCrO_3 , supported by the variation of ΔH_{pp} and ΔI_{pp} values. However, the magnetic transition observed in the temperature range 301 – 313 K, supported by the variation of ΔH_{pp} , ΔI_{pp} , $4\pi M_S$ and H_k with the apparent non-linear behavior of inverse susceptibility (χ^{-1}) in the paramagnetic regime of ErCrO_3 is not known and needs further investigation. The transition temperatures are not overlapping with each other which show the presence of more than one transition.

6.5 Conclusions

DC magnetic measurements on the $R\text{CrO}_3$ where ($R = \text{Eu}, \text{Gd}$ and Er) nanoparticles shows Cr^{3+} spins undergo a paramagnetic to antiferromagnetic transition at 181, 168 and 137 K respectively at Néel temperature (T_N^{Cr}) with canting of spins at chromium sub-lattice due to antisymmetric Dzyaloshinskii-Moriya transition. At low temperatures, the chromium spin-structure appears to take Γ_2 (F_x, C_y, G_z) in case of EuCrO_3 and GdCrO_3 nanoparticles while the ground state spin configuration is Γ_1 (A_x, G_y, C_z) in and ErCrO_3 nanoparticles. A critical view of magnetic measurements reveal that EuCrO_3 and ErCrO_3 exhibit an unusual bifurcation of ZFC and FC magnetization in the paramagnetic regime, close to room temperature. This indicates the presence of a magnetic transition unlike the PM–CAF M transition. However, such anomaly has not been observed in GdCrO_3 . Detailed analysis of the temperature dependent EPR spectra recorded in the range 118 – 373 K shows the R^{3+} spins remain in the paramagnetic state and the magnetic anisotropy plays a major role in tuning the spin structure of chromium. The PM –CAF M transition in all the three chromites in discussion and unfamiliar magnetic transition in EuCrO_3 and ErCrO_3 have been corroborated by an abrupt variation of line-width (ΔH_{pp}) and Differential intensity (ΔI_{pp}), the spontaneous magnetization ($4\pi M_s$), and magnetic anisotropy field (H_k) at respective magnetic transitions.

References

1. B. Rajeswaran, D. I. Khomskii, A. K. Zvezdin, C.N.R. Rao and A. Sundaresan, *Field-induced polar order at the Néel temperature of chromium in rare earth orthochromites: Interplay of rare earth and Cr magnetism*, Phys.Rev.B, **86**, p214409 (2012).
2. H.J. Zhao, J. Iniguez, X.M. Chen, and L. Bellaiche, *Origin of the magnetization and compensation temperature in rare earth orthoferrites and orthochromites*, Phys. Rev. B, **93**, p014417 (2016).
3. I. Singh, A. K. Nigam, K. Landfester, R.M. Espi and A. Chandra, *Anomalous magnetic behavior below 10 K in YCrO_3 nanoparticles obtained under droplet confinement*, Appl. Phys. Lett., **103**, p182902 (2013).
4. C. Rayan Serrao, A. K. Kundu, S. B. Krupanidhi, U. V. Waghmare, and C. N. R. Rao, *Biferroic YCrO_3* , Phys. Rev. B (Rapid Comm.), **72**, p220101 (2005).
5. G. Alvarez, H. Montiel, M.P. Cruz, A.C. Duran and R. Zamorano, *Resonant and non-resonant microwave absorption in the magnetoelectric YCrO_3 through ferro-paraelectric transition*, J. Alloy Compd., **509**, pL331 (2011).
6. E. F. Bertaut, *In Magnetism III*, edited by G. T. Rado and H. Suhl ,Academic, New York, **3**, p. 149 (1968).
7. E. F. Bertaut, G. Bassi, G. Buisson, P. Burlet, J. Chappert, A. Delapalme, J. Mareschal, G. Roult, R. Aleonard, R. Pouthenet, and J. P. Rebouillat, *Some Neutron-Diffraction Investigations at the Nuclear Center of Grenoble*, J. Appl. Phys., **37**, p1038 (1966).
8. A. Morales-Sánchez, F. Fernández and R. Sáez-Puche, *Magnetic properties of rare earth chromates $R\text{CrO}_4$ ($R=\text{Nd}, \text{Sm}$ and Eu)*, J. Alloy. Comp., **201**, p161 (1993).

9. J. H. Van Vleck, *Theory of Electric and Magnetic Susceptibilities*, Oxford University Press, Oxford (1965).
10. A. H. Morrish, *The Physical Principles of Magnetism*, Wiley-IEEE Press, New York (2001).
11. T. Sakata, and A. Enomura, *Studies of the rare earth-iron interactions in the orthoferrites GdFeO_3 and HoFeO_3* , Phys. Status Solidi A, **52**, p311 (1979).
12. K.B. Aring, and A. J. Sievers, *Role of the Ytterbium Spins in the Spin Reorientation in YbFeO_3* , J. Appl. Phys., **41**, 1197 (1970).
13. E. J. Melero, P.C.M. Gubbens, M.P. Steenvoorden, S.Sakarya, A.Goosens, P.D.D. Reotier, A. Yaouanc, J. R. Carvajal, B. Beuneu, J. Isasi, R. S. Puche, U. Zimmerman and J. L. Martinez, *A combined studies of the magnetic properties of GdCrO_4* , J. Phys.: Condens. Matter., **18**, p7893 (2006).
14. Y. Long, Q. Liu, YuxiLv, R. Yu, C. Jin, *Various 3d-4f spin interactions and field-induced metamagnetism in the Cr^{5+} system DyCrO_4* , Phys. Rev. B, **83**, p024416 (2011).
15. S.N. Kaul and V. Siruguri, *Ferromagnetic resonance evidence for long-range ferromagnetic ordering in amorphous Fe-rich $\text{Fe}_{100-x}\text{Zr}_x$ alloys*, J. Phys. Condens. Matter, **4**, p505 (1992).
16. S.N. Kaul and V. Siruguri, *Origin of magnetism in amorphous $\text{Ni}_{81.6}\text{B}_{18.4}$ alloy*, J. Phys. F: Met. Phys., **17**, pL255 (1987).

Chapter 7

Conclusions

Homogeneous single phase zircon-type tetragonal RCrO_4 and perovskite RCrO_3 nanoparticles have been synthesized through a modified sol-gel route followed by hydrothermal method from a single precursor. It has been observed that the heat treatment of the as-synthesized amorphous powder at 773 K favours the crystallization of zircon-type RCrO_4 (space groups $I41/amd$, No. 141, $Z=4$ with crystal symmetry D_{4h}^{19}) nanoparticles with Chromium stabilized in unusual Cr^{5+} state and 973 K results the of formation orthorhombic RCrO_3 (space group $Pbnm$ and D_{4h}^{19} crystal symmetry) nanoparticles with a stable Cr^{3+} at ambient pressure. The high pressure involved during the hydrothermal synthesis facilitates the stabilization of the metastable Cr^{5+} resulting the monodisperse single phase RCrO_4 which is unstable at high temperature. It has been demonstrated that the formation of RCrO_4 nanoparticles with smaller sizes while an increase of particle has been observed in respective RCrO_3 nanoparticles. The particle size plays a major in tuning the crystal structures and respective magnetic properties of rare earth chromium oxides at nanoscale with the aid of annealing temperature. Elemental analysis of the samples demonstrated the presence of R, Cr and O in RCrO_4 and RCrO_3 nanoparticles in the ratios 1:1:4 and 1:1:3 respectively.

The DC Magnetization measurements on the RCrO_4 ($R = \text{Sm, Gd, Dy and Er}$) nanoparticles exhibit magnetic transition temperature as a result of antiferromagnetic ordering of R^{3+} and ferromagnetic ordering of Cr^{5+} ions. from the analysis of by $d\chi_{ZFC}/dT$ curves, the presence of antiferromagnetic ordering of R^{3+} sublattice and ferromagnetic

ordering Cr^{5+} sublattice with a closely spaced Néel and Curie temperatures (T_N and T_C) at low temperatures, has been confirmed. The presence of a non-zero hysteresis and unsaturation of spontaneous magnetization at high fields observed in M-H curves validate the simultaneous competing antiferromagnetic and ferromagnetic interactions that lead to magnetic frustration in RCrO_4 with a ferromagnetic ground state. The non-linear behavior of Curie-Weiss fits confirms the Van-Vleck contribution due to rare earth ions. The magnetic moment per formula unit estimated from modified Curie-Weiss fits are accounted for Cr^{5+} moments along with R^{3+} moment in RCrO_4 nanoparticles respectively and found to be in accordance with the literature.

The DC magnetization measurements on the RCrO_3 ($\text{R} = \text{Sm}, \text{Gd}, \text{Dy}$ and Er) nanoparticles reveal the antiferromagnetic ordering of the Chromium sublattices with a canting of Cr^{3+} spins resulting a weak ferromagnetic moment. The weak ferromagnetic moment below T_N^{Cr} makes RCrO_3 to exhibit a non-negligible ferromagnetic hysteresis loop with a pinning at the origin of the M-H curves. M-T curves demonstrate that SmCrO_3 , DyCrO_3 and ErCrO_3 are found to be in antiferromagnetic ground state while GdCrO_3 is in weak ferromagnetic. The magnetic moment per formula unit estimated from modified Curie-Weiss fits are accounted for Cr^{3+} moments along with R^{3+} moment in RCrO_3 nanoparticles respectively and found to be in accordance with the literature.

A critical view of magnetic measurements reveal that EuCrO_3 and ErCrO_3 exhibit an unusual bifurcation of ZFC and FC magnetization in the paramagnetic regime, close to room temperature. This indicates the presence of a magnetic transition unlike the PM–CAFm transition. However, such anomaly has not been observed in GdCrO_3 . Detailed analysis of the temperature dependent EPR spectra recorded in the range 118 – 373 K

shows the R^{3+} spins remain in the paramagnetic state and the magnetic anisotropy plays a major role in tuning the spin structure of chromium. The PM–CAF_M transition in all the three orthochromites in discussion and unfamiliar magnetic transition in EuCrO_3 and ErCrO_3 have been corroborated by an abrupt variation of line-width (ΔH_{pp}) and Differential intensity (ΔI_{pp}), the spontaneous magnetization ($4\pi M_{\text{S}}$), and magnetic anisotropy field (H_{k}) at respective magnetic transitions.